INTERFACIAL MORPHOLOGY AND DESCALING OF REHEATED STAINLESS STEEL

By

Nana-Araba Quagraine

Submitted in partial fulfillment of the requirements for the degree

Master of Engineering

In the Department of Materials Science and Metallurgical Engineering, Faculty of Engineering, Built Environment and Information Technology, University of Pretoria, Pretoria, Republic of South Africa

Supervisor: Professor PC Pistorius

April, 2001

Acknowledgements

I am greatly indebted to my lecturers, colleagues and friends who directly or indirectly helped me in preparing this thesis. Special thanks to Professor Chris Pistorius, my supervisor, for his guidance and unending support; as well as Mr Carel Coetzee for his assistance with the SEM. I would also like to express my gratitude to Carnegie Mellon University and Iscor as well as Columbus stainless steel for providing all of the samples and financial support.

INTERFACIAL MORPHOLOGY AND DESCALING OF REHEATED STAINLESS STEEL

By

Nana-Araba Quagraine

Prof. PC Pistorius

Department of Material Science and Metallurgical Engineering

Master Degree in Engineering

ABSTRACT

During the steel-making process, scale is formed in the reheating furnace (on hot-rolled steel products) and is used to oxidize away some surface imperfections, but if the resultant scale cannot be removed prior to rolling (by the usual method of hydraulic descaling), then serious surface quality problems can arise. Experimental results are presented that test the hypothesis that the descaling behavior of slabs following reheating is controlled by interfacial roughening at the scale-steel interface. In this investigation, two stainless steels were considered: type 304 (austenitic, with 18% Cr and 8% Ni) and type 412 (ferritic / martensitic, with 11.6% Cr).

It was found that the entanglement that arose at the scale-steel interface was in fact effective in maintaining scale-steel adhesion, under the mechanical descaling conditions used. In the case of type 304, descaling proceeded by fracture along chromite layers, which formed on the austenite grain boundaries; for this steel, the extent of descaling depended most strongly on austenite grain size, and not primarily

on the conditions in the reheating furnace. In contrast, type 412 samples descaled only at the edge of the entangled zone, and showed a greater sensitivity to the reheating conditions.

Key terms: Interfacial morphology, reheated stainless steel, iron oxide, scale, mechanical descaling, reheating gas atmosphere, oxidation, surface quality, austenite grain structure, excess oxygen

INTERVLAKMORFOLOGIE EN ONTSKALING VAN HERVERHITTE ROESVRYSTAAL

deur

Nana-Araba Quagraine

Prof. PC Pistorius

Departement MateriaalKunde en Metallurgiese Ingenieurswese

Meestersgraad in Ingenieurswese

OPSOMMING

Gedurende die staalverwerkingsproses word skaal in die herverhittingsoond gevorm, wanneer platblokke voor warmwalsing verhit word. Skaalvorming word gebruik om oppervlakdefekte weg te oksideer, maar as die gevormde skaal nie voor walsing verwyder word nie, kan ernstige oppervlakgehalteprobleme ontstaan; die gebruiklike metode om die skaal te verwyder is om met hoëdrukwatersproeiers. Eksperimente is uitgevoer om die hipotese dat die onskalingsgedrag van herverhitte platblokke deur die ruheid van die skaal-staalintervlak beheer word, te toets. Twee tipes roesvrystaal is gebruik: tipe 304 (austenities met 18% Cr en 8% Ni) en tipe 412 (ferrities/martensities, met 11.6% Cr).

Dit is gevind dat verstrengeling tussen skaal en staal (by die intervlak) effektief was om die skaal aan die staal te heg gedurende warm meganiese onskaling. In die geval van tipe 304 het ontskaling deur kraking langs chromietlae wat op die austenietkorrelgrense gevorm het, plaasgevind; vir hierdie tipe staal was die omvang van ontskaling dus grootliks van die austenietkorrelgrootte afhanklik, en nie primêr

van toestande in die herverhittingsoond nie. In teenstelling het tipe 412-monsters by die buitegrens van die verstrengelde gebied ontskaal, en het ook 'n groter invloed van die herverhittingstoestande getoon.

Sleutelwoorde: intervlakmorfologie, herverhitting, roesvrystaal, ysteroksied, skaal, meganiese ontskaling, herverhittingsoondatmosfeer, oksidasie, oppervlakgehalte, austenietkorrelstruktuur

NOMENCLATURE

P (Pa)	Impact pressure of descaling jet
T	Temperature
ρ (kg/m^3)	Density of water
G (m^3/s)	Volume flow rate of water
t (m)	Thickness of jet
B (m)	Width of steel being descaled
v (m/s)	Speed of steel under jet
θ (^{0})	Angle of jet from vertical
ρ_s (kg/m^3)	Density of scale
α (°C^{-1})	Coefficient of thermal expansion of scale
C (J/kg °C)	Specific heat capacity of scale
E (N/m^2)	Elastic modulus of scale
k (W/ m °C)	Thermal conductivity of scale
x (m)	Thickness of scale
l (m)	Distance between through scale cracks
σ (J/ m^2)	Energy required to separate scale from steel
ε_c	Compressive strain to failure of scale
ε_T	Tensile strain to failure of scale
J (N/m^2)	Shear strength of scale / metal interface

LIST OF FIGURES AND TABLES

Figures

CONTENTS

1. INTRODUCTION

1.1. Background

During the steel-making process, scale is formed in the reheating furnace prior to hot-rolling and is used to oxidize away some surface imperfections, but if the resultant scale cannot be removed prior to rolling (by the usual method of hydraulic descaling), serious surface quality problems can arise. These quality problems appear to be important for both stainless and carbon steels.

Specific industry observations (by members of the Center for Iron and Steel-making Research at Carnegie Mellon University) which were used to determine the direction of this work are as follows: For stainless steels, difficult-to-remove scale forms on an 11.5% chromium stainless steel (similar to Type 409, but without titanium stabilization) at the reheating temperature of 1210°C, if the total reheating time is substantially longer than the usual 4 hour. This effect is reportedly not found for the Type 304 stainless steel. However, the scale on type 304 is also sometimes difficult to remove.

1.2. Problem

It is expected that scale removal is not only influenced by the thickness of the scale formed, but also by the micro-structural characteristics of the scale; i.e. the nature and distribution of the different phases present in the scale as well as the interfacial morphology of the scale. Roughening of the scale-steel interface during scale growth in the reheating furnace is expected to cause strong scale adhesion, leading to poor scale removal (by hydraulic descaling) prior to hot rolling. Thus the micro-structural characteristics have to be understood for efficient removal of the scale.

1.3. Objectives of investigation

The goals for this literature survey are to:

- Identify possible mechanisms for the formation of sticky scale
- Identify mechanisms of scale removal during hydraulic descaling
- Obtain information regarding the mechanisms of mechanical descaling

The objectives are then to allow scale growth under simulated reheating furnace conditions, where the temperature, gas atmosphere and mass transfer to the sample surface are controlled and then to assess scale adhesion at temperature.

1.4. Research methodology

1.4.1. Introduction

From the general observations above, the main parameters to consider in this study are the reheating conditions (time, temperature and gas atmosphere) and the steel grade (both major alloying elements and impurities). The underlying idea is that the nature of the scale-metal interface must affect the removability of the scale. Hence, possible mechanisms, which can lead to interfacial roughening, will be surveyed first, followed by observations on the mechanism of hydraulic as well as mechanical descaling.

1.4.2. Need for new methods

The importance of the descaling mechanism in this study concerns ways in which descalability may be evaluated in the laboratory. The usual method of using actual high-pressure sprays is not simple to implement in a laboratory. Thus simpler methods - for example, bending the sample around a set radius immediately upon removal from the furnace, and subsequently measuring the amount of scale remaining— may suffice. This of course, all depends on the nature of the descaling mechanism (mechanical or thermal).

2. LITERATURE SURVEY

2.1. Interfacial roughening mechanisms

2.1.1. Pure metals

2.1.1.1 VOID FORMATION AT THE SCALE-METAL INTERFACE

Both carbon and stainless steels generally oxidize by a cationic diffusion mechanism (Kofstad, 1988). As an example, the classical scale growth mechanism of iron is as follows: Iron is oxidized to Fe^{2+} at the scale-metal interface, releasing two electrons. Both the Fe^{2+} cation and the electrons travel through the scale to the outside atmosphere. At the scale-gas interface, the electrons react with oxygen (or other oxidants such as CO_2 or H_2O) to produce O^{2-} anions, which then react with the Fe^{2+} to form new FeO. In this way, the new scale forms at the scale-gas interface, while the iron atoms are removed from the scale-metal interface.

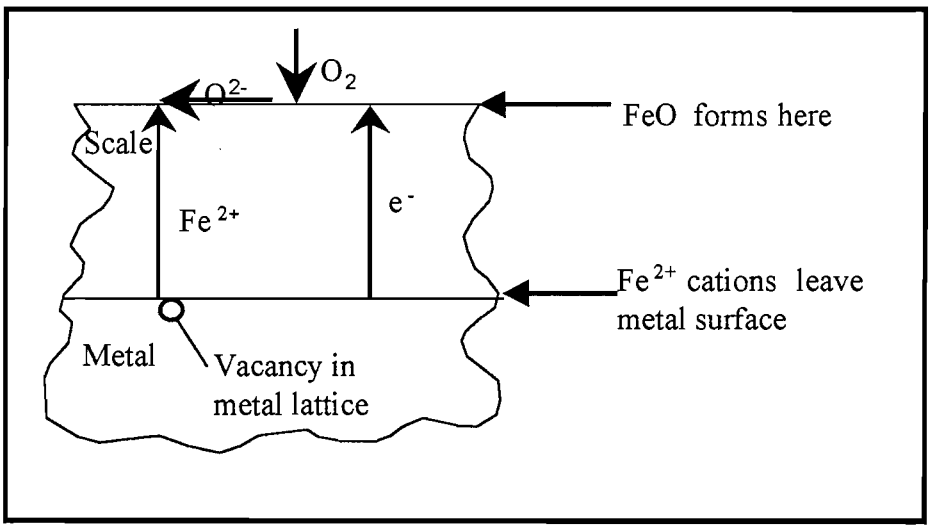

Figure 1: Schematic depiction of processes occurring during scale growth by cationic diffusion

At high temperatures, three oxides of iron are stable in the scale and form in parallel layers. The innermost layer with the lowest oxygen content is wustite (FeO) followed by magnetite (Fe_3O_4) and then hematite (Fe_2O_3). For oxidation in the temperature range 700-1250°C, the average FeO/ Fe_3O_4 / Fe_2O_3 thickness ratios were 95:4:1 (Sheasby, *et al*, 1984) (Ajersch, 1992). At lower temperatures (below 570°C), wustite is not stable and magnetite grows at the expense of the wustite (Sheasby ,*et al*, 1984).

2.1.1.2 RATE OF SCALE GROWTH

Initially after exposure of a base metal, the oxygen mass transfer to the outer scale surface controls the rate of scale growth since cation (Fe^{2+}) transfer is relatively efficient at small-scale thicknesses. The rate of scale growth is thus linear — the thickness of the scale formed is directly proportional to time and independent of the scale thickness. During this period, only FeO is present (appendix 1) up to a thickness of between 0.4 and 0.5 mm, beyond this thickness, the rate-controlling step becomes the arrival of Fe^{2+} at the interface. Then the scale growth rate changes from linear to parabolic, i.e. the square of the scale thickness is proportional to time, at constant temperature (Sachs and Tuck, 1968).

The initial scaling rates are reduced by reducing the oxygen input/fuel ratio to the furnace, thereby lowering concentrations of free oxygen in the combustion products from about 3 to 1.5 %. The predicted weight gains during reheating in the industrial reheat furnace indicate that oxidation rates during reheating are intermediate between linear and parabolic, especially during reheating with high oxygen/fuel ratio. (Abuluwefa, *et al*, 1997).

The classic Wagner theory (Rapp, 1984) predicts parabolic kinetics, if the oxidation rate is controlled by diffusion (of cations, in this case) through the scale — and good

agreement between actual scale growth rates and those predicted from diffusivities is indeed found, especially at temperatures higher than about 0.75 times the absolute melting point of the scale. This means the scale growth rate is often controlled by the rate of diffusion through the scale, which should serve to smooth any irregularities in the scale — since the scale thickens more rapidly at points where it is locally thinner. In this way, parabolic scale growth should imply a smooth scale layer, and hence a smooth scale-metal interface.

However, even in the case of pure metals undergoing parabolic scale growth, the basic scale growth mechanism can lead to roughening of the interface. As indicated above, cationic oxidation proceeds by continuous removal of iron atoms from the scale-metal interface, which means that vacancies are continually created in the metal lattice at this position. These vacancies are generally eliminated by climb of the misfit dislocations at the scale-metal interface (Rapp, 1993).

These misfit dislocations are present at the interface because of the epitaxial relationship between the scale and the underlying metal (i.e., with specific crystal planes and crystallographic directions of the scale parallel to those in the underlying metal) (Boggs, 1973; Rapp, 1984; Taniguchi, 1985; Pieraggi & Rapp, 1988). The dislocations are required to accommodate the misfit between the metal and scale lattices. If the process of vacancy elimination is somehow prevented, the vacancies can condense to form voids at the scale-metal interface — roughening that interface. Vacancy elimination can, for example, be prevented by the loss of epitaxy between the scale and the metal, or through immobilization of the dislocations by cations of "reactive elements" (such as yttrium) (Pieraggi, et *al,* 1995)

Void formation at the interface appears inevitable for the conditions during reheating. The extent of void formation is expected to increase as the extent of scaling increases, but it is not clear what the effect on descalability will be. On the one hand, voids may act as stress raisers, promoting loss of scale adhesion (Taniguchi, 1985). This may be an explanation for the observation that thinner scales (formed at lower

temperatures) on aluminum-killed steels are more difficult to remove by hydraulic descaling (Morris, *et al*, 1996). Conversely, because voids interrupt the movement of cations, scale growth slows down above voids causing the scale-metal interface to become uneven, which might in fact aid adhesion by a mechanical keying action (Kofstad, 1988).

Epitaxy may be lost if the metal undergoes a phase transformation (which disrupts the crystallographic relationship between the metal and the scale). This may play a role during the scaling of iron or carbon steel during heating, where a temporary reduction in the scale growth rate is observed when the temperature passes through approximately 900°C to 975°C, perhaps because the ferrite-austenite phase transformation causes separation between the scale and the metal (Sachs, and Tuck, 1970).

2.1.2. Alloys

2.1.2.1 INTRODUCTION

Interfacial roughening may occur when the alloying element (or impurity) is less likely to be oxidized (is more noble) than the iron matrix, or equally when it is more likely to be oxidized (is more reactive).

The general condition for interfacial stability, when one element in an alloy is considerably more reactive, and forms most of the scale (e.g. Cr_2O_3 formation on stainless steel) was stated by Wagner (1959). The qualitative result is that, if diffusion of the reactive element in the oxide is rate determining (for scale growth), the scale-metal interface is stable and should remain planar, whereas if diffusion in the alloy is comparatively slow, the interface is destabilized and roughens (due to internal oxidation leading to the formation of Cr_2O_3 in the metal substrate) (Gibbs, 1981). For iron-chromium alloys, a stable interface is only expected if the chromium content

exceeds a critical value, which is in the range of 13 - 25% (Hindham and Whittle, 1982) — thus commercial stainless steels (which have lower chromium contents) are generally expected to have unstable (i.e. roughened) scale-metal interfaces. This is experimentally observed for the oxidation of Fe-Cr alloys in oxygen (Whittle and Wood, 1967) and in water vapour (Fujii and Meussner, 1963, 1964). Thus some degree of interfacial instability is always expected for the stainless steels and certainly for the carbon steels, where the low concentrations of reactive elements (such as silicon, aluminum and manganese) imply that internal oxidation (Douglass, 1995) will be prevalent. Since some interfacial instability is expected, the question becomes what the effect of alloying elements and impurities will be on the extent (and physical size) of that instability. This is discussed in the following sections, classified according to the main mechanisms (fayalite formation, nickel enrichment, decarburization and internal oxidation), which are observed for commercial steels.

2.1.2.2 FAYALITE FORMATION

With high (> 0.25 %) silicon concentrations in the steel, a film of silica might form at the metal-oxide interface and thus slow the rate of scaling (Sachs and Tuck, 1970). Because an oxygen activity gradient exists between the scale and the metal, atomic oxygen diffuses from the scale into the steel and reacts with the dissolved silicon to form an internal precipitate of SiO_2 (Sachs and Tuck, 1970). FeO and SiO_2 form a eutectic system (with melting point around 1180°C); the eutectic composition is close to fayalite (Fe_2SiO_4) as shown in the figure below. This means that, for reheating temperatures greater than 1180°C, a liquid oxide is present next to the metal; this causes the interface to break down, apparently because the fayalite melt wets and penetrates the grain boundaries of the steel. The resulting inter-penetration of scale and metal renders the scale difficult to remove (Palin, 1965).

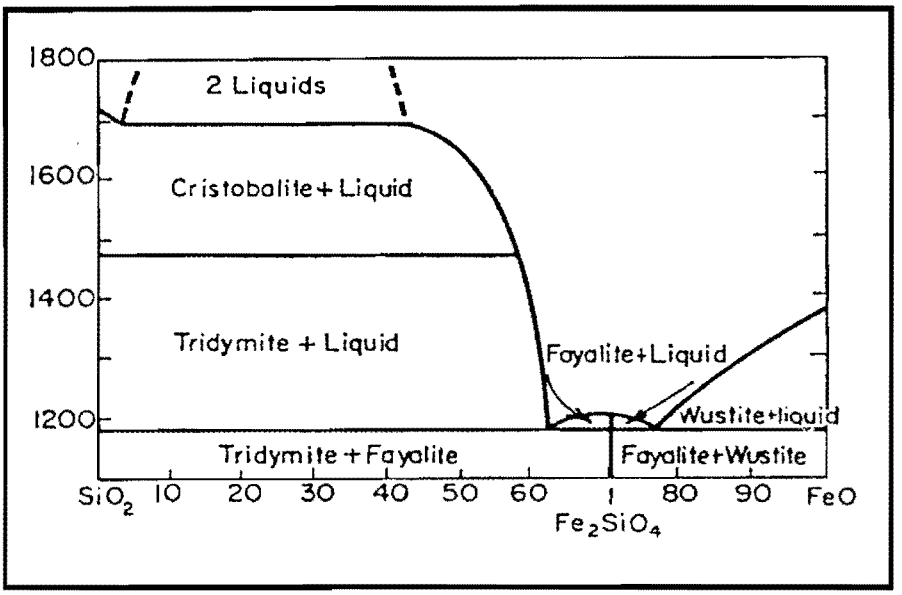

Figure 2 : SiO_2 - FeO phase diagram (Levin, et al, *1964)*

2.1.2.3 NICKEL ENRICHMENT

Nickel is less easily oxidized than iron and is thus rejected by the scaling reaction and is concentrated at the metal-oxide interface. Because nickel does not diffuse rapidly back into the steel, a discontinuous nickel-rich layer, which extends into the scale, is formed. The presence of Ni entanglement in the scale makes the scale adherent during rolling, so that it is sometimes forced into the metal, giving rise to surface defects (Zittermann, *et al*, 1982). Ni in steel having a bulk Ni concentration of 0.14% segregates in the sub-scale to a concentration as high as 5-6% after oxidation. Increasing the Ni content may result in extensive internal oxidation and the appearance of a Fe-Ni spinel phase next to the oxide-metal interface (Boggs, 1973).

2.1.2.4 INTERNAL OXIDATION

Internal oxidation of elements, which are more reactive than iron may occur within the metal behind the metal-scale interface, by reaction with oxygen. This results in oxide particles distributed within the metal grains. For example, in the case of stainless steels with high Cr contents, a protective film of Cr_2O_3 is formed which inhibits the outward diffusion of Fe. However, the film often breaks down and a spinel ($FeCr_2O_4$) forms at the scale-metal interface, which allows some oxidation to occur, although the rate is much slower than with ordinary steels (Fujii and Meussner, 1964).

2.1.2.5 DECARBURIZATION

In general, the oxidation rate of steels is much slower than that of pure iron and it is not easy to establish which component is responsible for this effect. Carbon is peculiar in that it forms a gaseous reaction product. The main effect of carbon on oxidation rates is to make the rates more erratic. Thus carbon reacts with the iron oxides to produce CO and CO_2. A concentration of CO or CO_2 in pores in the scale might cause cracking leading to an increase in the scaling rate. On the other hand, the gases might fill the gaps and voids, thus preventing healing of the defects and slowing the rate of oxidation (Sachs, and Tuck, 1970). Even very low carbon contents are sufficient to cause some pores to form at the interface; the pores are only absent if the carbon content is lower than 50 PPM for the oxidation of carbon steel at 950°C (Sheasby, *et al*, 1984).

2.1.2.6 IMPLICATIONS FOR THIS WORK

It appears likely that all of the mechanisms briefly surveyed here — fayalite formation, entanglement due to interfacial enrichment with nobler elements, carbon monoxide bubble formation, and internal oxidation — will be present to some extent

under the reheating conditions considered in this work. Two likely exceptions are CO formation in the case of stainless steels and fayalite formation in the case of aluminium-killed steels— but even with these excluded, several mechanisms leading to interfacial roughening are expected to operate simultaneously. As a result, the descalability of stainless steels is expected to depend strongly on their composition, and especially the level of impurities (with both noble and reactive impurities being important). It also means that it will probably be impossible to assign causes of interfacial roughening or poor descalability to a single factor. The implication is that the steel grades, which are to be used in the experimental work, need to be chosen with care.

2.2. Descaling

2.2.1. Introduction

The two legs of this project are the development of the interfacial morphology and the effect of this morphology on the behaviour during descaling. This section deals with the mechanism of hydraulic descaling. A typical plate mill plant-descaling rig includes a pump, which is driven by an electric motor. The typical pump pressure used is about 0.7 MPa (Iscor Vanderbijlpark). High pressure water is delivered by the pump to a header bar over the steel, from which water is sprayed through a series of nozzles. Both pump and motor are fitted to a base frame mounted on anti-vibration mountings (Morris, *et al*, 1996).

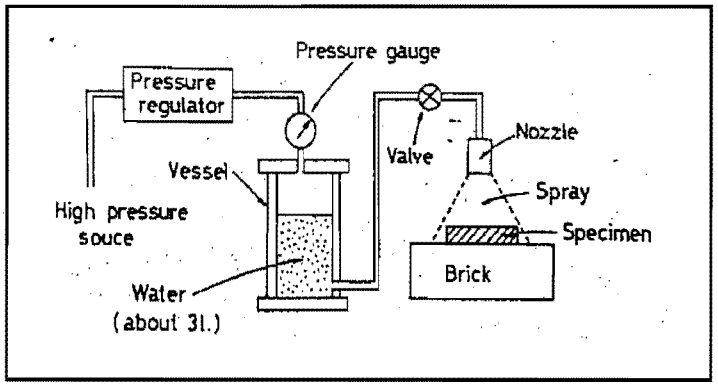

Figure 3 : Diagram of set-up during hydraulic descaling (Matsuno, 1980)

2.2.2. Header diameter

Larger diameter (150 mm) header pipes with the same water pressure and flow rate have lower water velocities and thus, less turbulent flow than smaller diameter headers. Less turbulence produces better descaling action since more kinetic energy remains in the spray. Modern descaling systems attempt to achieve an optimum velocity of 1.2 meters a second in the header (Grigg, *et al*, 1985).

2.2.3. Nozzles and attachments

The nozzle system consists of a welded steel body, with a long tapered bore to promote smooth water flow, a replaceable nozzle tip and a threaded locking nut to retain the tip. The orifice tips should be self-aligning to ensure a consistent offset-angle and the orifices should be made of tungsten carbide to increase the working life (Grigg, *et al*, 1985).

The impact pressure is a maximum when the nozzle impact angle is vertical because a scouring action is produced on chipped scale, which removes the scale. The main benefit from inclining the nozzle towards the approaching steel is that detached scale is directed away from the rolling stand. An elliptical orifice results in better descaling because a relatively constant impact pressure across the jet width can be maintained. The water jet width and thickness increase linearly with nozzle height. The impact pressure of the jet increased linearly with system pressure (Sheridan and Simon, 1995).

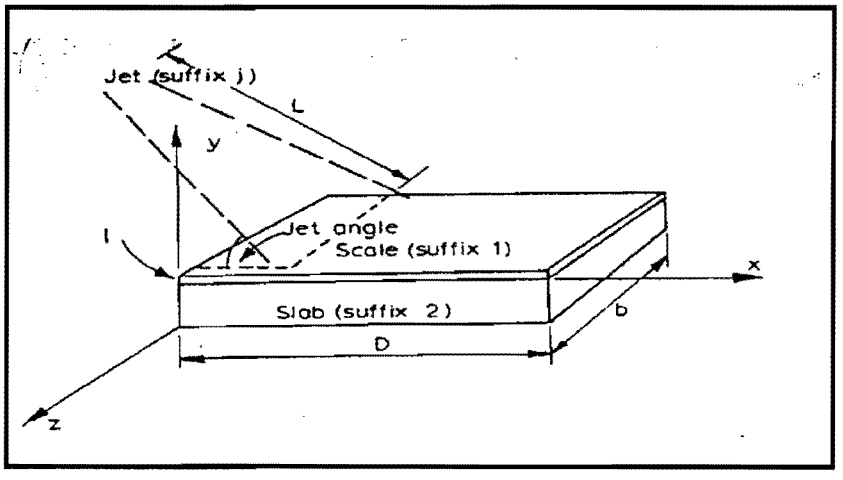

Figure 4 : Diagram indicating offset angle of cooling jet (Sheppard, and Steen,1970)

Figure 5 below gives as a function of the nozzle diameter:

- $Q_c.f_c$ or the actual descaling capacity of the nozzle which is the flow rate through coherent part (orifice) of nozzle Q_c (litre/m^2) multiplied by the actual momentum flux density f_c (MPa) ; (f_c is the jet force divided by the jet cross sectional area)
- $Q_c.f_c$ / ($Q_t.f$) or the efficiency of the nozzle, i.e. the ratio between the actual descaling capacity at the impact and the theoretical descaling capacity, which is equal to the total flow rate of the nozzle Q_t multiplied by the theoretical jet momentum flux density.

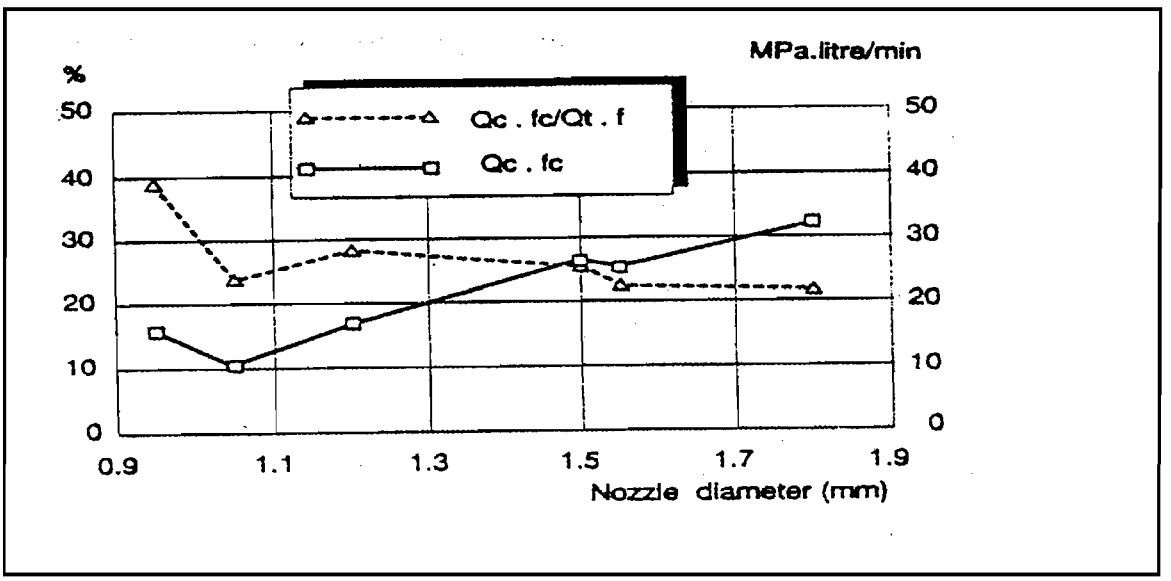

Figure 5 : Influence of nozzle diameter (Sheridan and Simon,1995)

The descaling capacity increases with the nozzle diameter but the efficiency is better for smaller nozzles. Thus it is better to use a larger number of nozzles of smaller diameter with a reduced pitch between the nozzles.

2.2.4. Distance and water pressure

The distance between the nozzle and the steel surface should be as small as practically possible and the delivered water pressure should be maximized to ensure that sufficient descaling is obtained in the shortest time possible. Raising the jet velocity considerably increases the descaling efficiency that is until the change in

pressure across the spray nozzle attains a value of 400 kN/m^2 (0.4 MPa), when no significant increase in efficiency occurs (Sheppard and Steen, 1970).

2.2.5. Effect of scale temperature

The effect of scale surface temperature on the efficiency of scale removal originates in the crack initiation and propagation behavior during air-cooling. When scale formed at high temperature is subjected to air-cooling, tensile stress is developed at the scale surface resulting from thermal contraction. When this tensile stress exceeds the fracture stress of the scale, the cracks initiated at the scale surface continuously propagate towards the scale-metal interface (Fukutsuka, *et al*, 1981). The scale surface temperature influences the removability of especially the scale on the silicon-killed steel slabs.

2.2.6. Mechanism of high pressure water descaling

2.2.6.1 INTRODUCTION

Two principal effects may predominate, namely thermal effects as a result of water-cooling, and secondly, the mechanical effect of the water jet in striking the steel, thereby breaking the scale and removing it by direct force. The hydraulic removal of the scale is dependent on both the impact pressure and quantity of applied water per unit area. The total stress produced in the scale by descaling is the sum of the thermal stress produced by the cooling action of water jets, the stress due to the impact force of the jet and the depositional compression stress (the oxidation stress). The amount of stress in the scale is closely related with the hydraulic scale removal (Matsuno, 1980). The importance of the descaling mechanism in the present work concerns ways in which descalability may be evaluated in the laboratory. If there is no clarity on the descaling mechanism, there is no alternative to using actual high-pressure water sprays (which is not simple to implement in a laboratory). However, if the mechanism is primarily mechanical, simpler methods — for example, bending

the sample around a set radius immediately upon removal from the furnace, and subsequently measuring the amount of scale remaining (as used by Tuck and Barlow [1972]) — may suffice.

2.2.6.2 THERMAL EFFECTS

The difference in temperature between the descaling water and the scaled steel or between the atmosphere and the scale when the steel is removed from the furnace is such that a thermal gradient can exist within the scale leading to thermal contraction of the surface of the scale. This causes the scale to curl and break away from the steel, i.e. the thermal shock created by the high energy impact breaks the scale and the short contact time limits the temperature drop of the product (Sheridan and Simon, 1995). The depth of scale, which would experience cooling as a result of the effects of the water jets, is only about 0.2 mm (as calculated in appendix 2).
Reducing the sample speed under the descaling spray increases the effective volume of the water applied to a given area of steel, reducing the temperature further and increasing the descaling action. The formation of steam, leading to disruption of the scale, may be capable of supplying sufficient energy to the scale to fracture the metal / scale interface. This mechanism depends however on the ability of the water to penetrate pores and fissures within the scale and thus produce an undercutting effect.

2.2.6.3 MECHANICAL PRESSURE EFFECTS

When considering the mechanical pressure effects on the other hand, it is noted that the force exerted by the water jets on the surface of the scale can produce displacement of the scale if porosity or detachment exists as a result of either scaling conditions or thermal contraction effects. This mechanism would be expected in friable scales, and would be of increased effectiveness at higher water pressures. In addition, the force of the water jet on the scale may crush and fragment the scale,

following which the pieces of scale are removed by the water. In practice, these mechanisms may all contribute to scale removal:

· The stagnation pressure of the water jet forces water beneath the scale

· The generation of steam undermines and ruptures the scale

The figure below illustrates that, for low-carbon aluminium-killed steel, successful descaling relies on the impact pressure being high enough, supporting the mechanical removal mechanism. However, in the case of steels which are more difficult to descale - such as those containing significant amounts of nickel or silicon - a trade-off between impact pressure and the total amount of water is found: as the figure shows, successful descaling of the high silicon steel requires an impact pressure of 1.5 MPa at a lower water consumption (i.e. shorter dwell time beneath the jet), but successful descaling is obtained at an impact pressure of 0.5 MPa if more water (longer time) is used at 25 l/m^2 specific water flow rate.

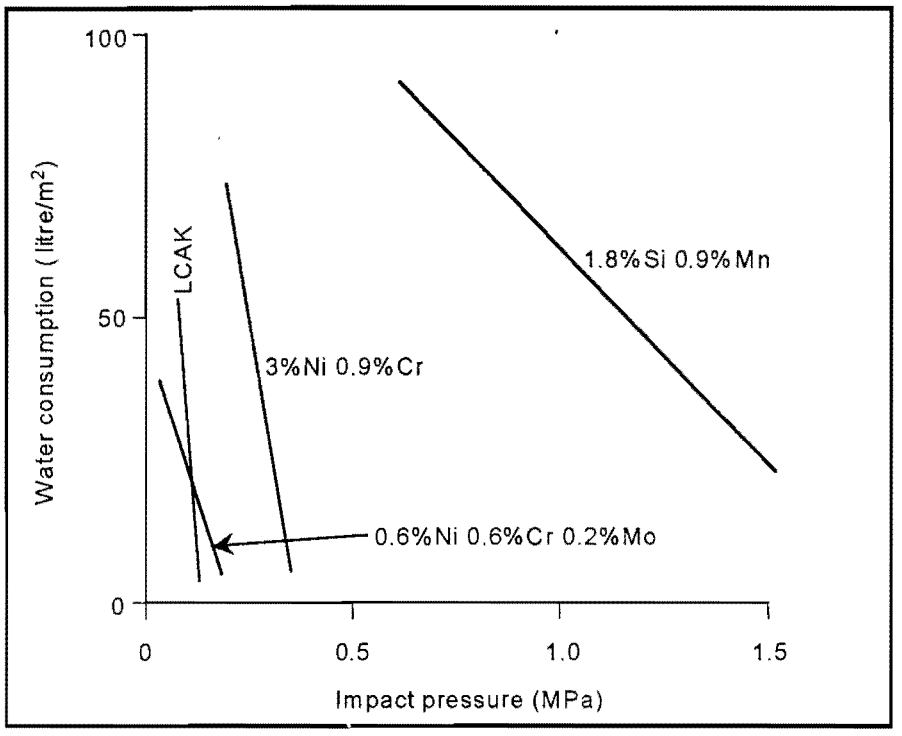

Figure 6 : Conditions required for successful descaling of four steel grades(low-carbon aluminium-killed steel, and 3 alloy steels). Descaling is successful if the actual jet impact and water consumption lie to the right of the relevant line. (Sheridan and Simon, 1995)

However, the effect of time suggests that a comparatively slow process - such as heat transfer through the scale, may contribute to descaling of these steels. The envisaged role of heat transfer is to quench the scale, causing it (or its outer layers) to contract, scale failure being the result of thermal shock (Sheridan and Simon, 1995). The pressure and time required to obtain successful descaling for given reheating conditions could be related by the parameter $\Delta pt / l^2$ — where Δp is the header pressure, t the time allowed for descaling, and *l* the scale thickness. The dependence on the square of the scale thickness is in accordance with the control by heat conduction through the scale (Sheppard and Steen, 1970).

In further indirect support of a possible role of thermal shock, Fukutsuka, *et al* (1981), ascribed the poorer descaling of silicon-killed steel to the great prevalence of through-thickness cracks in the scale on this steel — these cracks can give stress relief during cooling (Tominaga, *et al.*, 1982), so improving the resistance to thermal shock.

However, some quantitative indication of whether thermal shock is a feasible mechanism can be obtained by estimating the time required to cool the scale to a given depth. Assuming that conduction through the scale is rate determining, the time to cool the scale is of the order of l^2/α, where l is the scale thickness and α, the thermal diffusivity. Using literature values for the thermal conductivity and density of wustite (Akiyama *et al.*, 1992) and its heat capacity (FACT, 1998), the thermal diffusivity is estimated to be some $8.3*10^{-7}$ m^2/s in the vicinity of 1100°C. Based on the typical thickness of the jet of around 8 mm, and slab speeds of 0.1 to 1 m/s (Morris, *et al*, 1996), the time that the scale is exposed to the water jet is between 8 and 80 ms — which, based on the thermal diffusivity, is only sufficient time to quench the outer 80 - 250 μm of the scale (compared with the total scale thickness which may be 2 mm or more after reheating). This very limited cooling of the scale does bring the validity of the thermal shock mechanism into doubt (appendix 2).

This is further illustrated in cases where larger pieces of scale are observed upon their removal from the slab at the descaler. It is observed that the surface, which had been in contact with the steel, still glows red-hot, indicating that the full thickness of the scale had not been cooled down - suggesting that thermal shock was not effective. In addition, the observed removal of scale at positions up to several millimeters ahead of the jet also suggests a mechanical action (Blazevic, 1987).

Thus it does seem that the mechanism of hydraulic descalers is largely mechanical and that a mechanical means of descaling at temperature should yield an adequate simulation of in-plant hydraulic descaling.

2.2.7. The effect of interfacial roughening on descaling

According to Asai, *et al.* (1997), the effect of impurities on the removability of primary scale on 0.02 and 0.1 mass percentage Si mild steels was investigated using hydraulic descaling tests and the results were as follows:

- The scale / metal interface becomes uneven for steels containing a small amount of Ni ranging to 0.05 mass %, and the unevenness is independent of oxidation temperature as well as Si content of steel. Thus the removability of primary scale reduces by an addition of a small amount of Ni. However, comparing the residual thickness of 0.05 and 0.1 mass % Ni steels, the thickness of both was almost equal (Asai, *et al*, 1997).

- The cause of poor descaling in Si-added steel has been explained so far in terms of the fact that the impact by high-pressure water spray is reduced by the existence of molten eutectic compound (fayalite) between steel and scale. The fayalite increases the unevenness of the interface thus leading to poor descaling.

The qualitative indications are that steels with roughened interfaces, whether as a result of nickel enrichment or of fayalite formation, are more difficult to descale. However, it is not clear whether interfacial roughness correlates in a quantitative way with descalability or even what an appropriate way of quantifying the interfacial roughness is.

In one study, the interfacial roughness was quantified by determining the length of the scale-metal interface relative to a smooth interface (expressed as a ratio) (Asai, *et al*, 1997). This roughness index was determined by examining cross-sections under an optical microscope. Some of the results are shown in figure 6 below. This figure (redrawn from the data of Asai, *et al*, 1997) indicates the amount of residual scale after hydraulic descaling, together with the measured roughness index, for

steels with low and high nickel and silicon contents, which had been reheated at 1100°C and 1200°C in air. The figure shows the expected effect of silicon and nickel to increase the interfacial roughness and that descaling is less efficient if the interfacial roughness is larger.

This work does indicate that this simple roughness index might be useful but also hints at its limitations. For example, the figure shows that the higher-nickel higher-silicon steels which had been reheated at 1200°C had (as expected) the worst descaling behavior, but their roughness index was similar to that of steels with less silicon, and of the same composition reheated at the lower temperature. This suggests that something more than just the roughness index may be required. A contender could be a measure of the absolute size of the roughness (Asai, *et al*, 1997).

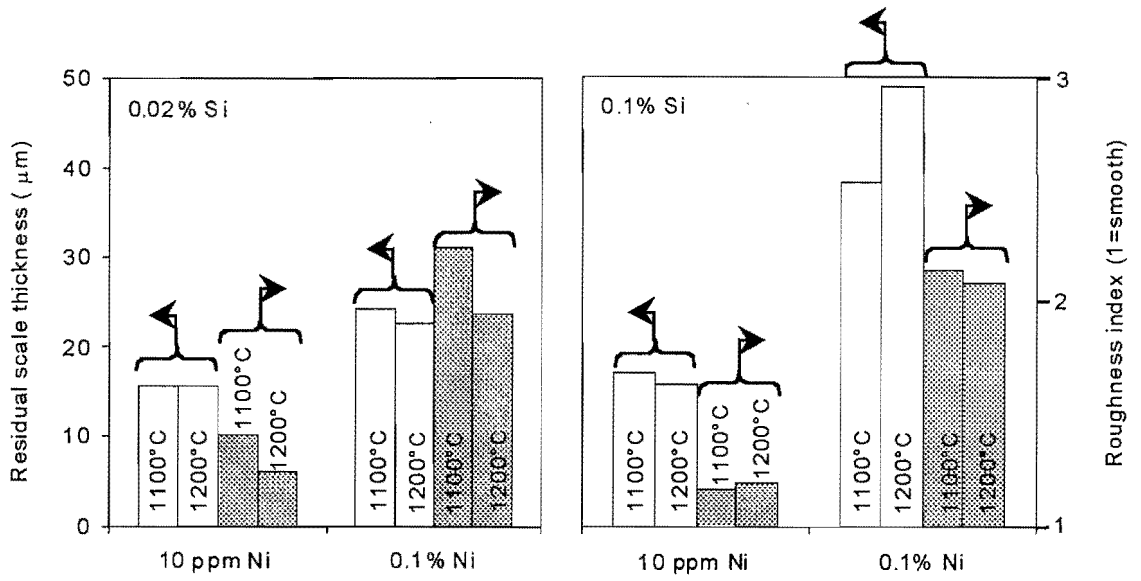

Figure 7 : Effect of steel composition and reheating temperature on the interfacial roughness and descaling behavior for steels containing 0.02% or 0.1% Si, together with 10ppm or 0.1 Ni %. The clear columns give the average thickness of scale remaining after descaling (plotted against the left-hand axis), and the shaded columns give the relative roughness of the scale-metal interface (right-hand axis) (Asai, et al, 1997).

2.2.8. Mechanical Descaling

The above arguments indicate that the action of hydraulic descalers is largely mechanical. And as stated, this means that a mechanical means of descaling at temperature should yield an adequate simulation of in-plant hydraulic descaling. A number of papers relating to mechanical removal of the scale on stainless steel coils have been published (Liekmeier, 1982; Tuck, *et al,* 1972; Garceau, 1997; Ito, *et al*, 1997 and Fresnedo, *et al*, 1996). However apparently no systematic research has been performed on mechanical descaling methods therefore, an optimal descaling method has not yet been established.

The principle basically is to remove the relatively thick shield of coarse oxide by deforming the sample whilst still hot (i.e. approximately at the furnace temperature [1200°C]). This latter requirement is in contrast with available commercial mechanical descaling methods, where the samples are allowed to cool to room temperature before descaling (Engell and Peters, 1957). Tuck and Barlow (1972), used a hot bend test to assess the quantity of adherent scale remaining on a particular specimen after being deformed at the furnace temperature. A simple test rig was designed and built to bend hot specimens by a constant deformation of approximately 32 mm at their center. This degree of deformation was sufficient to remove some of the scale but not all. Thus after oxidation, each specimen was removed from the furnace, immediately bent in the jig and allowed to cool naturally. Loose scale was removed from the convex face, the specimen weighed and the convex face shot blasted to remove the fine shield of oxide that is very firmly adhered to the steel surface.

The force required to deform the specimens (100mm x 50mm) in this project was calculated to be 2.5kN (section 3.3). Thus the impact pressure of the mechanical descaler was 0.5 MPa (force / Area). Using equation A3.2 in appendix 2, the compressive strain exerted was calculated to be 2.6×10^{-6}. This value is of the same order as the calculated compressive strain (5.3×10^{-6}) for a typical commercial

hydraulic descaler (calculations shown in detail in appendix 2). Based on these calculations, it can be assumed that mechanical descaling is likely to yield the same results as hydraulic descaling.

However, depending on the amount of scale and the surface roughness of the steel, the crust can be easy or difficult to remove by the mechanical descaling process. But regardless of the amount or nature of the scale, it should be completely removed if the quality of the steel is to be maintained.

2.3. Reheating temperature

While high reheating temperatures (giving thicker scales) were found to increase scale adhesion, especially for silicon-killed steels, this was not observed for all grades (Palin, 1965). For aluminium-killed steels, lower reheating temperatures gave thinner scales, which were more difficult to remove (Morris, *et al.,* 1996) whereas steels susceptible to entanglement (silicon and nickel-containing steels) developed more entanglement at higher temperatures, with a negative effect on descalability. An indication of the complex effect of reheating temperature is given by the results of Sheppard and Steen (1970), which are redrawn in figure 8 below. This figure shows a combination of header pressure (Δp) and time (t) required to remove a scale of thickness *l*, for different reheating temperatures —clearly scales formed at 1000°C are more difficult to remove than those formed at both higher and lower reheating temperatures.

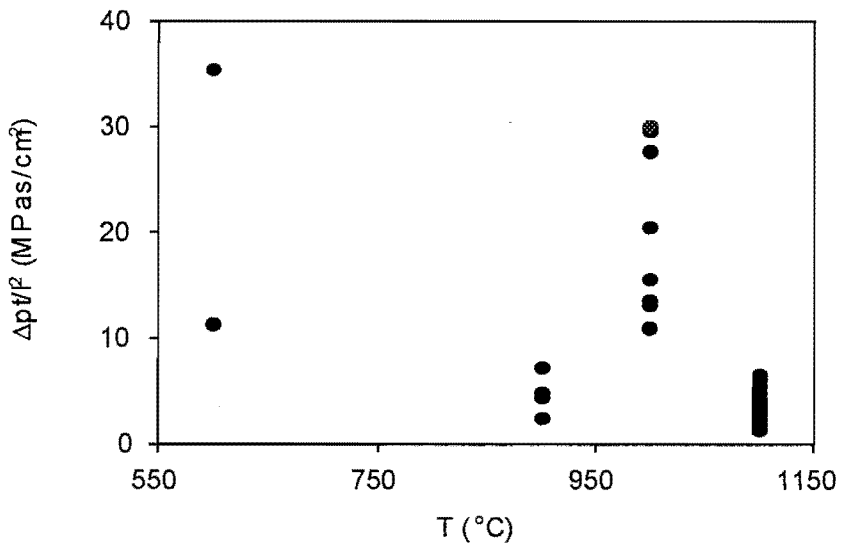

Figure 8 : Combinations of header pressure (delta P) and time (t) required to remove scale with thickness l from carbon steel which had been reheated at different temperatures.

In addition to the nominal reheating temperature, the temperature cycle to reach this is expected to be of importance. For example, Fukutsuka *et al. (1981)*, found that the amount of residual scale on slabs following descaling did not correlate well with either reheating time or temperature alone, but best with an integrated "degree of overheating" (DOH). DOH was defined as follows:

$$DOH = \int_{t_o}^{t_e} (T - T_0)dt$$

Where T_o is the critical temperature for overheating (1100°C yielded the best results), t_o is the time when the slab reaches T_o, and t_e is the time when the slab is removed from the furnace.

In addition to the thermal history of the slab as it reaches the reheating temperature, possible fluctuations in the surface temperature are expected to affect the scale — Abuluwefa *et al.* (1997b) found more cracks in the scale on samples which had passed through an actual reheating furnace, compared with samples exposed to nominally the same thermal cycle and atmosphere under laboratory conditions. The cracks were ascribed to temperature fluctuations in the furnace (temperature cycling is indeed a well-established method to induce cracking of oxide scales [Schutze, 1995]).

2.4. Reheating time

The plant observation that the descalability of the 11.5% chromium stainless steel is severely reduced by extended reheating emphasizes the importance of this variable. While this observation suggests a monotonic decrease in descalability with increased reheating time, this is not always the case. For carbon steel slabs, the amount of residual scale after descaling increased with reheating time, but peaked at just over two hours, dropped to a minimum at 2.5 hours, and then increased again. Hence time was varied in the first number of experiments, whilst keeping to the typical reheating temperature profiles used in stainless steel plants (Palin, 1965).

2.5. Composition of gas atmosphere

2.5.1. Effect of water vapour

In oxidizing gas mixtures containing water vapour, the scale remained attached to the metal surface for considerably longer reaction times than in the absence of vapour, and the scale growth progressed in accordance with the parabolic rate for pure Fe (Sheasby, *et al*, 1984). This might imply that the presence of water vapour in the oxidizing gas enhanced the rate of creep in the scale and thus increased the rate of scale growth. Pores which developed (probably due to mechanical cracking) at the metal / scale interface in the presence of water vapour migrated away from the interface as the oxidation progressed. In the scales formed on the Fe-C alloys the pores migrated into the wustite layer and became larger. When H_2O was absent, the scale was detached from the metal, preventing further Fe transport across the scale. However, oxidation continued in the detached FeO and Fe_3O_4 resulting in a thinner layer of FeO and thicker layers of Fe_3O_4 and Fe_2O_3. Thus the presence of water vapour in the laboratory furnace atmosphere is essential to achieve scale growth that is comparable to that in the reheating furnace (Sheasby, *et al*, 1984). To obtain a product gas containing 3% excess oxygen for example, the other components of the gas mixture can be calculated by a mass balance and based on these calculations; about 16% water vapour is required in the gas mixture (appendix 3).

2.5.2. Effect of oxygen

The amount of free oxygen has a strong effect on the scaling of carbon steels apparently because the initial period of scale growth (lasting an hour or more) often exhibits linear kinetics, where the scaling rate is limited by gas-phase oxygen diffusion to the scale surface (Abuluwefa, *et al*, 1996, 1997a). Despite this, the

extensive study of Morris *et al.* (1996) did not find a large effect of excess oxygen (in the range 1-6%) on the descalability of carbon and low-alloy steels. Whilst it appeared important to test possible effects of the amount of excess oxygen, in the initial experiments gas atmospheres with 3% excess oxygen were used – this appeared to be typical of many reheating furnaces. Because of probable mass transfer control (for the initial scaling of carbon and stainless steels), the gas flow rate across the sample should be controlled to yield similar mass transfer constants to those encountered in a reheating furnace. Control of the gas flow rate is important in the case of stainless steels also due to the formation of the volatile species CrO_3, which is expected to form at temperatures above 1000°C (Stearns *et al*, 1974).

2.6. Surface finish

During oxidation studies, ground or polished surfaces are often used, to provide a reproducible starting condition. However, the nature of the surface finish can affect the scaling process. For scales which grow by cationic diffusion, the new scale grows on top of the old, which implies that the original surface finish is trapped at the scale-metal interface. Only in the case of extensive internal oxidation is the surface finish expected to be less important (Boggs, 1973). In this project, hot-rolled plate samples were used and thus the samples had the same surface finish and starting condition.

2.7. Effect of cooling conditions after descaling

The microstructure of the scale cross-section is greatly affected by the rate of cooling of the samples in the case of carbon steel. If wustite is the only phase formed in the early stages of oxidation, the wustite layer decomposes and oxidizes to form relatively thick hematite and magnetite layers during slow cooling of the sample (Sheasby, *et al*, 1984). Thus, the slower the cooling rate the greater the volume fraction of higher oxides in the scale.

3. Experimental techniques

3.1. Introduction

The experimental configuration to grow the scale as constructed at the University of Pretoria, is similar to the Cahn microbalance (the same equipment as used in the CISR work previously performed by Bahri Ozturk and Arianna Morales). The experimental approach contains the following elements:

- Scale growth under conditions of gas atmosphere, gas flow rate and temperature which simulate reheating conditions, using large samples to avoid edge effects.
- Mechanical descaling of the hot samples
- Assessment of interfacial roughness and the amount of residual scale by examining sample cross-sections by scanning electron microscopy (SEM).

3.2. Experimental set-up (Scale growth)

3.2.1. Gas system set-up

The gas composition was chosen to simulate the combustion product of methane (CH_4) with air, with 3% or 4% excess free oxygen. The total gas flow rate was 4Ndm^3 per minute, which was selected to give similar mass transfer conditions (which depend on the Reynolds number) to industrial furnaces. A schematic representation of the gas system is depicted in figure 9. The gas system contained three separate gas lines for N_2, O_2, and CO_2. The gases used were chemically pure CO_2 (99.0% minimum purity), chemically pure O_2 (99.5% minimum purity) and chemically pure N_2 (99.5% minimum purity). The nitrogen gas was stripped of any excess moisture by passing the gas through a drierite (anhydrous $CaSO_4$) column. The three gas lines were then joined before the gas mixer, after the flow rates had been set.

The gas flow rates were measured and controlled by rotameters, which were calibrated using a bubble-meter. In-line calibration of the rotameters was required to establish the exact flow rate of the gas mixture because a backpressure in the gas line would affect the flow rate.

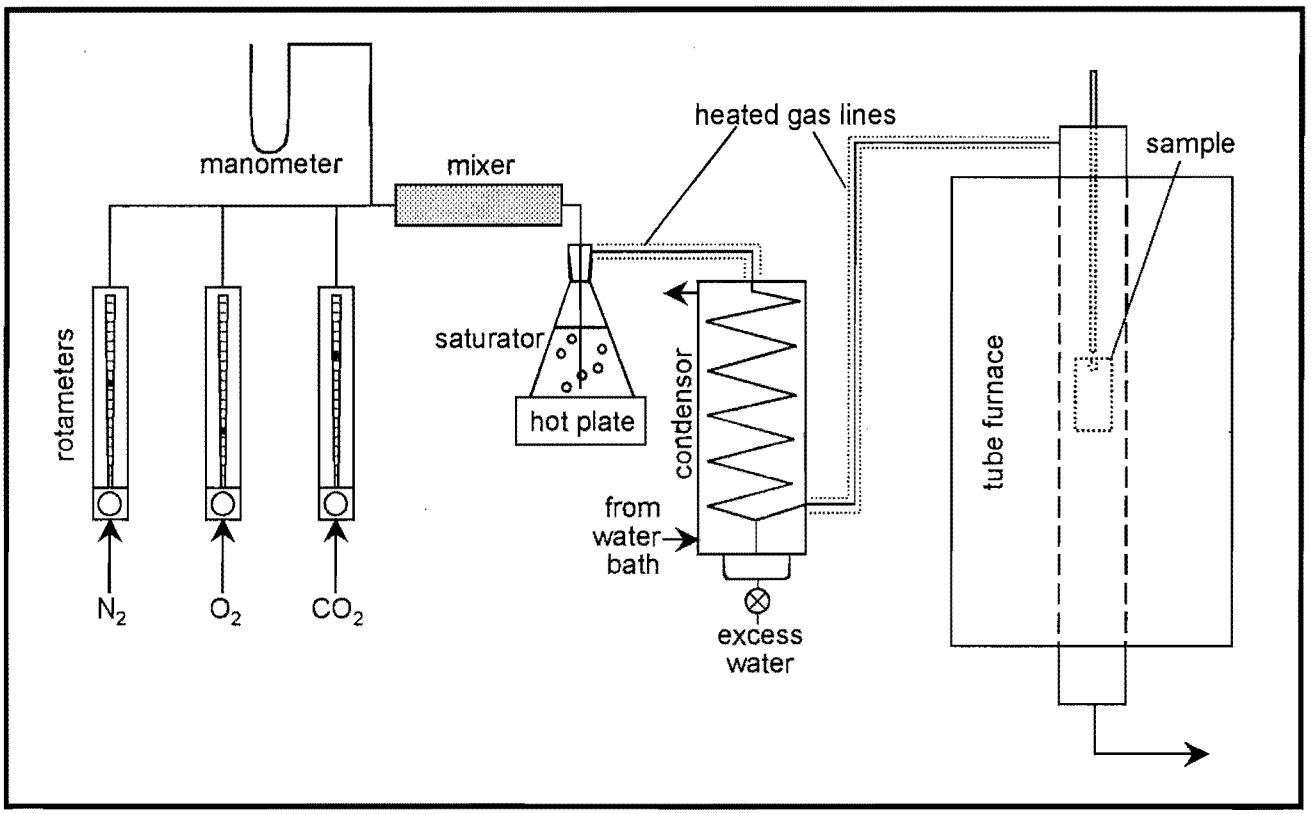

Figure 9 : Experimental configuration used to grow scale under simulated reheating furnace conditions

For this calibration purpose, the outlet from the furnace bottom at the end of the gas system was connected to the bottom of the bubble meter cylinder. The gas was introduced into the bottom of the apparatus, displacing a soap bubble along the length to the top end of the cylinder. A stopwatch was used to establish the time required for one bubble to traverse an indicated volume. The flow rate of the gas was thus calculated by dividing the amount of divisions (cm^3) which the bubble moved by

the time (s) taken for the displacement. This measurement was repeated about six times to establish a good average value for each rotameter setting.

The inlet pressure into the rotameters was measured by a mercury manometer, thus indicating the backpressure relative to the atmosphere. Rotameter corrections for gas density were done since changes in gas density could significantly affect the airflow measurements by rotameters. Using a rotameter at a pressure different than that for which it was calibrated, could yield serious error. The rotameter corrections are shown in detail in appendix 3.

The gas mixer consisted of a glass cylinder filled with glass beads in order to facilitate turbulent flow of the gases through the cylinder for proper mixing of the gases. The gas mixture then entered a saturator — that was basically filled with water kept close to its boiling point. The gas mixture was thus saturated with water vapour. By passing the mixture through a controlled-temperature glass condenser (figure 10), the excess water in the mixture was stripped.

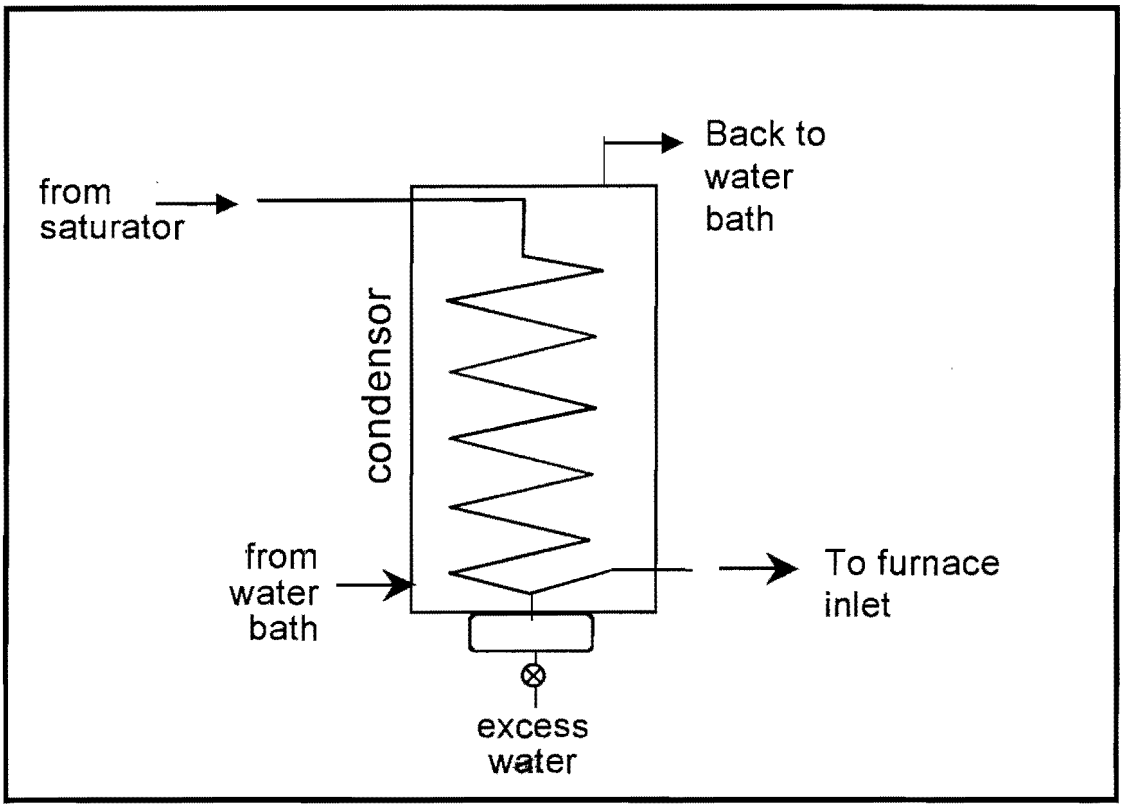

Figure 10 : Figure of temperature-controlled glass condenser

The temperature of the water circulating in the outer section of the condenser was kept at 60 ^{0}C. Control of this temperature was achieved by using a water bath, which was fitted with a pump that enabled the bath to be used as a circulator. The heater power of the bath was 1.4 kW, with a stability of approximately 0.1 ^{0}C. To ensure that any excess vapour in the mixture would condense, the mixture exited the condenser at angle and was fed into the furnace. A three-way brass valve was fitted between the condenser exit and the furnace inlet. A heavy insulated heating tape with a knitted heavy Fibrox fabric covering (Barnstead Thermolyne) was used to heat all the connections between the water saturator and the furnace. The variable transformer controlling the heating tape temperature was set at 135V to ensure that the temperature of the heating tape was approximately 80 ^{0}C.

Silicon rubber tubing was used for all the connections between the regulators and the glass-condenser. PFA- tubing (Swagelok) was used for the connections between the

three-way valve and the furnace simply because the hardness of the tubing made wrapping the heating tape around it easier.

The gas system was checked for leaks by filling the gas system with He and checking for leaks with a He-detector, one section at a time.

3.2.1.1 REQUIRED GAS FLOW RATES IN FURNACE

The specimen size and furnace bore diameter, were used to fix the minimum required gas flow rate through the furnace, to ensure that oxygen mass transfer to the scale surface was sufficient to yield the required oxidation rate. The results of calculations of the required gas flow rate are presented below, to show that these can be feasibly obtained in the large-bore tube furnace. The calculations were based on the combustion product of methane with air, to yield a product gas containing 3% excess oxygen; the other components of the gas were calculated by a mass balance to be 73% N_2, 16% H_2O and 8% CO_2. The report of Abuluwefa, *et al.* (1996) indicates that the initial rate of mass gain of the carbon steel samples during reheating at 1200°C is 1.7×10^{-4} kg/m^{2}s. The required oxygen mass transfer constant to match this rate is defined by the expression for the mass-transfer-controlled reaction:

$$K = m_{O_2}(C_{O_2}^{g} - C_{O_2}^{int}) \qquad (1)$$

Where K is the rate of mass gain (in kg/m^{2}s), m_{O_2} is the mass transfer constant of oxygen in the gas phase (in m/s), and C_{O_2} is the concentration of oxygen (in kg/m^3), where the superscripts "g" and "int" refer to the gas stream and the gas-scale interface respectively. Assuming $C_{O_2}^{g} >> C_{O_2}^{int}$, and taking $C_{O_2}^{g} = 6.7 \times 10^{-3}$ kg/m^3 (valid for a 3% oxygen mixture, at the typical reheating temperature of 1500 K, and atmospheric pressure of 0.865 atm), the required mass transfer constant of oxygen is calculated to be m_{O_2}=0.025m/s. This mass transfer constant is obtained by controlling the gas flow rate to yield the appropriate Reynolds number, as shown by the expression below (Abuluwefa, *et al,* 1996):

$$m_{O_2} = (4D_{O_2}/3L)\,(Re)^{1/2}(Sc)^{1/3} \qquad (2)$$

Where D_{O_2} is the diffusion coefficient of oxygen in the gas mixture (taken to be 3.27×10^{-4} m^2/s [Turkdogan, 1980]), L is the sample length (0.1m), Re is the Reynolds number (uL/ν), and Sc is the Schmidt number (ν/ D_{O_2}); u is the gas velocity and ν is the kinematic viscosity of the gas. Taking the viscosity of the gas to be $\nu = 2.3\times10^{-4} m^2/s$ (Turkdogan, 1980), the required Reynolds number was calculated to be 41.7, yielding a required gas velocity of 0.10m/s, or a gas flow rate of $8.3\times10^{-5} Nm^3/s$. This means that the required flow rates of nitrogen, carbon dioxide and oxygen are respectively 3.59Ndm^3/min, 0.4Ndm^3/min, and 0.15Ndm^3/min. After calibration and correction of the rotameters for gas density, the actual flow rates of nitrogen, carbon dioxide and oxygen that were used were respectively 3.91Ndm^3/min, 0.44 Ndm^3/min, and 0.16 Ndm^3/min (appendix 3).

3.2.2. Furnace set-up

The experiments were carried out in a vertical tubular furnace consisting of a pure (99.8% purity) mullite process tube with an inside diameter of 7.6 cm allowing samples of 5 cm width and 10 cm length to be oxidized. A schematic representation of the furnace assembly is shown in figure 11.

The maximum temperature that could reliably be reached in the available laboratory furnace without drastically reducing the life of the elements was 1400 ^{0}C. The furnace temperature was controlled by a Eurotherm 902P controller / programmer using a thermocouple that was positioned next to the furnace tube, close to the hot zone.

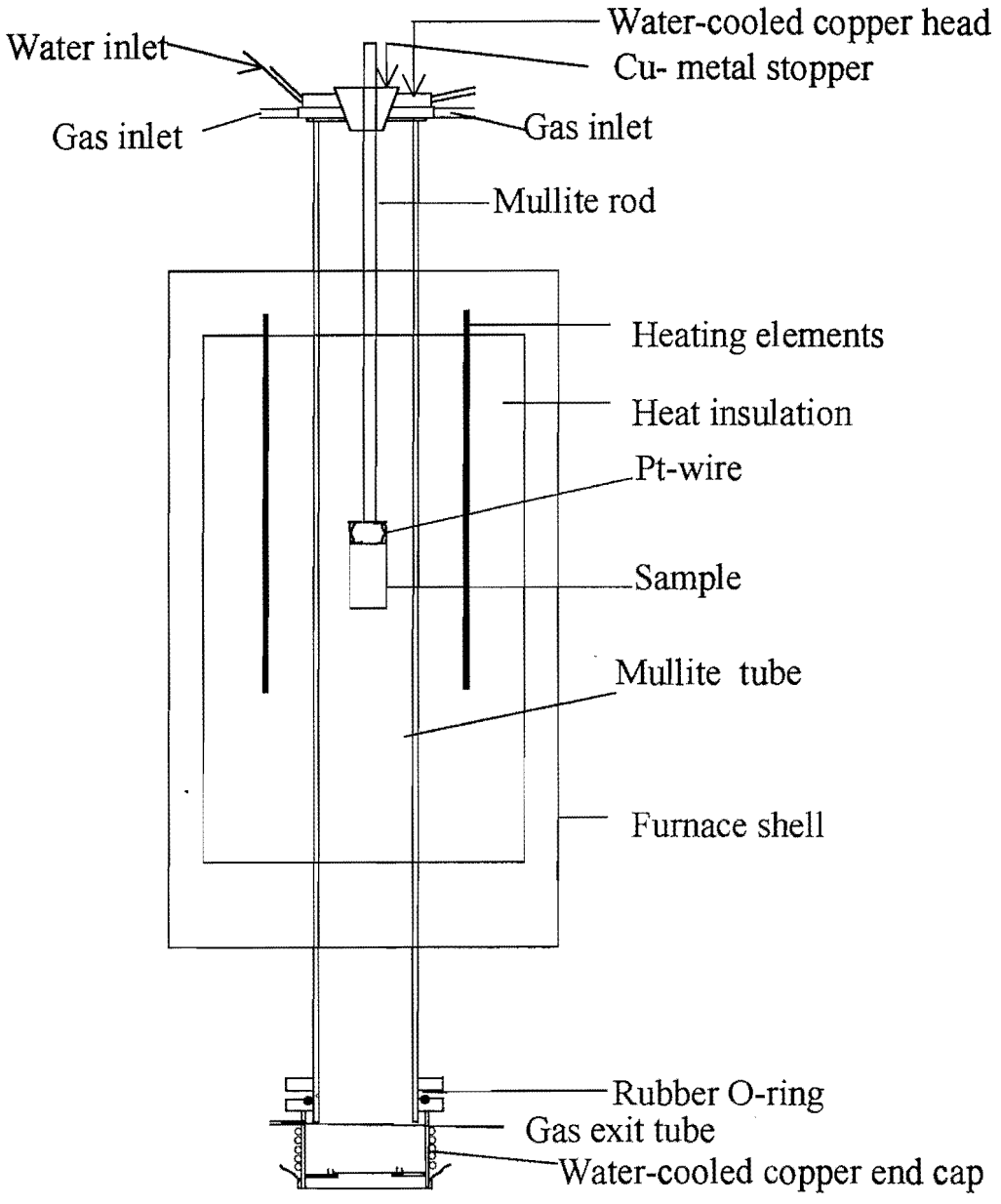

Figure 11 : Schematic representation of furnace assembly

The exact position of the hot zone in the furnace was measured by placing a hand-held K-type (Ni-Cr) thermocouple at various depths into the furnace tube. The

temperature profile as a function of position at a programmed temperature of 1250 ^{0}C is shown in figure 12. The reference point from which the depth was measured was the furnace top.

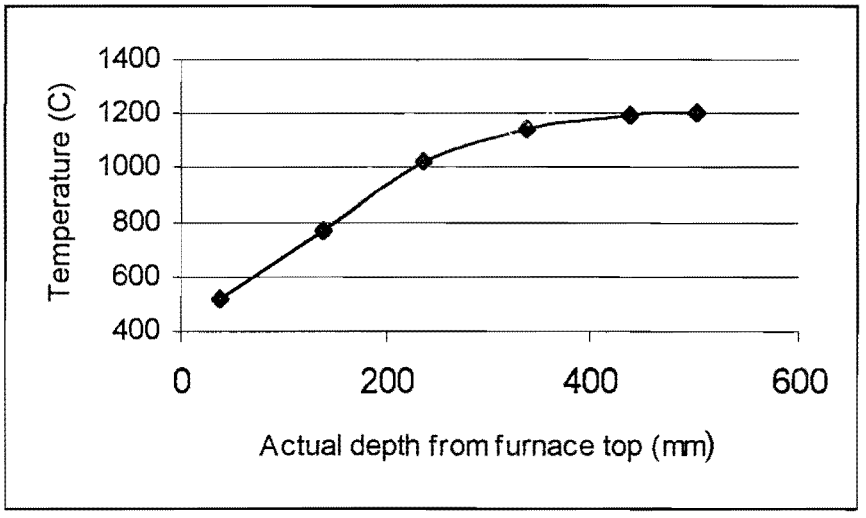

Figure 12 : Temperature profile as a function of position. (Depth measured from top of furnace. Programmed furnace temperature: 1250 ^{0}C. The average measured temperature in the hot zone was approximately 1200 ^{0}C.

The average temperature of the hot zone measured with the hand-held thermocouple was within 40 ^{0}C of that indicated by the furnace controller as shown in figure 13 below. This correlation was used to program the furnace temperature accurately.

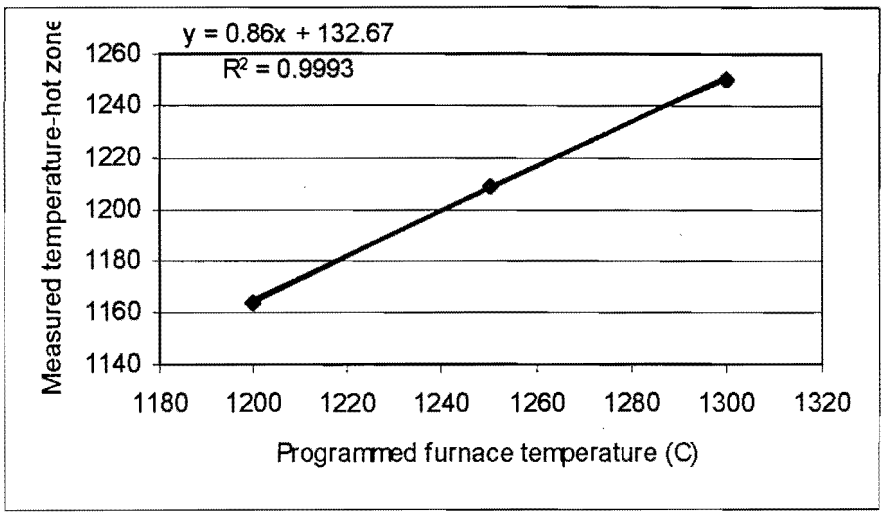

Figure 13 : Measured temperature in hot zone versus programmed furnace temperature at a depth of 503 mm below furnace top

The mullite furnace tube (90 mm O.D. x 76 mm I.D. x 1500 mm length) was fitted with water-cooled copper heads at both ends. The bottom fitting extended below the mullite tube and was sealed with an O-ring lubricated with high temperature vacuum grease. The upper end cap was sealed to the open flat end of the tube, sealing into a rubber gasket between the tube and the fitting. A steel bracket attached to the furnace tube exerted pressure on the gasket. Within the furnace, the sample was suspended from a mullite rod (8 mm I.D. and 1000 mm length) by means of platinum wire.

PVC - braided tubing was used for connecting the cooling water inlet and outlet to the furnace. Quick-connect couplings were used to ensure that the cooling water tubes could easily be removed from the copper-end cap before descaling of the sample.

3.3. Experimental set-up (Descaling)

At the end of the scaling period, the sample was removed from the furnace and subjected to mechanical descaling whilst hot. Literature observations indicated that the action of hydraulic descalers was largely mechanical (section 2). This meant that a mechanical means of descaling at temperature should yield an adequate simulation of in-plant hydraulic descaling. Thus, the mechanical descaling method of Tuck and Barlow (1972) was used, namely transferring the sample from the furnace to a bending rig. The rig used for this purpose is illustrated in Figure 14. As indicated the hot sample is placed on a U-shaped tool steel anvil, and then bent by a tool steel punch pressing on the center of the sample. The total time from opening of the furnace to deformation of the sample is about 30 seconds. The punch is driven by a pneumatic cylinder, which can give a maximum force of 10 kN (the calculation is shown below). The vertical displacement of the hammer is controlled by means of limit switches to ensure that the amount of deformation is the same in each case (to yield the same radius of curvature). The force required to deform the specimen was estimated from the expression for fully plastic bending of a beam (Hosford, *et al,* 1983):

$$F = \frac{bd^2\sigma}{L} \tag{3}$$

Where b, d and L are the sample width, thickness, and length respectively, and σ is the yield stress. Taking σ =50 MPa (Metals Handbook, 1980), b= 0.05m, d= 0.01m and L= 0.1m, the required force is calculated to be 2.5 kN, which is well within the capability of the available pneumatic cylinder, using compressed air available in the laboratory.

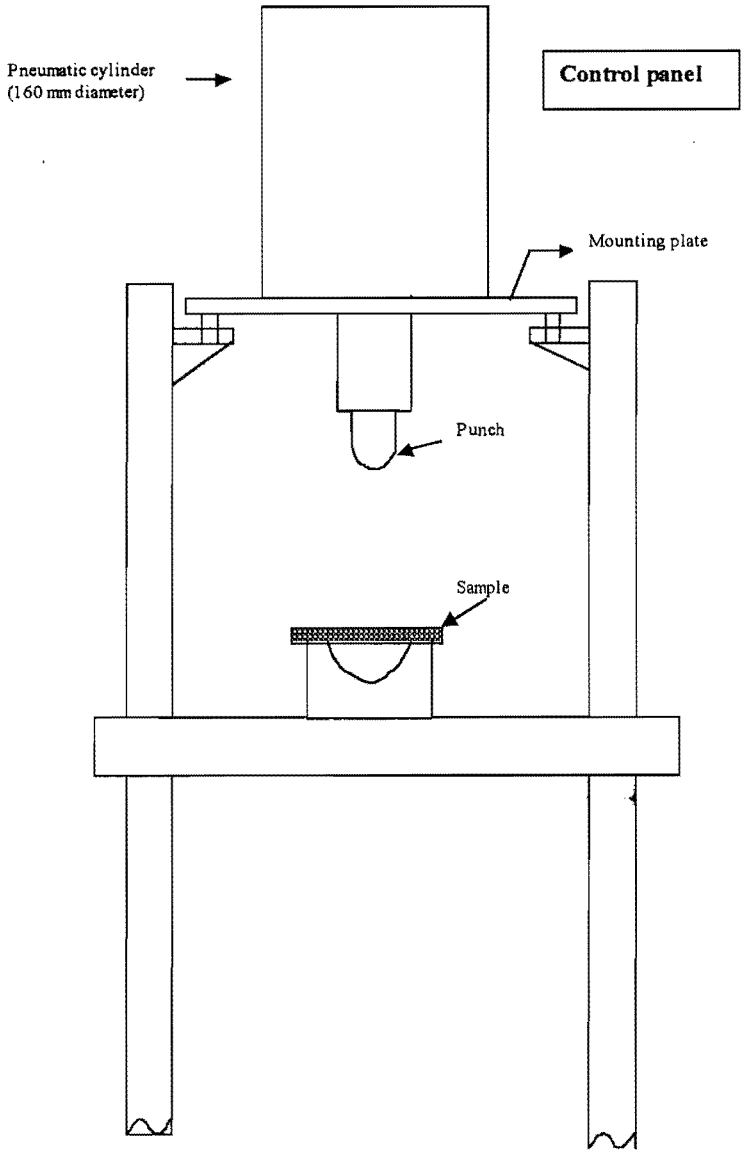

Figure 14 : Schematic representation of bending rig, to yield mechanical descaling

The validity of this method was assessed by testing whether it yielded the same descalability ranking as that observed in industry (e.g. comparing 11.5% chromium steel and type 304, and different amounts of excess oxygen.)

Figure 15 gives a closer view of the punch and anvil combination used to give mechanical descaling. The dot-dash lines show the position of the sample.

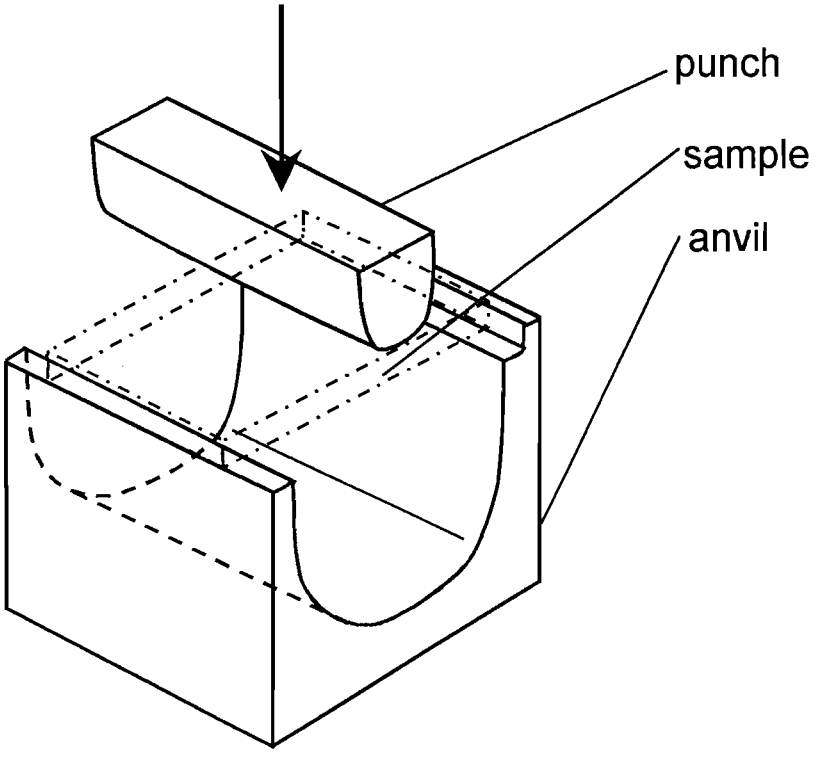

Figure 15 : Punch-and-anvil combination used to give mechanical descaling

Transfer of the samples from the furnace to the descaling station had to be performed in a standardized way, since cooling of the surface before descaling is detrimental to scale removal (Sheppard, and Steen, 1970). The interfacial roughness and the amount of residual scale were assessed by examining sample cross-sections by scanning electron microscopy (SEM). The calculations are shown in detail in appendix 6.

3.4. Experimental procedure

3.4.1. Sample size and preparation

Given the expected strong effect of steel compositions (nominal composition and impurity content) different grades of steel were used to test these effects. Since the 11.5% chromium stainless steel is said to behave very differently from type 304, these two stainless steels were considered in this study. Thus the steels used were samples of type 412 and 304 stainless steel. Samples from different heats of the two steel grades were used in this work. However, these were similar in chemistry and microstructure, and average chemical compositions are given in the table below.

Element	Grade	
	412	304
C	0.021	0.044
S	0.0024	0.0033
P	0.026	0.022
Mn	0.485	1.305
Si	0.72	0.40
V	0.08	0.12
Cu	0.09	0.09
Co	0.02	0.03
Ti	0.034	0.010
Mo	0.02	0.14
Cr	11.62	18.16
Ni	0.34	8.09
Al	0.002	0.004
Nb	0.002	0.003
B	0.003	0.001
N	0.0213	0.050
O	0.0037	0.0080

Figure 16 : Table of chemical compositions (mass percentages) of samples

The samples were cut to size from hot-rolled plate using a band saw as well as a fixed abrasive disc cutter. The samples were typically around 100 mm x 50 mm x 10

mm large. 3 mm holes – through which Pt-wire was passed to hang the sample - were drilled close to one of the shorter sides of the sample. These comparatively large sample dimensions were required to minimize the relative effects of scale growth stresses at the specimen edges and corners; the principle is to have the width and length large compared with the scale thickness (which could approach 5 mm for long reheating times). If smaller specimens were used, the growth stresses (which inevitably arise during oxide growth) could detach the scale from the steel surface, so altering the scale growth rate and adhesion.

The stainless steel samples used here had been pickled clean in the plant, and were hence only degreased (with acetone) before scaling.

3.4.2. Experimental run

As mentioned earlier, the gas composition was chosen to correspond to the combustion products of methane with air, with 3% or 4% excess oxygen. The total gas flow rate was 4 Ndm^3/min. To ensure that the gas composition was correct the gas mixture was analyzed regularly using a Gaslab 300 gas analyzer (appendix 4). Thus the gas composition was obtained by mixing the nitrogen, oxygen and carbon dioxide in a glass bead mixer and saturating this with water vapour by passing the mixture through water kept near its boiling point (as discussed in paragraph 4.2.1.1). The mixture was then fed into the furnace.

Some preliminary experiments were done to ensure that the correct amount of water vapour entered the furnace. This was done by passing the exit gas at the bottom of the furnace through a drierite column that had been pre-weighed. After the experiment the drierite column was then weighed again. The difference between the two weights, gave the amount of water that had been absorbed by the drierite. This value was then compared to the theoretically calculated mass of water that was

expected to be in the gas mixture. In all of the experiments the values were quite similar (appendix 4).

At the end of the scaling period, the sample was removed from the furnace and subjected to mechanical descaling whilst hot. Following mechanical descaling and cooling of the sample (in air for stainless steel, with the sample placed on a stainless steel plate which acts as a heat sink), samples were cut from the region of tensile deformation and from the undeformed region of the sample (as illustrated in figure 17), using a band saw.

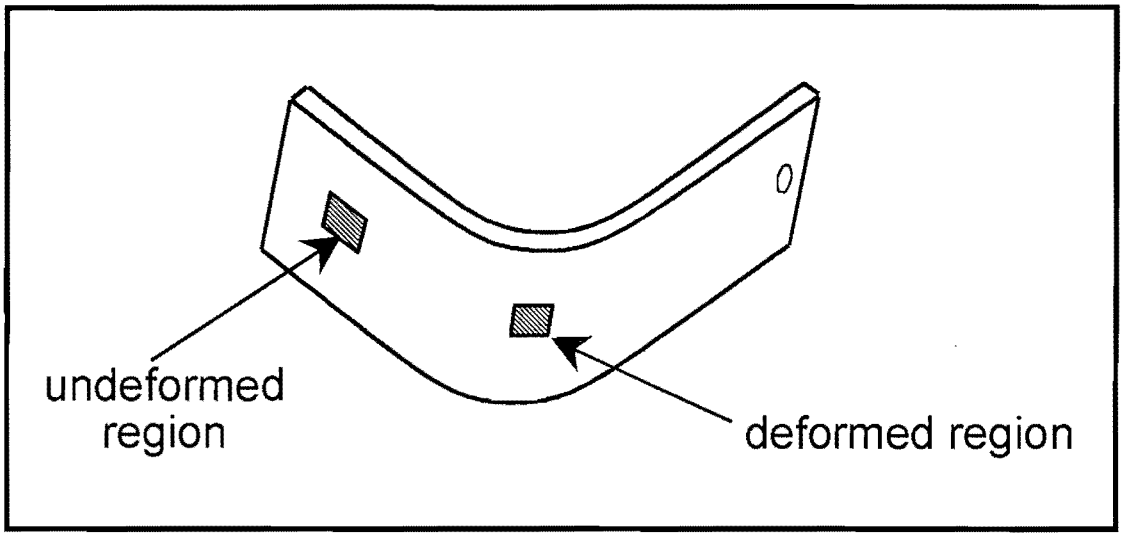

Figure 17 : Location of samples to assess the degree of descaling, within the reheated sample which had been descaled by bending

The samples were mounted in metallographic resin, machined away and then polished to allow a cross-section near the center of the sample to be examined (so avoiding possible edge effects). The samples were examined in a scanning electron microscope (recording the secondary electron image). Backscatter electron imaging (at an acceleration voltage of 15 kV) was used to show the nature of the scale-steel interface. Energy-dispersive X-ray analysis (EDX) was used for point analyses of the

various phases. The average thickness of scale remaining on the descaled surfaces was found by means of image analysis (of the SEM images).

The basic matrix of experiments done is shown in the table below.

Temperature (^{0}C)	% O_2	Reheating time(hr)
1280	3	1.5
1250	4	3
		6

Figure 18 : Experimental matrix for type 304 stainless steels

For the type 304 stainless steels some preliminary experiments were done at a reheating temperature of 1245 ^{0}C. These experiments served to test whether the experimental configuration as assembled, could be used successfully to simulate scale growth and descaling. The type 304 steel was used in this initial assessment, both because of ready availability of suitable plate material and because of the apparent contradiction between the observation of substantial steel-scale entanglement and the plant observation of good descalability (which hence made this a good test for the validity of the laboratory test).

In the next batch of experiments done, all the samples were reheated isothermally at 1280 ^{0}C and 1250 ^{0}C, with free oxygen contents in the gas stream of 3 % and 4 % oxygen respectively, and reheating times ranging from 1.5 hours to 6 hours. The reheating temperature of 1250 ^{0}C is similar to the actual reheating temperature of type 304 stainless steels in industry. A few preliminary experiments were also done at reheating temperatures of 1230 ^{0}C and 1260 ^{0}C.

For the type 412 stainless steels, all the samples were also reheated isothermally at 1280 ^{0}C as well as 1210 ^{0}C, with free oxygen contents in the gas stream of 3 % and 4 % oxygen respectively, and reheating times ranging from 1.5 hours to 6 hours. The reheating temperature of 1210 ^{0}C is similar to the actual reheating temperature of type 412 stainless steels in industry.

Temperature (^{0}C)	% O_2	Reheating time(hr)
1280	3	1.5
1210	4	3
		6

Figure 19 : Experimental matrix for type 412 stainless steels

The temperature during reheating was generally monitored and controlled by means of the furnace thermocouple. However in two runs an additional (R-type) thermocouple was spot-welded to the sample surface to ensure more careful measurement of the sample temperature in the furnace. Since the gas which is introduced into the furnace is not preheated, this will tend to quench the sample slightly, whereas the exothermic nature of the scaling reaction tends to conversely heat the sample surface to a slightly higher temperature than the furnace hot zone.

The furnace temperature used for these experiments was 1280 ^{0}C, in an atmosphere with 3% excess oxygen. The samples were reheated for approximately 3.5 hours. The recorded sample temperatures were plotted in the graphs below.

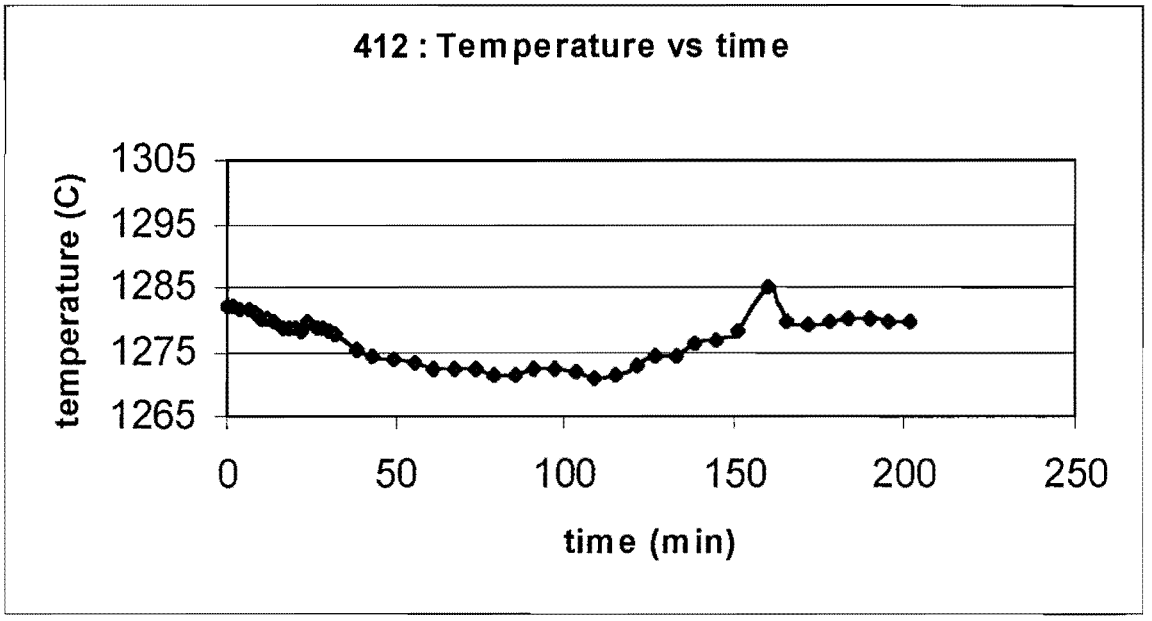

Figure 20 : Type 412-sample temperature as a function of time

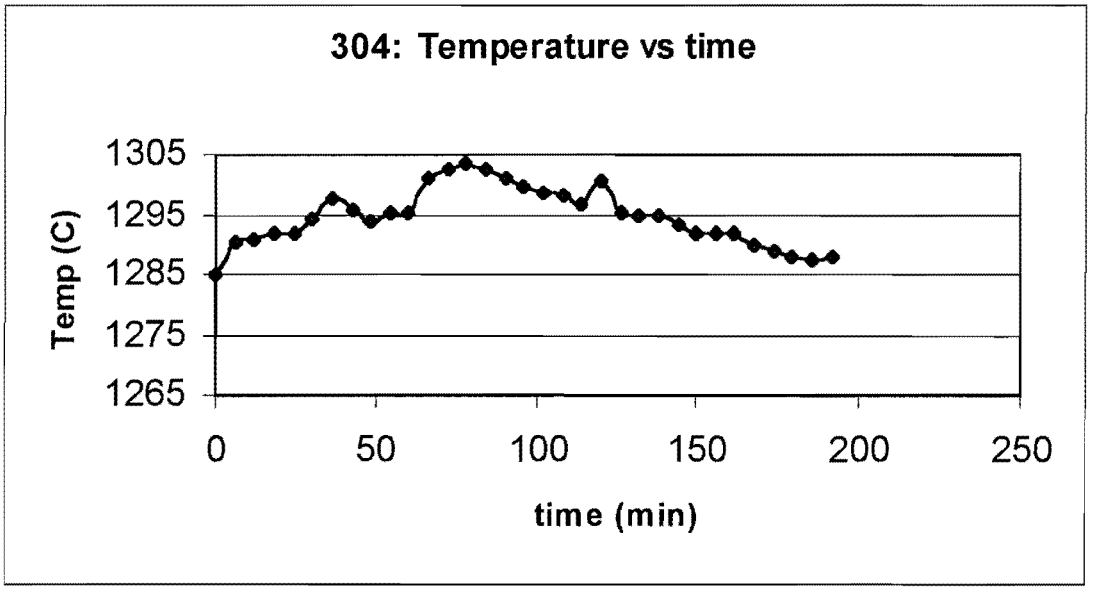

Figure 21 : Type 304-sample temperature as a function of time

It was found that the sample temperature was generally within 10 ^{0}C of the furnace temperature (1280 ^{0}C). Thus the samples did not heat significantly above the furnace temperature. Although some heating was expected from the exothermic nature of the oxidation reactions, it was found that this was not significant for these samples.

4. Results

4.1. Stainless steel type 412

The scale had a complex structure. The outer layer was iron oxide containing little or no chromium. The inner layer of scale largely consisted of an iron-chromium spinel, but with more phases present close to the interface with the steel. Closer examination of the metal-scale interface revealed severe entanglement at the interface.

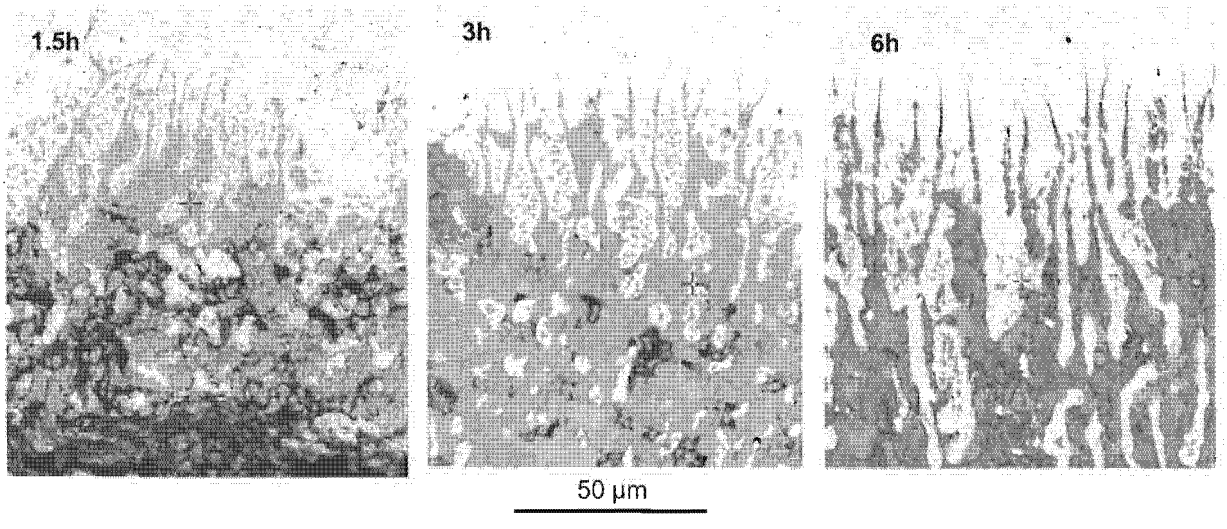

Figure 22 : Scanning electron micrographs of the scale-steel interface of type 412 samples held at 1210 ^{0}C with 4% excess O_2 for different holding times (as indicated on the micrographs).

The metal is at the top of the images in figure 22 and the scale at the bottom. The width of the entangled zone appears to increase as the holding time increases and the tendrils of metal become much coarser. These coarser tendrils perhaps anchor the scale more strongly to the steel, with the resulting poorer descaling. Given that interfacial roughening arises in this steel but is not reported in literature for (pure)

binary iron-chromium alloys, the residual elements must play a role. Closer examination of the entangled region reveals an effect of silicon. As the table of steel compositions (figure 16) indicates, the steel contains 0.72% Si. This silicon (once oxidised) accumulates at the scale-metal interface and forms a fayalite melt.

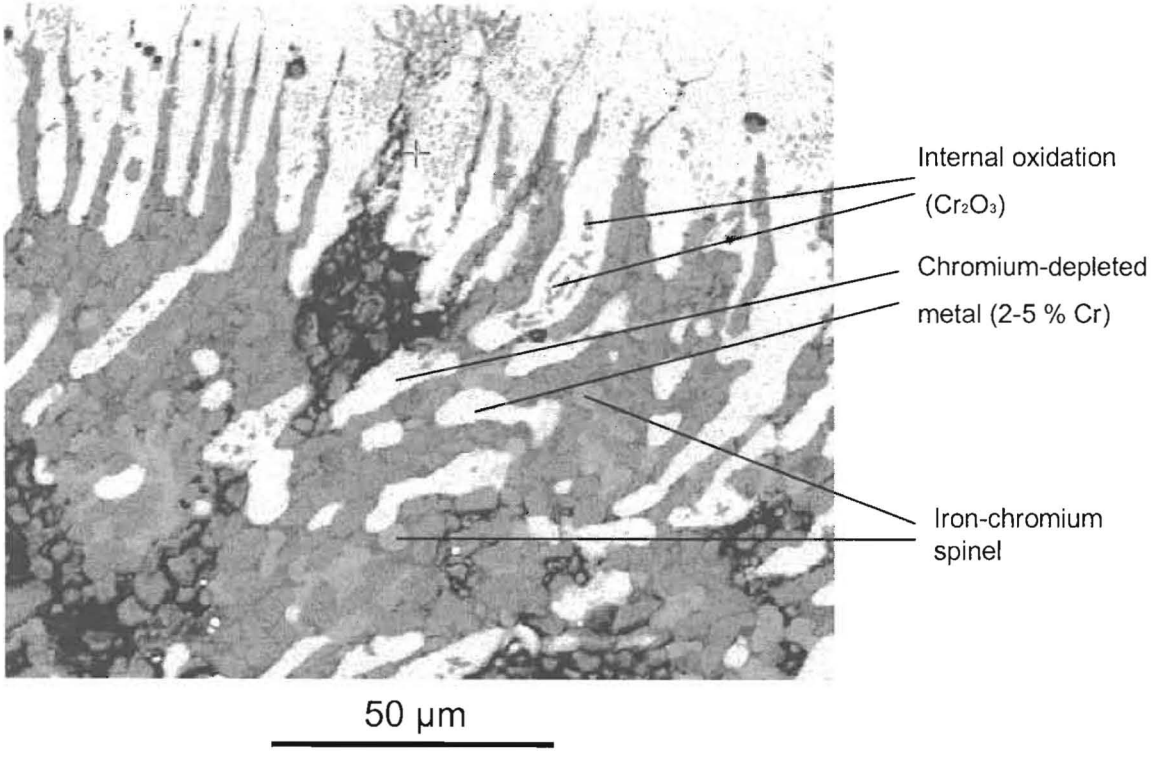

Figure 23 : Detail of the structure in the entangled region, showing internal oxidation

The metal at the interface is chromium-depleted as shown in figure 23. The metal contains approximately 2-5 % chromium as indicated by the point analyses in appendix 5. This low chromium content is the result of precipitation – by internal oxidation – of Cr_2O_3 within the metal. Upon oxidation of the remaining iron to iron oxide the Cr_2O_3 is converted to the spinel scale, and some iron is transported through the spinel scale to precipitate as the iron oxide scale at the outer surface. This sequence of phases is as expected from the iron-chromium-oxygen phase diagram (Laheij et al, 1980).

4.1.1. Residual scale thickness

4.1.1.1 REHEATING TEMPERATURE : 1210 ^{0}C

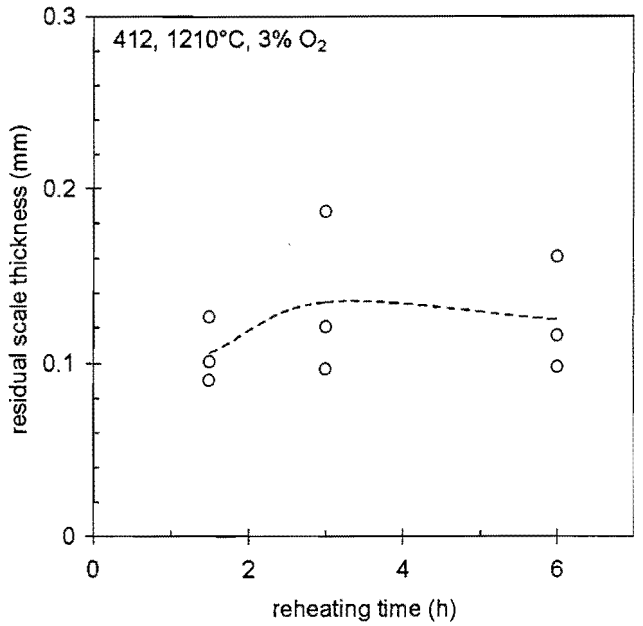

a)

Type 412, at 1210 ^{0}C with 3% O_2

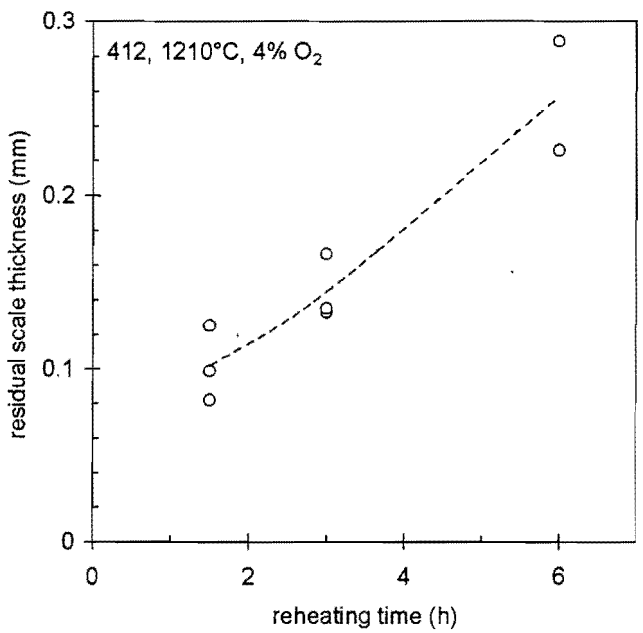

b)

Type 412, at 1210 ^{0}C with 4% O_2

Figure 24 : Measured residual scale thickness for type 412 samples, reheated at 1210 ^{0}C, for varying times and with 3% and 4% oxygen in the furnace atmosphere

The graphs on the previous page show the measured residual scale thicknesses, for type 412 samples that were reheated at 1210 ^{0}C, for varying reheating times and with 3% and 4% oxygen in the furnace atmosphere. The data points show measurements at three positions on each descaled surface and the broken line the average of these measurements. The results show that the 412 steel grade is quite sensitive to reheating time and excess oxygen, with increases in both elevating the amount of residual scale.

The following graphs below (figure 25) illustrate the way in which the width of the entangled region increases with longer reheating times and higher excess oxygen contents, for type 412 stainless steel. This is in line with the effect of such processing changes on the amount of residual scale (figure 24).

The micrographs in figure 22 differ from those in figure 25 (for 4% excess oxygen) because in figure 22 the micrographs were taken from the undescaled section of the sample (concave part of the deformed region in figure 17), whilst in figure 25 the micrographs were from the descaled section of the sample (convex part of the deformed region in figure 17).

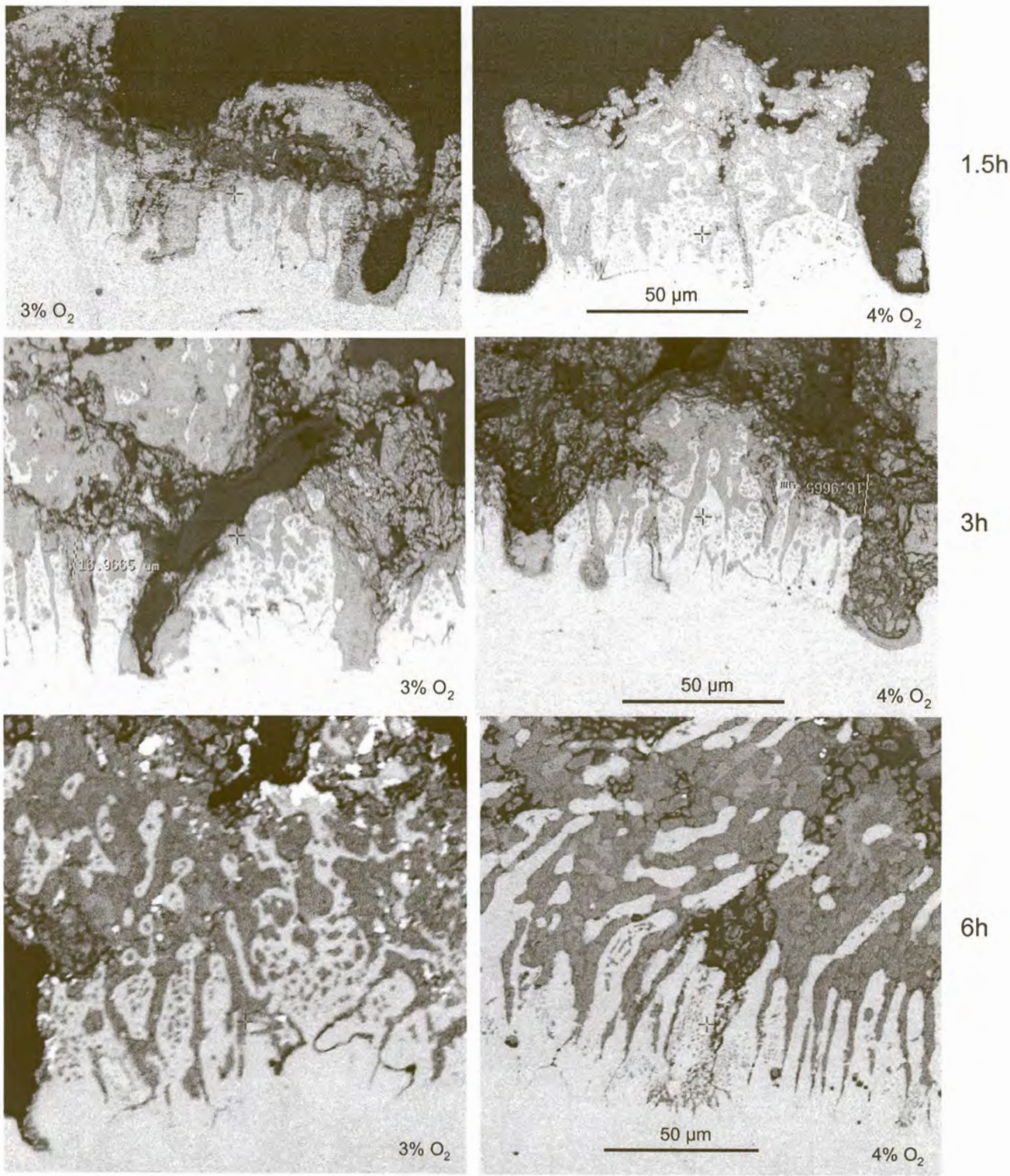

Figure 25 : Development of entanglement at the scale-steel interface, for type 412 steel at a reheating temperature of 1210 ^{0}C (scanning electron micrographs)

In all of the images, the scale is towards the upper part of the image and the steel substrate towards the bottom. All the samples were mechanically descaled. Each pair of images is for the same reheating time, but for two different levels of excess oxygen.

The direct link between the width of the entangled region and the residual scale thickness is illustrated by figure 26, which shows a lower magnification image of a sample, which had been reheated for 6 hours and then mechanically descaled. Evidently fracture of the scale occurred at the edge of the entangled region, leaving the entire entangled region attached to the substrate. The strong effect of reheating conditions on the amount of residual scale has clear implications for the need to control excess oxygen closely in industrial operations.

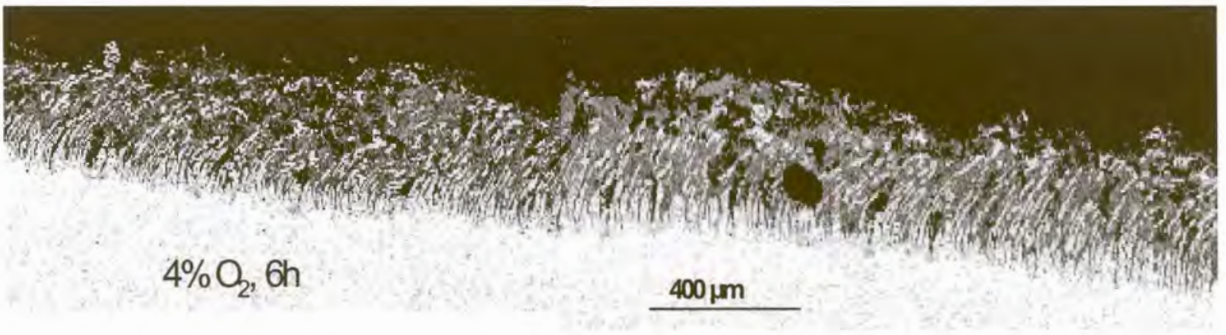

Figure 26 : Montage of descaled surface of type 412 sample (reheated at 1210 ^{0}C), showing that the residual scale thickness corresponds to the full thickness of the entangled region

4.1.1.2 REHEATING TEMPERATURE : 1280 ^{O}C

The figures below are for the same conditions as in the previous section however; the reheating temperature is 1280 ^{0}C.

Figure 27 also shows the measured residual scale thicknesses, for type 412 samples. The results also illustrate the sensitivity of the 412 steel grade to reheating time and excess oxygen. However the effect is not similar to the reheating temperature of 1210 ^{0}C and the fact that the residual scale thickness seems to decrease for longer reheating times in figure 27, is quite odd. In both cases of reheating time and excess oxygen at 1280 ^{0}C however, there is still more than 0.1mm scale remaining after 6 hours. The way in which the width of the entangled region develops with longer reheating times and higher excess oxygen contents, for type 412 stainless steel at this higher reheating temperature, is shown in figure 28. In all of the images, the scale is towards the upper part of the image and the steel substrate towards the bottom.

a)

Type 412, at 1280 ^{0}C with 3% O_2

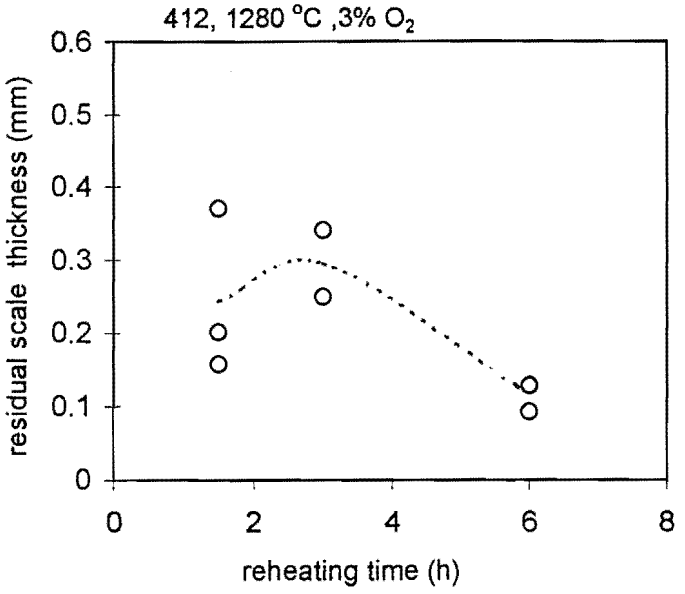

b)

Type 412, at 1280 ^{0}C with 4% O_2

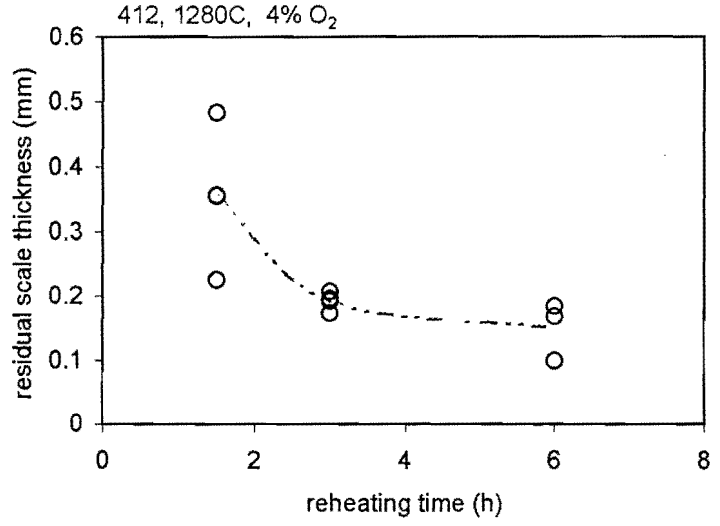

Figure 27 : Measured residual scale thickness for type 412 samples, reheated at 1280 ^{0}C, for varying times and with 3% and 4% oxygen in the furnace atmosphere

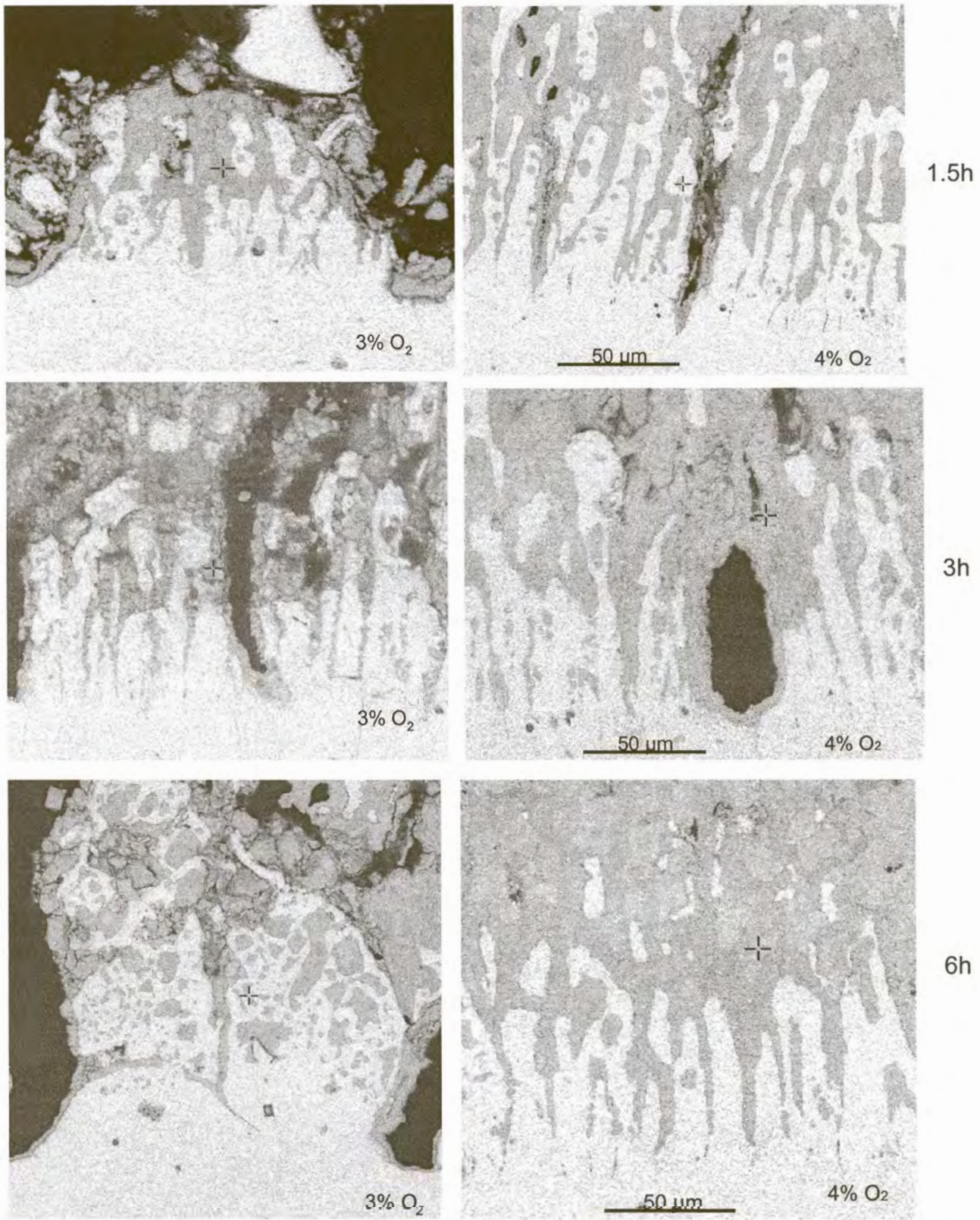

Figure 28 : Development of entanglement at the scale-steel interface, for type 412 steel at a reheating temperature of 1280 ° C (scanning electron micrographs)

Figure 29 shows a lower magnification image of a sample, which had been reheated for 1.5 hours and then mechanically descaled. Fracture of the scale occurred at the edge of the entangled region, leaving the entire entangled region, attached to the substrate. The direct link between the width of the entangled region and the residual scale thickness is illustrated.

Figure 29 : Montage of descaled surface of type 412 sample (reheated at 1280 ^{0}C)

4.2. Stainless steel type 304

Tendrils of unoxidized metal were detected in the scale on the type 304 samples as shown in figure 30. The scale is at the top of the images and the metal at the bottom. The composition (mass percentages) of these tendrils was 4-11% chromium and 12-15% nickel (balance iron) close to the steel-scale interface, with the chromium content decreasing to 3 –4% as you move away from the interface into the entangled scale (appendix 5). Thus at the interface, the composition of the metal tendrils is a chromium-depleted form of the original composition (18.16 % Cr and 8.09 % Ni – as given in figure 16) and nickel enrichment is found in the tendrils which are present in the outer layers of the scale.

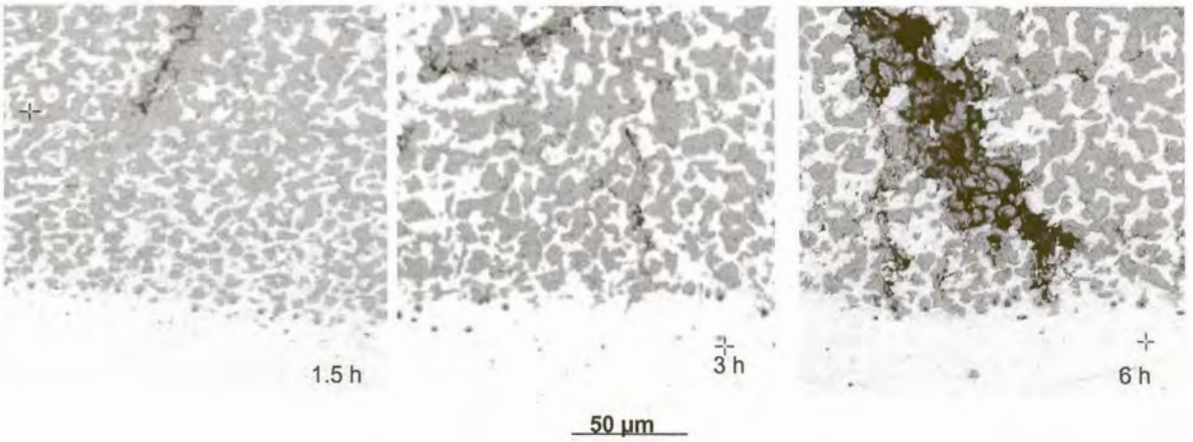

Figure 30 : Scanning electron micrographs of the scale-steel interface region of type 304 samples held at 1280 ^{0}C and 4% excess O_2 for different times (as indicated on the micrographs).

4.2.1. Residual scale thickness

4.2.1.1 REHEATING TEMPERATURE: 1250 ^{O}C

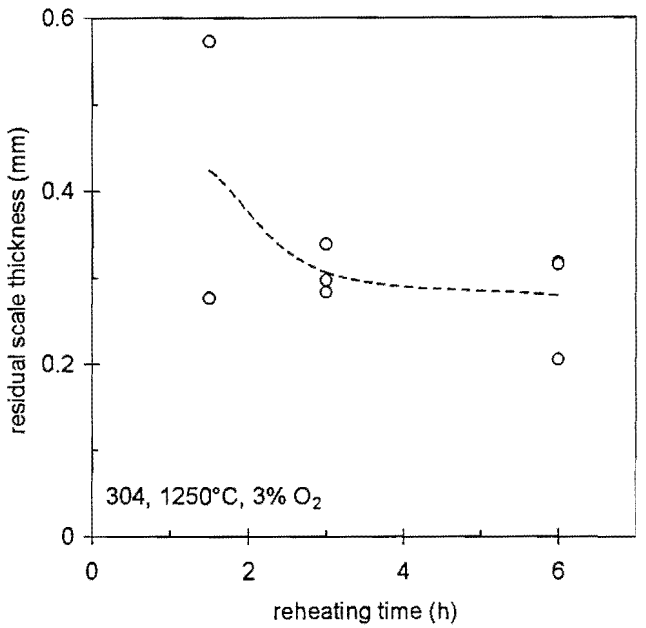

c)

Type 304, at 1250 ^{0}C, with 3% O_2

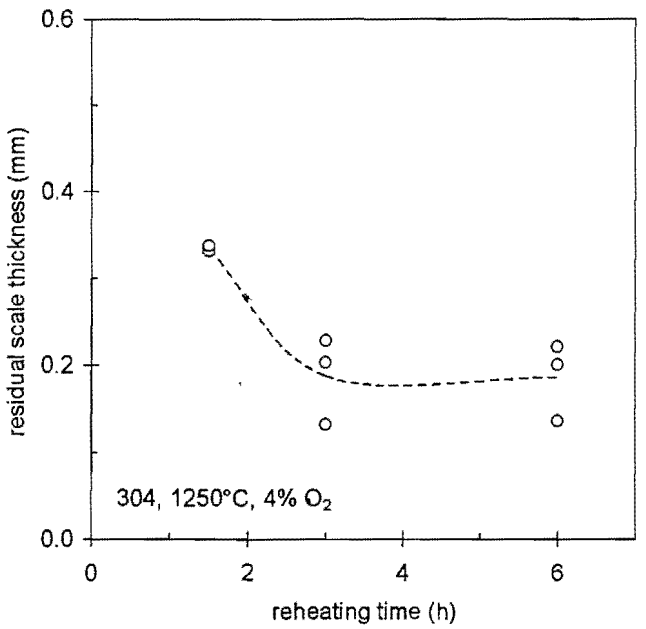

d)

Type 304, at 1250 ^{0}C, with 4% O_2

Figure 31 : Measured residual scale thickness for type 304 samples, reheated at 1250 ^{0}C, for varying times and with 3% and 4% oxygen in the furnace atmosphere

The graphs on the previous page (figure 31) show the measured residual scale thicknesses, for type 304 samples that were reheated at 1250 ^{0}C, for varying reheating times and with 3% and 4% oxygen in the furnace atmosphere. The data points show measurements at three positions on each descaled surface and the broken line the average of these measurements. The residual scale on the type 304 samples at this temperature, were not much affected by reheating conditions; if anything the scale somewhat decreased in thickness for higher excess oxygen and longer reheating. This difference is caused by the way in which the type 304 samples descaled. As figure 32 below illustrates, descaling arose by the formation of numerous cracks through the scale. In all of the images, the scale is towards the upper part of the image and the steel substrate towards the bottom. Each pair of images is for the same reheating time, but for two different levels of excess oxygen.

Closer examination revealed that these cracks followed areas of metal-free scale, as shown at higher magnification in figure 33. ("Metal-free scale" here indicates regions of the scale which consisted of oxide only, without any nickel-enriched metal tendrils). The metal-free chromite scale regions offer low-toughness fracture paths, and hence the extent of descaling is linked directly to the prevalence of these fracture paths in the strongly entangled scale. No descaling was observed between the substrate and the scale where such chromite paths were absent. The chromite layers apparently form by internal oxidation (as indicated by the chromite layer extending into the substrate in the 1.5 hour sample of figure 33), with internal oxidation somewhat more prevalent on the austenite grain boundaries. Hence the location of the chromite layers in the scale (the fracture paths during subsequent descaling) depends on the austenite grain structure.

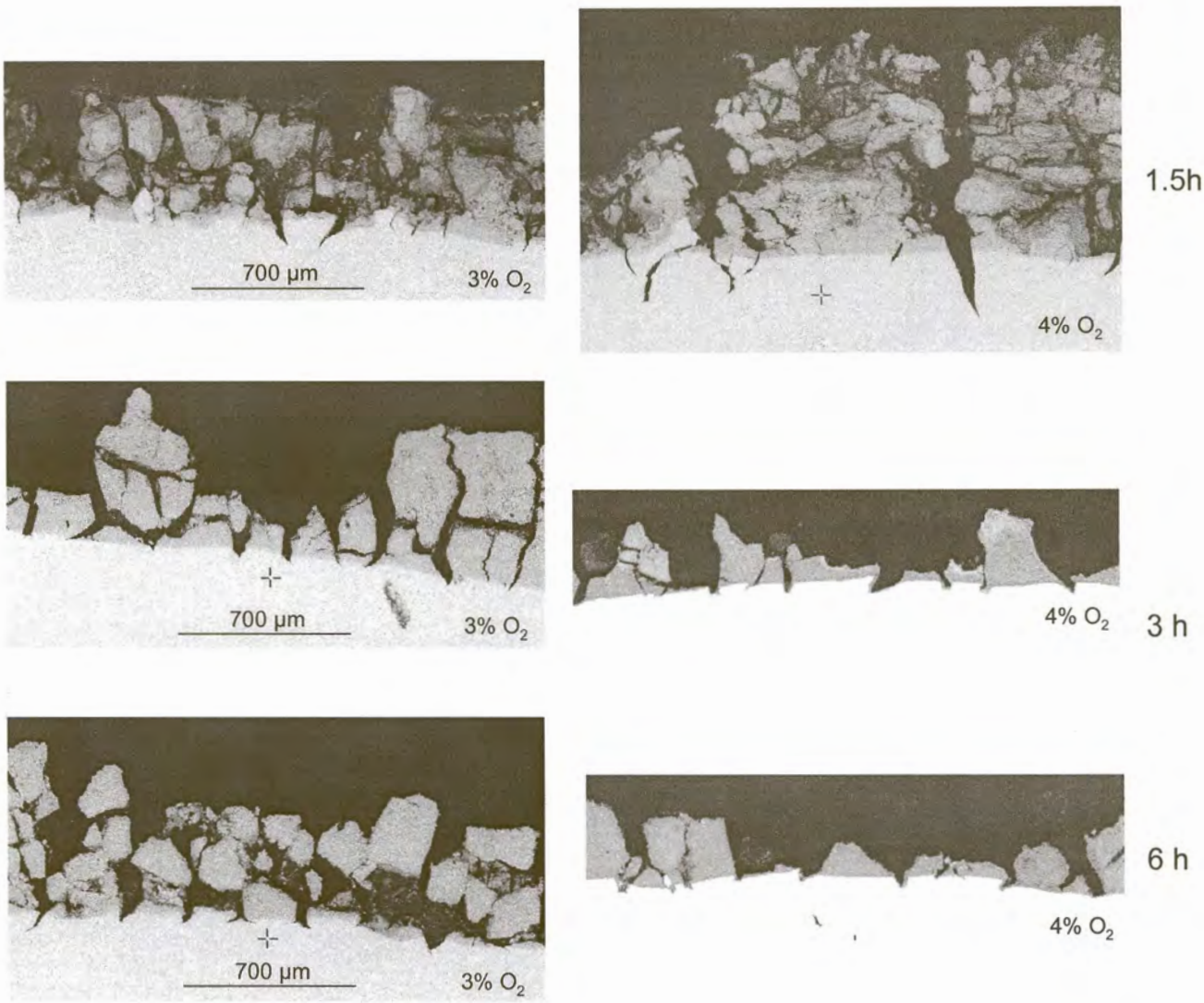

Figure 32 : Change in appearance of the residual scale, for type 304 stainless steel, after reheating at 1250 ^{0}C and mechanical descaling (scanning electron micrographs)

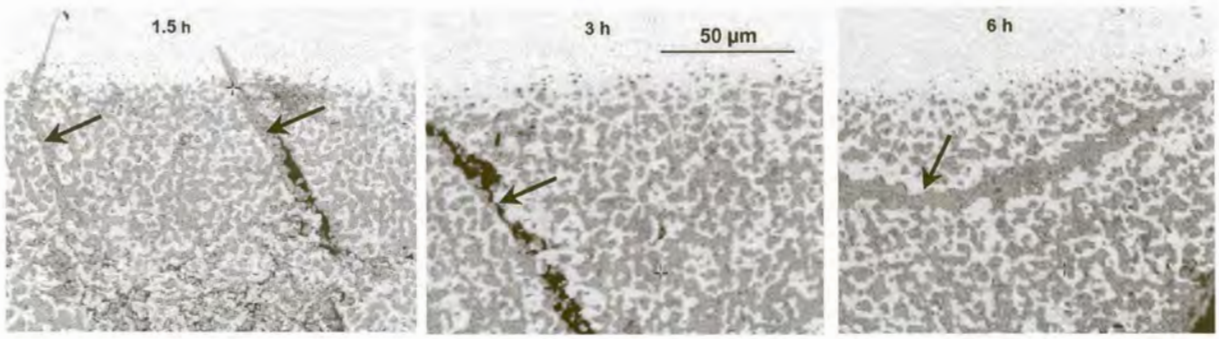

Figure 33 : Structure of scale close to scale-steel interface, for type 304 stainless steel reheated at 1250 ^{0}C in an atmosphere with 4% excess oxygen. Planes of metal-free chromite (arrowed) are evident. (The unoxidised substrate is shown in the upper parts of the three images.)

The correspondence between the austenite grain structure and the fracture paths is confirmed in figure 34, which shows cross-sectioned samples that had been etched (using electrolytic oxalic acid etch) to reveal the austenite grain structure. Cracks in the residual scale can be seen to correspond to grain boundaries in the underlying microstructure. This is also evident in figure 35 as well as appendix 7.

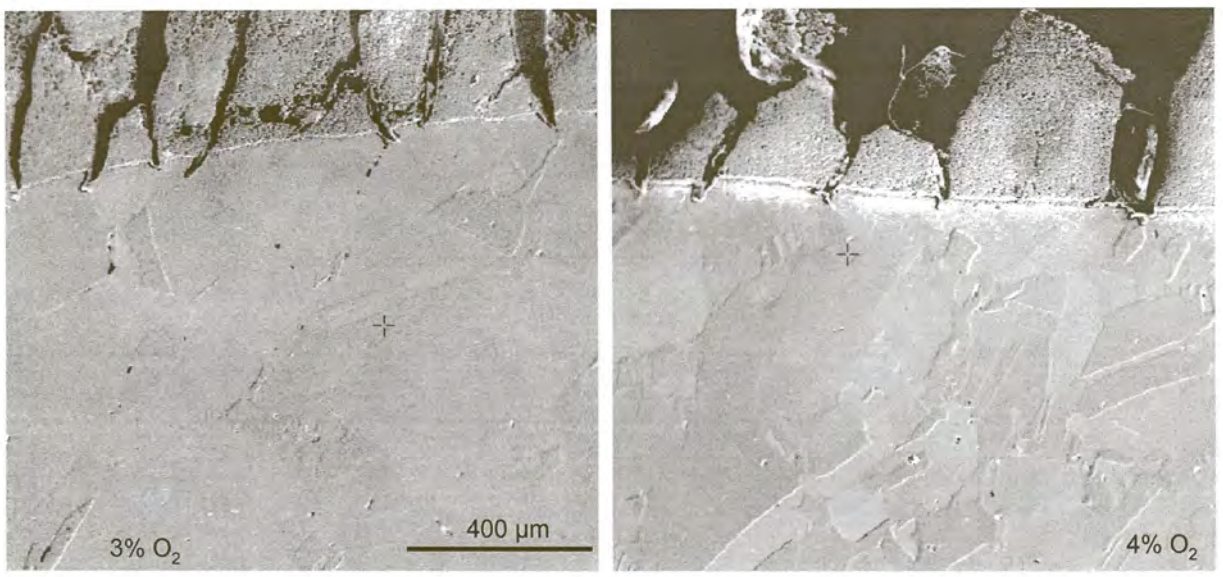

Figure 34 : Etched cross-sections of type 304 samples reheated at 1250 ^{0}C.

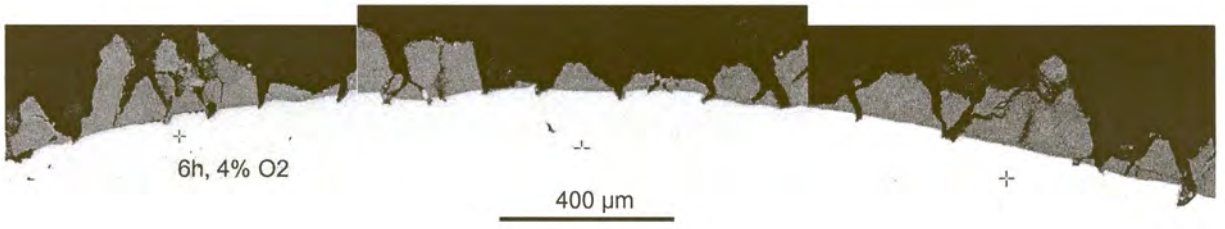

Figure 35 : Montage of descaled surface of type 304 sample (reheated at 1250 ^{0}C),

4.2.1.2 REHEATING TEMPERATURE : 1280 ^{O}C

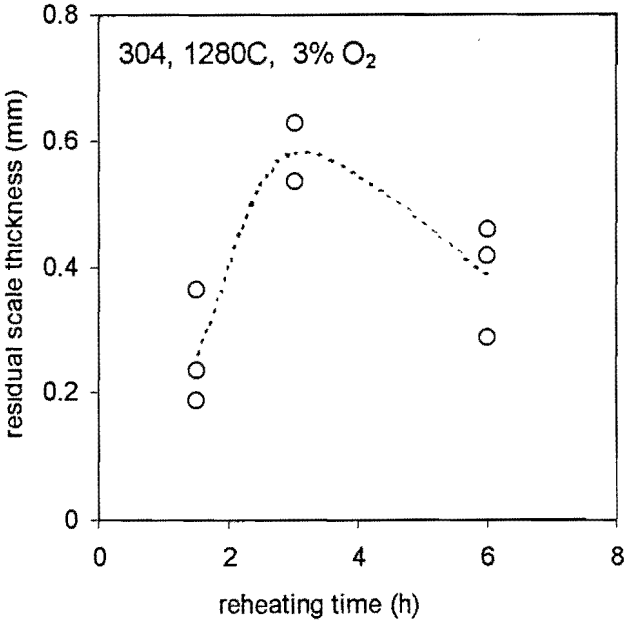

c)

Type 304, at 1280 ^{0}C, with 3% O_2

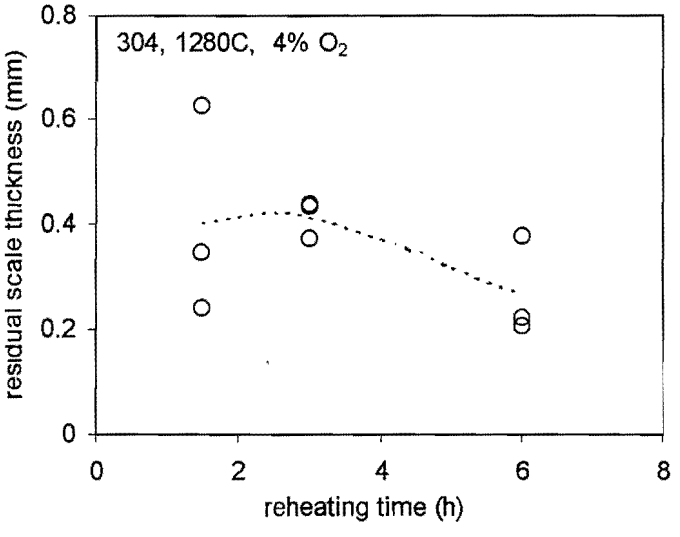

d)

Type 304, at 1280 ^{0}C, with 4% O_2

Figure 36 : Measured residual scale thickness for type 304 samples, reheated at 1280^{0}C, for varying times and with 3% and 4% oxygen in the furnace atmosphere

The graphs on the previous page (figure 36) show the measured residual scale thicknesses, for type 304 samples that were reheated at 1280 ^{0}C, for varying reheating times and with 3% and 4% oxygen in the furnace atmosphere. The residual scale somewhat decreased in thickness for higher excess oxygen and longer reheating. As was stated previously, this difference is caused by the way in which the type 304 samples descaled — by the formation of numerous cracks through the scale as is illustrated in figure 37 below.

On comparing the residual thicknesses at 1280 ^{0}C and at 1250 ^{0}C, it is evident that for both reheating temperatures, the residual scale again somewhat decreased in thickness for higher excess oxygen and longer reheating. However, slightly more residual scale is observed at the reheating temperature of 1280 ^{0}C (especially for 3% excess oxygen). As mentioned earlier, this can be explained by the way in which the samples descaled — by formation of cracks through the scale (or the lack of crack formation in this particular case, as seen on comparison of figures 32 and 37).

Etched cross-sections of samples, which were reheated at 1280 ^{0}C, are shown in figure 39. Cracks in the residual scale can be seen to correspond to grain boundaries in the underlying microstructure. The lack of cracks in this figure (resulting in the presence of slightly more residual scale at the reheating temperature of 1280 ^{0}C) is also evident on comparison with figure 34.

Small amounts of delta ferrite may serve to pin the austenite grain boundaries and so favour descaling – austenite crystals are produced during the transformation of primary delta ferrite crystals which are enriched with nickel and substantially depleted of chromium. Delta ferrite appears upon reheating at high temperatures, increasing in extent up to the melting point and from an Fe-Ni-Cr phase diagram, the formation of delta ferrite starts at a temperature of approximately 1250 ^{0}C (Folkhard, 1988).

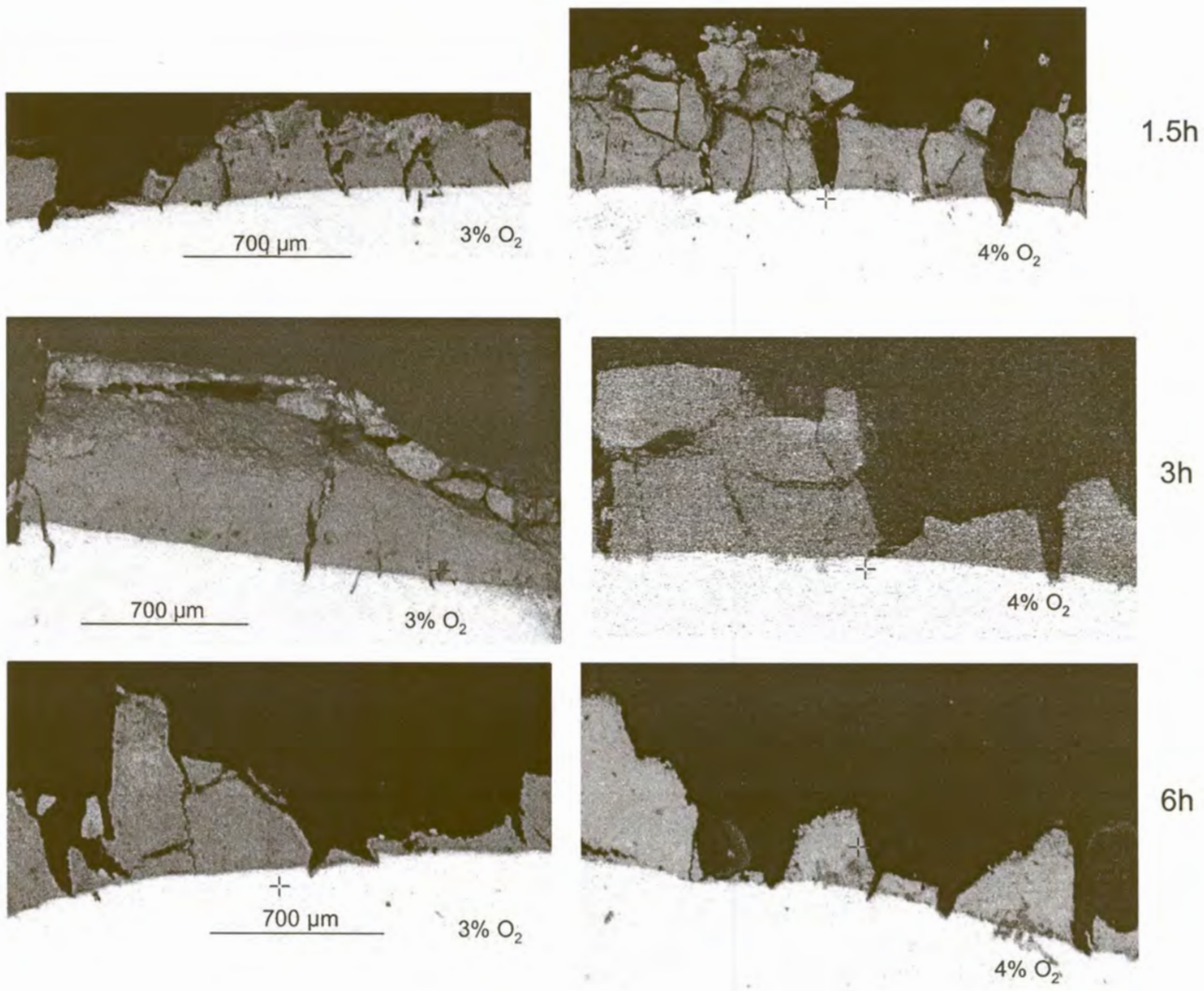

Figure 37 : Change in appearance of the residual scale, for type 304 stainless steel, after reheating at 1280 ^{0}C and mechanical descaling (scanning electron micrographs)

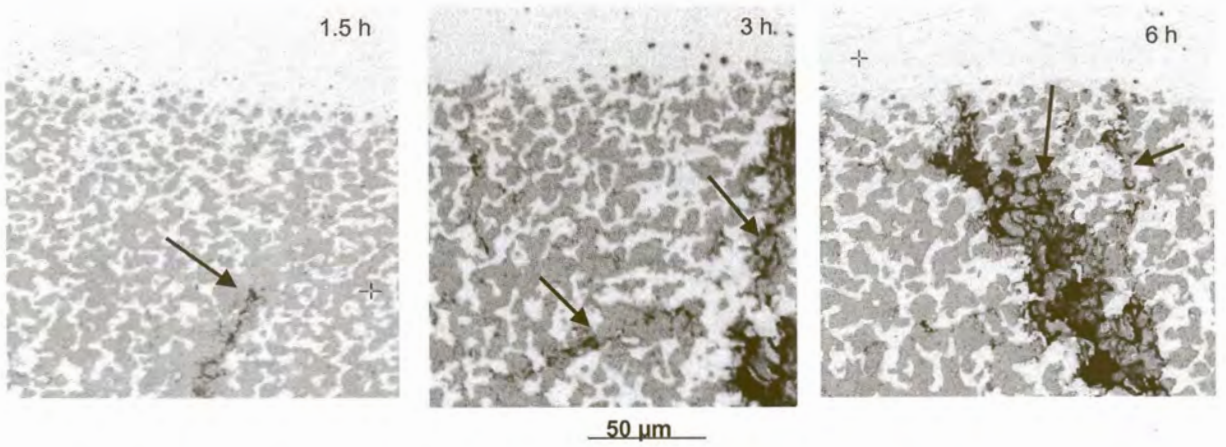

Figure 38 : Structure of scale close to scale-steel interface, for type 304 stainless steel reheated at 1280 ^{0}C in an atmosphere with 4% excess oxygen. Planes of metal-free chromite (arrowed) are evident. The unoxidised substrate is shown in the upper parts of the three images.

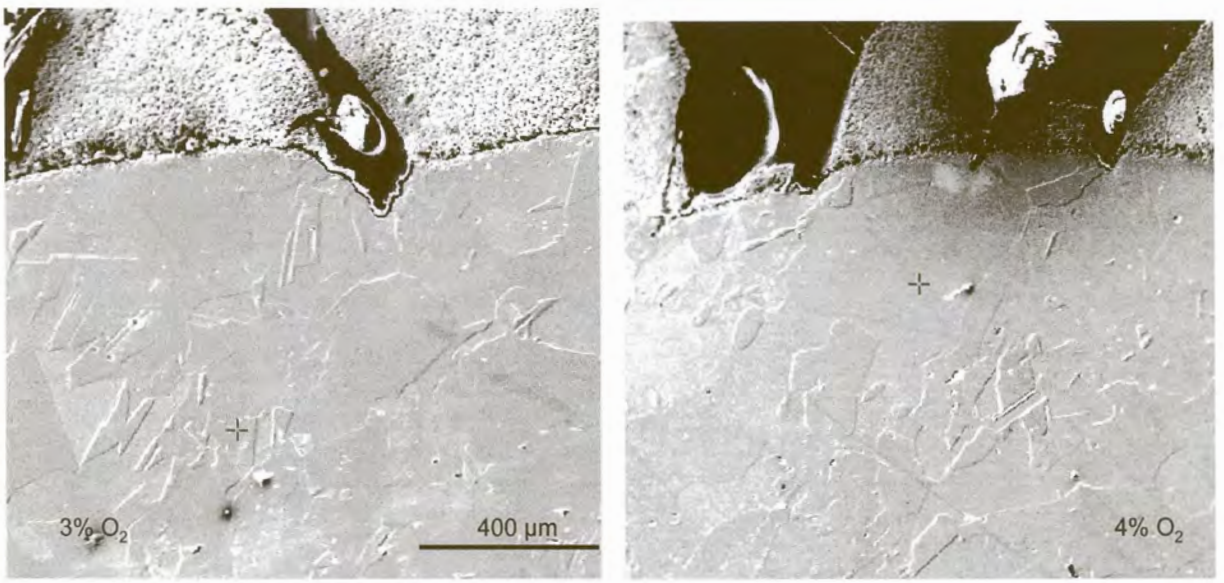

Figure 39 : Etched cross-sections of type 304 samples reheated at 1280 ^{0}C.

4.3. Comparison of type 304 and 412 stainless steel

The measured residual scale thicknesses for the two steel grades are shown in figures (24, 27, 31 and 36). These results show the behaviour of type 412 and type 304 to be quite different – while the former steel grade is quite sensitive to reheating time and excess oxygen; this is not the case for type 304. These differences (with time, atmosphere and steel grades) arise from differences in the structure of the scale. In figure 40, the appearance of the exterior surface of a descaled type 412 sample is presented.

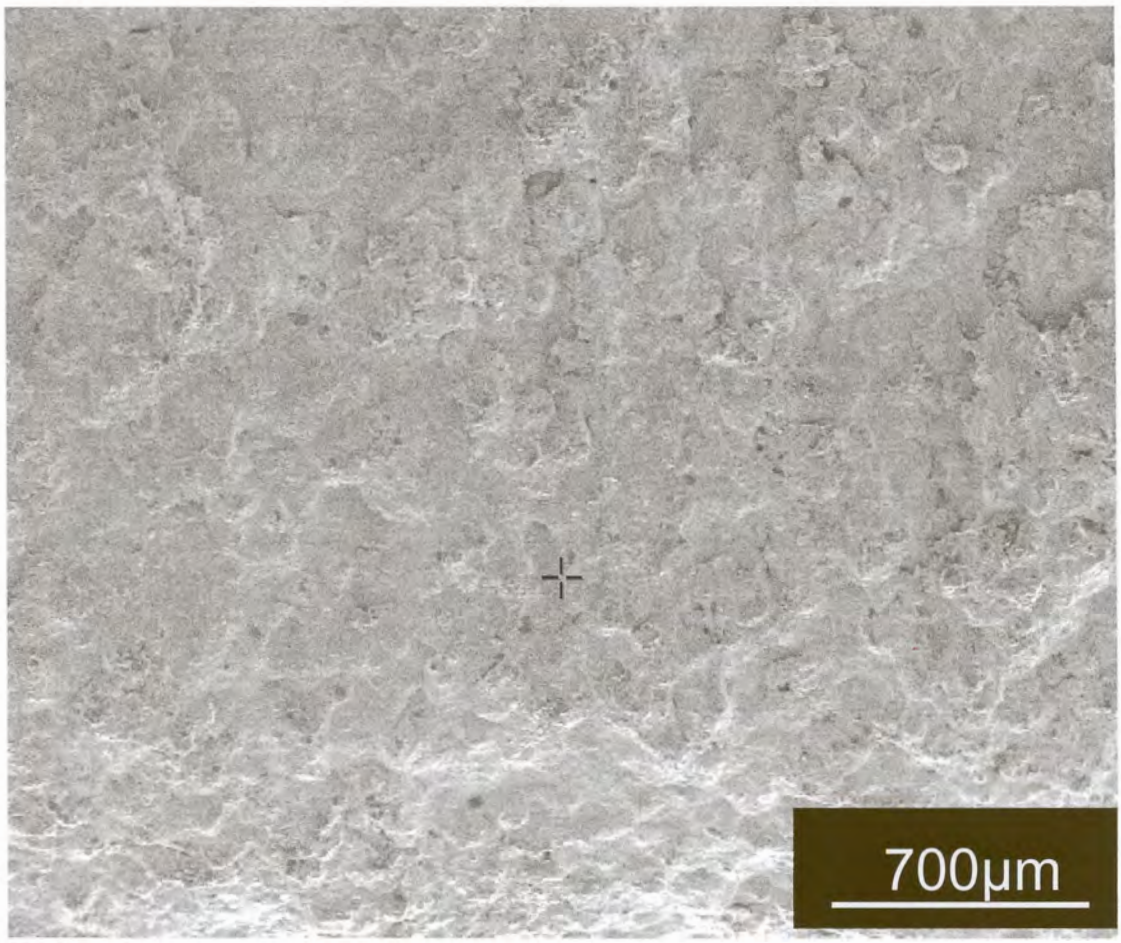

Figure 40 : Appearance of exterior surface of descaled type 412 sample

The correspondence between the austenite grain structure and the fracture paths for the type 304 stainless steel is evident in figure 41 below (as well as appendix 7), which shows the appearance of the as-descaled surface. The topography visible in this image is that of the residual scale attached to the stainless steel sample. The cracks through this residual scale can be seen to delineate a typical austenite grain structure.

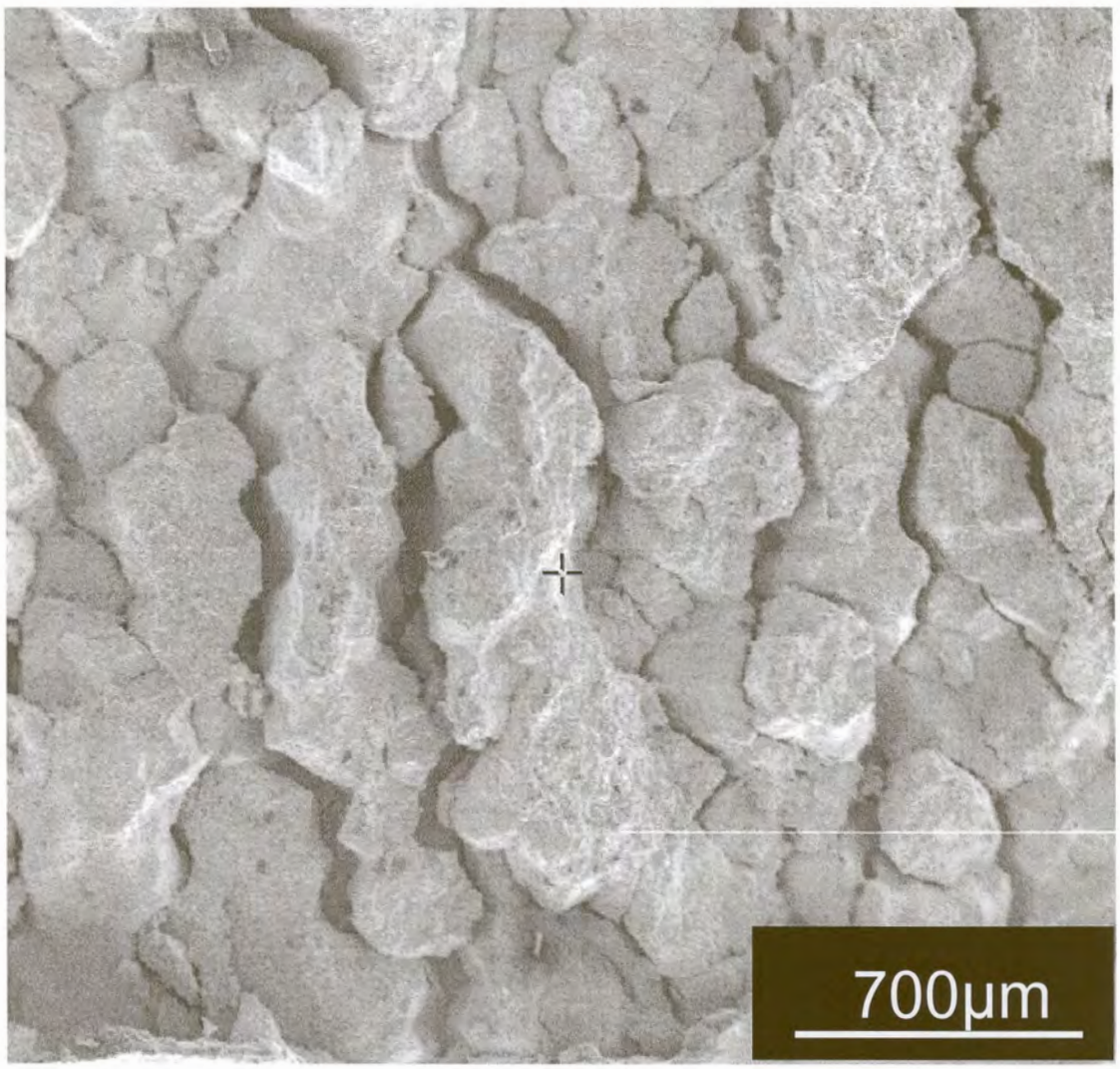

Figure 41 : Appearance of exterior surface of descaled type 304 sample, showing that the appearance of the cracked residual scale reflects the underlying austenite grain structure

5. Conclusion

The experimental results presented above indicate that the original hypothesis – that descaling is simply linked to the interfacial structure – does not fully explain the differences between steel grades and processing conditions. Descaling rather depends on the presence of metal-free fracture paths through the scale. In the case of type 412 stainless steel, these fracture paths lie at the outer edge of the entangled region (where the metallic fingers have been oxidized). The type 412 stainless steel showed greater sensitivity to reheating conditions and thus the amount of oxidation can be limited – by controlling the excess oxygen and the reheating time.

For type 304, the fracture paths followed the austenite grain boundaries (as a result of the formation of chromite layers at the grain boundaries, by internal oxidation). Control of the austenite grain structure is thus likely to have a strong effect on descaling for nickel-bearing stainless steel grades; small amounts of delta ferrite may serve to pin the austenite grain boundaries and so favour descaling (delta ferrite appears upon reheating at high temperatures, increasing in extent up to the melting point). Thus for the type 304, the effect of temperature on the residual scale thickness may probably be linked to the amount of delta ferrite that is formed and thus the austenite grain structure.

6. Recommendations

The difference in behaviour of the type 412 and 304 stainless steel suggests that different approaches favour descaling in industrial operations.

For type 412 (and by extension other nickel-free ferritic and martensitic grades) the amount of oxidation must be limited – by controlling the excess oxygen and the reheating time. For type 304, longer oxidation in more oxygen-rich atmospheres apparently favour descaling presumably because this allows more complete development of the chromite layers in the scale (the poor descaling of the samples reheated for only 1.5 hours likely originates from such an effect).

The grain structure of the as-cast slab also assumes an unexpected importance in descaling – if the extent of scale growth is such that the chill zone is fully oxidised, and the scale grows into the columnar zone, descaling is likely to be much poorer (and the extent of slab grinding is of relevant to this). This indirect effect may well account for much of the variability in descaling behaviour that is observed practically and perhaps this effect should be investigated as well. Thus samples from actual type 304 slabs (rather than rolled plate as used in this project) should be used to test the predicted effect of differences in grain structure on descaling. Actual scale samples from primary descaling operations could also be examined to test whether the predicted role of chromite layers is found in practice.

REFERENCES

Abuluwefa, H.T., Guthrie, R.I.L. and Ajersch, F., 1996, *The effect of oxygen concentration on the oxidation of low- carbon steel in the temperature range 1000 to 1250°C,* Oxidation of Metals, **46**, 423 - 440

Abuluwefa, H.T., Guthrie, R.I.L. and Ajersch, F., 1997, *Oxidation of low carbon steel in multi-component gases: Part 1. Reaction mechanisms during isothermal oxidation*, Metallurgical and Materials Transactions series A, **28**, A, 1633 - 1641

Abuluwefa, H.T., Guthrie, R.I.L. and Ajersch, F., 1997, *Oxidation of low carbon steel in multi-component gases: Part 2. Reaction mechanisms during reheating*, Metallurgical and Materials Transactions series A, **28**, A, 1643 - 1651

Ajersch, F., 1992, *Scale formation in steel processing operations*, Mechanical working &steel processing conference, **30**, 419-437

Akiyama, T., Ohta, H., Takahashi, R., Waseda, Y. and Yagi, J., 1992, *Measurement and modeling of thermal conductivity for dense iron oxide and porous iron ore agglomerates in stepwise reduction.* ISIJ International, **32**, 829 - 837

Asai, T., Soshiroda, T. and Miyaharea, M., 1997, *Influence of Ni impurity in steel on the removability of primary scale in hydraulic descaling*, ISIJ International, **37**, 272 - 277

Blazevic, D.T., 1987, *Rolled in scale - the consistent problem*, 4th International Steel rolling conference, **1**. Deauville, France, 1-3 June 1987, A38.1 - A38.13

Boggs, W.E., 1973, *The role of structural and compositional factors in the oxidation of iron and iron-based alloys in high temperature gas-metal reactions in mixed environments*, Metallurgical society of AIME, 84 - 128

Boggs, W.E., Sonon, D.E., 1978, *Method for improving the surface quality of stainless steels and other chromium-bearing iron alloys.*, United States Patent 4078949

Douglass, D.L., 1995, *A critique of internal oxidation in alloys during the post-Wagner era.* Oxidation of Metals, **44**, 81 - 111

Engell, H.J. and Peters, F.K., 1957, Arch.f.d. Eisenhuttenw, **28**, 567-574

FACT, thermo-chemical database, http://www.crct.polymtl.ca/fact/fact.htm

Folkhard, E., 1988, *Welding metallurgy of stainless steels.* Springer-Verlag Wien, New York, 10

Fresnedo, C. and Ruiz, J.M., 1996, *Change to mechanical descaling.* Wire Journal International, 70 - 73

Fujii, C.T. and Meussner, R.A., 1963, *Oxide structures produced on iron-chromium alloys by a dissociative mechanism.* Journal of the electrochemical society, **110**, 1195 - 1204

Fujii, C.T. and Meussner, R.A., 1964, *The mechanism of high temperature oxidation of iron-chromium alloys in water vapor*, Journal of the electrochemical society, **111**, 1215 - 1221

Fukugawa, T., Okada, H., Maehara, Y., 1994, *Mechanism of red-scale defect formation in Si-added hot-rolled steel sheets.* ISIJ International, **34,** 906 - 911

Fukutsuka, T., Nakamura, T., Sato, M., Kokubo, I. and Ishida, R., 1981, *Study of descaling of steel slabs before hot rolling*, Transactions of the Iron and Steel Institute of Japan, **21**, 699 - 707

Garceau R., 1997, *Mechanical descaling*, Wire Technology International, 63 - 65

Gibbs, G.B., 1981, *On the influence of metal lattice diffusion on oxidation of metals and alloys*, Oxidation of metals, **16**, 147 - 158

Grigg, C.R., Sexton, B.G. and Matteson, L.E., 1985, *1420 mm Hot strip mill control of rolled-in-scale*, 4th International Steel Rolling Conference, **1**, Deauville, France, A39.1 - A39.8

Hindham, H. and Whittle, D.P., 1982, *Microstructure, adhesion and growth kinetics of protective scale on metals and alloys,* Oxidation of metals, **18**, 245 - 284

Hosford, W.F. and Caddell, R.M., 1983, *Metal forming, mechanics and metallurgy*, Prentice-Hall, Englewood Cliffs, NJ.

Ito, M.; Tachibana, R.; Seino, Y.; Yamamoto, A.; Kawabata, Y. and Uchino, K., 1997, *Descaling behaviour of type-430 hot-rolled stainless steel coil*, Japanese Journal of Applied Physics, **36**, 7404 - 7410

Metals Handbook, 1980, American Society for Metals, **3**, 194

Knowlton, J, Caplan, P.E., 1985, *Rotameter Corrections for gas density.* American Industrial Hygiene Association Journal, **46**, B-10 - 16

Kofstad, P., 1988, *High temperature corrosion*, Elsevier, London

Laheij, M.A.J.T.H., van Loo, F.J.J and Metselaar, R., 1980, *Phase relations in the Fe-Cr-O system at 1200°C investigated by means of a diffusion couple technique.* Oxidation of Metals, **14**, 207 - 215

Levin, E.M., Robbins, C.R. and McMurdie, H.F., 1964, *Phase diagrams for ceramists*, The American ceramic society, Columbus, Ohio

Liekmeier F., 1982, *Mechanical descaling of wire rod by bending — Possibilities and limits*, Wire, **32**, 57 - 58

Matsuno, F., 1980, *Blistering and hydraulic removal of scale films of rimmed steel at high temperature*, Transactions of the Iron and Steel Institute of Japan, **20**,

Morris, P., Bagshaw, P. and Marston, H., 1996, *Descaling of steels in rolling mills*, Report EUR 15836, ECSC agreement no. 7210.EA/818, European commission, Technical steel research, Office for official Publications of the European Communities, Luxembourg.

Palin, G.M., August 1965, *Effect of heating conditions on the adhesion of the scale to the metal*, Stal in English, **8**, 677 - 679

Pickens, J.W., 1983, *The microstructure characteristics of oxide scale formed during bar processing*, 21st Mechanical working & steel processing conference, Philadelphia, USA, 26 - 28 Oct. 1983. Iron and Steel Society / AIME, Warrendale, USA, 39 - 65

Pieraggi, B., Rapp, R.A. and Hirth, J.P., 1995, *Role of interfacial defects in oxide scale growth.* Oxidation of Metals, **44**, 63 - 79

Rapp, R.A., 1984, *The high temperature oxidation of metals forming cation-diffusing scales,* Metallurgical Transactions Series B, **15B**, 195-212

Rapp, R.A., 1993, *Fundamental aspects of high-temperature corrosion,* Journal de Physique, Colloque C9, **3**, 1- 15

Sachs, K. and Tuck, C.W., 1968, *Surface oxidation of steel in industrial furnaces*, Proceedings of the conference held in London, 19 -20 December 1967, The iron and steel institute, London, 1 - 17

Sachs, K. and Tuck, C.W., 1970, *Scale growth during re-heating cycles*, Werkstoffe und korrosion, **21**, 945 - 954

Schutze, M., 1995, *Mechanical properties of oxide scales.* Oxidation of Metals, **44**, 29 - 61

Sheasby, J.S., Boggs, W.E. and Turkdogan, E.T., 1984, *Scale growth on steels at 1200 C: rationale of rate and morphology*, Metal science, **18**, 127 - 136

Sheppard, T. and Steen, W.M., 1970, *Hydraulic Descaling of steel: a preliminary experimental survey*, Journal of the Iron and Steel Institute, **7**, 797 - 805

Sheridan, A.T. and Simon, P., 1 February 1995, *Descaling of steels in rolling mills*, European steel-making developments and perspectives in rolling and reheating, Luxembourg, 233 - 244

Taniguchi, S., 1985, *Stress developed during oxidation of metals and alloys*, Transactions of the Iron and Steel Institute of Japan, **25**, 3 - 13

Tominaga, J., Wakimoto, K., Mori, T., Murakami, M., Yoshimura, T., 1982, *Manufacture of wire rods with good descaling property.* Transactions of the Iron and Steel Institute of Japan, **25**, 3 -13

Tuck, C.W. and Barlow, J., 1972, *The effect of reheating furnace atmosphere on the adhesion of scale to steel*, Iron and steel, **45**, 31 - 38

von Bogdandy, L. and Engell, H.J., 1967, *The reduction of iron ores,*Berlin-Heidelberg-New York, 83-89

Whittle, D.P. and Wood, G.C., 1967, *Complex scale formation on an iron-18% chromium alloy.* Journal of the Electrochemical Society, **114**, 986 - 993

Wagner, C., 1959, *Reaktionstypen bei der Oxydation von Legierungen.*, Zeitschrift fur Elektrochemie, **63**, 772-782.

Zittermann, J.A., Bacco, R.P. and Boggs, W.E., April 1982, *Factors affecting scale adhesion on steel forging*, Journal of metals, **34**, 4, 22 - 26

APPENDIX 1

ANALYSIS OF REACTION RATES AND KINETICS OF IRON

A.1.1 Introduction

This appendix presents an analysis of the rate of scale growth. The mechanisms generally observed for the oxidation of iron can be divided into two stages — an initial linear rate of oxidation, followed by a parabolic rate of oxidation. The initial mechanism is observed for short times up to a certain oxide thickness. Initial oxidation rates depend on the oxidizing species and the rate is expressed in terms of the rate of adsorption of the oxidizing species on the scale surface. When the oxide layer reaches a certain thickness, approximately 0.4 mm (Pettit and Wagner, 1964), the mechanism of oxidation becomes controlled by the diffusion of the ionic species through the oxide layer, leading to parabolic oxidation.

A.1.2 Analysis

A.1.2.1 Symbols used

t (s)	Time
x (m)	Scale thickness
$D_{Fe}(m^2/s)$	Self-diffusion coefficient of Fe^{2+} in iron oxides
$A(m^2)$	Surface area of the sample
G (mole/ m^3)	Molar volume of the oxide
K_p (g^2/m^4s)	Parabolic rate constant

ρ_{FeO} (g/m^3)	Density of FeO
M_o (g/ g-mole)	Molecular weight of atomic oxygen
M_{FeO} (g/g-mole)	Molecular weight of FeO
Y	Iron-ion vacancy fractions
β (m/s)	Mass-transfer coefficient
D_{O2} (m^2/s)	Diffusion coefficient of oxygen
u (m/s)	Gas velocity past the sample surface
l (m)	Length of the sample and
ν (m^2/s)	Kinematic gas viscosity.
T(K)	Temperature
R (J/mole K)	Gas constant
P (atm)	Pressure

A.1.2.2 Diffusion in the oxide

The parabolic oxidation mechanism is driven by the diffusion of metal ions and vacancies through the oxide layer and chemical equilibrium is maintained at the metal-oxide and oxide gas boundaries during the course of oxidation (Abuluwefa *et al*, 1996).

The diffusion of Fe^{2+} cations is expressed in terms of Fick's first law,

$$\frac{dn_{Fe}}{Adt} = \frac{3D_{Fe^{2+}}\,\Delta[Fe^{2+}]}{x}$$

Where $x = G\,\Delta n_{Fe}/A$ G = Molar volume of the oxide (m^3/mole Fe)

$$\text{Thus} \quad \frac{dn_{Fe}}{Adt} = \frac{3D_{Fe^{2+}}\Delta[fe^{2+}]}{G\Delta n_{Fe}\,/\,A}$$

$\Delta[Fe^{2+}]$= Concentration of cations in the scale and Δn_{Fe} = moles Fe^{2+}

The exponent 3 in this equation results from the parallel movement of electrons and cations in the scale layer (von Bogdandy and Engell, 1967)

By integration:

$$G\int_0^{\Delta n_{Fe}} dn_{Fe}\Delta n_{Fe} = 3\int_0^t D^* A^2 \Delta[Fe^{2+}]dt$$

$$\frac{\Delta n_{Fe}^2}{A^2} = \frac{6D_{Fe^{2+}}\Delta[Fe^{2+}]t}{G}$$

The parabolic rate constant gives the increase in mass (due to reacted oxygen) as follows:

$(\Delta m/A)^2 = K_p t$

It follows that the parabolic rate constant is given by

$K_p = 6xD_{Fe2+}\Delta[Fe^{2+}]\ M_o^2\ /G$

The molar volume of FeO (G) can be written as $G = M_{FeO}/\rho_{FeO}$

and the concentration of Fe^{2+} ions, $[Fe^{2+}] = \rho_{FeO}(1-y)/\ M_{FeO}$

$$K_p = \frac{6 * D_{Fe^{2+}} * \rho_{FeO}^2 * M_0^2 (y_{FeO/Fe_3O_4} - y_{Fe/FeO})}{M_{FeO}^2} \qquad (A)$$

$y_{FeO/Fe3O4}$ and $y_{Fe/FeO}$ are the iron vacancy fractions at the FeO/Fe_3O_4 and Fe/FeO boundaries respectively. The vacancy concentrations are determined from the wustite-magnetite (y = 0.14) and iron-wustite (y = 0.049) equilibria respectively (Ajersch, 1992). The self-diffusion coefficient (cm^2/s) of Fe^{2+} in FeO can be calculated as below

$D_{Fe2+} = 4.5x10^{-2}exp(-6641/RT)$ (Deich and Oeters, 1973)

By differentiation of $(\Delta m/A)^2 = K_p t$ the following is obtained:

$$2 * \frac{\Delta m}{A} * \frac{d(\Delta m)}{Adt} = K_p$$

Where

$$\frac{\Delta m}{A} = \frac{x\rho_{FeO}M_o}{M_{FeO}} \qquad (x = \text{thickness of scale})$$

Thus

$$\frac{d(\Delta m / A)}{dt} = \frac{K_p M_{FeO}}{2x\rho_{FeO}M_o}$$

This rate of scale growth is matched by molecular oxygen transfer to the scale-gas interface:

$$\frac{d(n_{O2} / A)}{dt} = \frac{K_p M_{FeO}}{x\rho_{FeO}M_{O2}^2} \qquad (B)$$

Where $d(n_{O2}/A)dt$ gives the rate of oxygen transfer to the scale surface. This can be determined as follows:

$$\frac{n_{O2}}{A} = \beta\Delta C_{O2}$$

Thus the oxidation rate in terms of the oxygen mass transfer is:

$$\frac{n_{Fe^{2+}\rightarrow FeO}}{A} = 2 * \beta\Delta C_{O2} = 2 * \beta\Delta P_{O2} / RT \qquad (C)$$

In which β is the mass transfer coefficient (m/s). The equation expressing β for gas-phase mass-transport control is

$$\beta = \frac{4}{3}\frac{D_{O2}}{l}(Re)^{\frac{1}{2}}(Sc)^{\frac{1}{3}}$$

Where Re is the Reynolds number (ul / ν), Sc is the Schmidt number (ν / D_{O2}), u is the gas velocity past the sample surface, l is the length of the sample and ν is the kinematic gas viscosity (Abuluwefa *et al*, 1996).

A.2.3 Application of Analysis

A.2.3.1 Conditions used in analysis

Gas constant, R = 8.314 J/mole K

Furnace temperature, T = 1500 K

Diffusion coefficient of Fe^{2+}, $D_{Fe2+} = 3.98x10^{-10}$ m^2/s

Molecular weight of FeO, $M_{FeO} = 0.07185$ kg/mole

Density of FeO, $\rho_{FeO} = 5883$ kg/m^3

Molecular weight of atomic oxygen, $M_O = 0.016$ kg/mole

Pressure, P = 0.865 atm

Diffusion coefficient of O_2, $D_{O2} = 3.27x10^{-4}$ m^2/s

Length of sample, l = 0.1 m

Gas velocity, u = 0.1 m/s

Kinematic viscosity of the gas, $\nu = 2.3*10^{-4}$ m^2/s

Equilibrium iron vacancy fraction at the Fe/ FeO boundary, $y_{Fe/FeO} = 0.049$

Equilibrium iron vacancy fraction at the FeO/ Fe_3O_4 boundary, $y_{FeO/Fe3O4} = 0.14$

Using the above data, the parabolic rate constant (K_p) was calculated as $3.7*10^{-4}$ kg^2/m^4s which is in the same range as the value ($3.11*10^{-4}$ kg^2/m^4s) calculated by Sachs and Tuck (1970). Using equation B, the rate of mass transfer of Fe^{2+} was calculated for various scale thicknesses and the graph below shows the relation between the oxidation rate and the scale thickness.

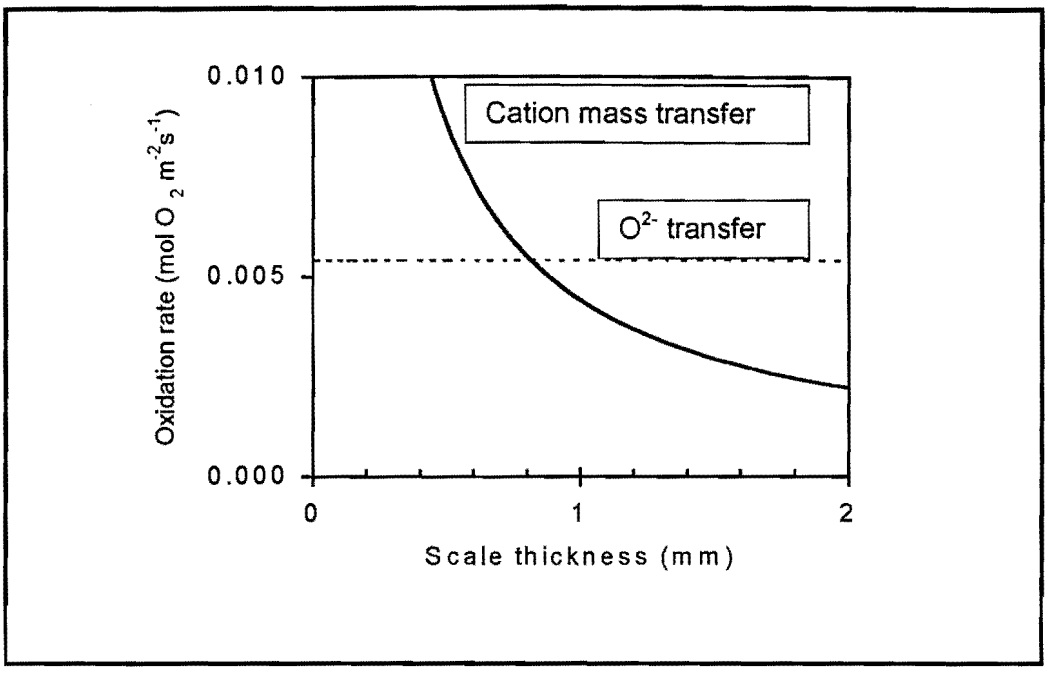

The dotted line represents the situation where oxygen mass transfer is the limiting case and the solid graph represents where cation mass transfer is the limiting case. From the above graph, it can be seen that FeO is present up to a thickness of between 0.4 and 0.5 mm, beyond this thickness, the rate-controlling step becomes the arrival of Fe^{2+} at the interface.

The overall oxidation rate is illustrated in the figure below:

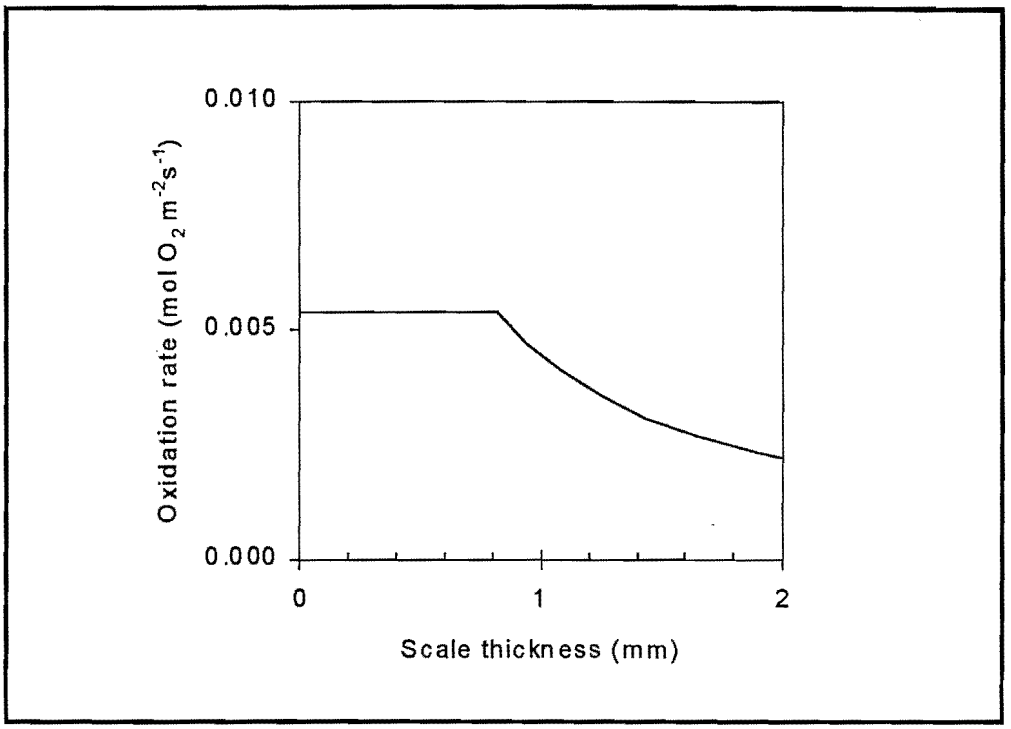
0.010
0.005
0.000
Oxidation rate (mol O_2 $m^{-2}s^{-1}$)
0
1
2
Scale thickness (mm)

APPENDIX 2

THEORETICAL ANALYSIS OF POSSIBLE MECHANISMS OF HYDRAULIC DESCALING

A.2.1 Introduction

This appendix presents an analysis of descaling mechanisms. Each of these mechanisms has been considered as being independent, thus avoiding the complication that would otherwise follow from possible interactions between them. It is recognized that synergistic interactions may arise in practice. This analysis is largely taken from Morris *et al*, (1996).

A.2.2 Analysis

A.2.2.1 Symbols used

P (Pa)	Impact pressure of descaling jet
T	Temperature
ρ (kg/m^3)	Density of water
G (m^3/s)	Volume flow rate of water
t (m)	Thickness of jet
B (m)	Width of steel being descaled
v (m/s)	Speed of steel under jet
θ (^{0})	Angle of jet from vertical
ρ_s (kg/m^3)	Density of scale

α ($°C^{-1}$)	Coefficient of thermal expansion of scale
°C (J/kg °C)	Specific heat capacity of scale
E (N/m^2)	Elastic modulus of scale
K (W/m °C)	Thermal conductivity of scale
x (m)	Thickness of scale
l (m)	Distance between through scale cracks
σ (J/ m^2)	Energy required to separate scale from steel
ε_c	Compressive strain to failure of scale
ε_T	Tensile strain to failure of scale
J (N/m^2)	Shear strength of scale / metal interface

A.2.2.2 Effect of thermal shock on scale

Some quantitative indication of whether thermal shock is a feasible mechanism can be obtained by estimating the time required to cool the scale to a depth. Assuming that conduction through the scale is rate determining, the time to cool the scale is of the order of l^2/α, where *l* is the scale thickness and α, the thermal diffusivity.

The time that the steel takes to traverse the thickness of the jet = t/v. This is the minimum time for which the scale would experience a cooling effect from the water; the real time will be longer than this owing to spreading of the water over the scale. The thickness of scale, which would be cooled, can therefore be estimated as:

$$\left(\frac{K}{p_s C}\frac{t}{v}\right)^{\frac{1}{2}} \qquad \text{(A3.1)}$$

If this distance is less than the total scale thickness (quantitatively tested in section A.1.3.2), then the scale / metal interface will not be directly cooled by the jet. There

will be contraction stresses in the outer layers of the scale, which would lead to fracture of the scale, with de-cohesion taking place by a shear effect leading to tensile forces across the scale / metal interface.

A.2.2.3 Effect of deformation of scale

The vertical component of the pressure of the water jet on the scale may crush and shatter the scale, following which the pieces of scale are removed by the water.

Compressive stress on scale = vertical component of pressure jet = P Cos θ

Compressive strain in steel = (P/E) Cos θ

The condition for descaling by this mechanism is:

$$(P/E) \cos\theta > \varepsilon_c \quad \ldots\ldots\ldots\ldots\ldots\ldots\ldots\ldots\ldots\ldots\ldots A3.2$$

This assumes that the pressure exerted by the jet is uniform over its entire area of impact.

A.2.3 Application of Analysis

A.2.3.1 Conditions used in analysis

Density of water, ρ = 1000Kg/m^3

Molecular weight of water, m = 18 g/mole

Density of FeO at 1000°C, ρ_s = 5500 kg/m^3

Heat capacity of scale, C_p = 65J/K (FACT, 1988)

Thermal diffusivity, = 8.3 * 10^{-7} m^2/s (in the vicinity of 1100°C)

Thermal conductivity of scale, k = 4.2 W/ m K (Akiyama *et al*, 1992)

Quantities relating to mechanical properties of scale at rolling temperatures are not very well known. Estimates of their likely magnitudes can however be obtained from published work.

Coefficient of expansion, $\alpha = 13.5 * 10^{-6} °C^{-1}$ (this is the average values for FeO and Fe_2O_3)

Elastic modulus of scale, $E = 18*10^4$ MN m^{-2} (from Hancock *et al.*, 1974)

Tensile strain to failure, $\varepsilon_T = 2.3*10^{-4}$ (Hancock P., 1980)

Compressive strain to failure, $\varepsilon_c = 40*10^{-4}$ (no reference available. An estimate of the probable magnitude of ε_c, has therefore been made based on (Hancock, 1980)

Energy required to fracture scale / metal interface = 1 J/m (estimate, no reference found)

Shear strength of scale/metal interface, J = 20 MN m^{-2} (estimate based on the fact that tensile strengths of the interface of this order have been measured at room temperatures, (Hancock *et al.*, 1974).

For typical commercial practice,

Impact pressure, $P = 1*10^6$ Pa

Volume flow rate, $G = 1*10^{-3}$ m^3/s

Thickness of jet, $t = 8*10^{-3}$ m

Width of steel, B = 0.1 m (assuming descaling of a billet)

Speed of steel, v = 1 ms^{-1}

Angle of jets from vertical, $\theta = 15^0$ (a typical value, although higher angles are used in some mills).

A.2.3.2 Effects of thermal shock on scale

Using literature values for the thermal conductivity and density of wustite (Akiyama *et al*, 1992) and its heat capacity (FACT, 1998), the thermal diffusivity is estimated to be some $8.3*10^{-7}$ m^2/s in the vicinity of 1100°C. Based on the typical thickness of the jet of around 8 mm, and slab speeds of 0.1 to 1 m/s (Morris *et al*, 1996), the time that the scale is exposed to the water jet is between 8 and 80 ms — which, based on the thermal diffusivity, is only sufficient time to quench the outer 80 - 250 μm of the scale (compared with the total scale thickness which may be 2 mm or more after reheating). This very limited cooling of the scale does bring the validity of the thermal shock mechanism into doubt.

Equation A3.1 gives the depth of scale, which would experience cooling as a result of the effects of the water jets. This expression is calculated to be 0.2 mm. This assumes that the cooling effect lasts only as long as the steel is under the water jets, which is an unrealistic assumption since water lying on the surface of the scale will continue to cool it. It appears, however, that the scale/ metal interface is unlikely to be cooled if the scale is more than a few millimeters thick, and therefore under these circumstances the scale removal mechanism cannot depend on uniform cooling of the scale. Tensile stresses in the scale surface, caused by cooling of the outer layer of the scale, must however lead to the generation of compressive stresses in the lower layers of the scale, resulting in a shear stress at the scale / metal interface.

A.2.3.3 Effect of deformation of scale

Equation A3.2 gives the condition for descaling to take place by crushing of the scale. It can be seen that this mechanism is expressly dependent on the impact pressure generated by the descaling system. Therefore, calculating the left-hand side we have:

APPENDIX 3

REQUIRED GAS FLOW RATES IN FURNACE

Introduction

The gas composition was chosen to simulate the combustion of CH_4 with air, with 3% or 4% excess free oxygen as shown in the calculations below. In this specific example, the gas composition was calculated using 3% excess oxygen.

	CH_4	$+ 2O_2$	$+ N_2$	=	CO_2	$+ 2H_2O$	$+ N_2$	$+ O_2$
MM	16	32	28		44	18	28	32
Moles	1	2	7.5		1.0	2.0	8.9	0.4

Using "goal seek" the % excess oxygen that must enter to ensure that 3% excess O_2 is obtained in the exit gas, can be calculated.
Thus for a calculated 18.4 % O_2 entering, the rest of the mass balance is as follows:

CH_4	$+ 2O_2$	$+ N_2$	=	CO_2	$+ 2H_2O$	$+ N_2$	$+ O_2$
	2.4	8.9		8.1	16.3	72.6	3.0

The total volume of gas flowing through the furnace is then calculated as follows:

Dimensions of tube (cm)

Outside	Inside	Length (cm)	
9	7.6	100	
Area (πr^2)	0.0045	m^2	r = inside radius of tube
Vtot	8E-05	Nm^3/s	Vtot = total volume of gas (area x velocity)

Where the gas velocity is 0.1m/s.

Thus the flow rates of the individual gases through the furnace should be:

	Nm^3/s	L/min	Mole/s
VN_2	6E-05	3.59	0.0024
VO_2	2E-06	0.15	0.0001
VCO_2	7E-06	0.40	0.0003

The following tables show the rotameter calibration values of the various gases using the soap bubble meter.

Nitrogen calibration

Pressure drop	Rotameter Nr.	ml	time	ml	time	ml	time	ml	time	ml	time	l/min
85	1	100	4.37	100	4.2	100	4.36	200	8.65	200	8.65	1.39
108	2	100	2.34	100	2.34	100	2.34	200	4.85	200	4.82	2.53
122	3	100	1.66	100	1.57	100	1.58	200	3.23	200	3.28	3.72
143	4	100	1.2	100	1.16	100	1.18	200	2.35	200	2.38	5.08
162	5	100	0.87	100	0.84	100	0.85	200	1.85	200	1.82	6.84

Rotameter Nr.	measured rate	Rotameter Nr.	rate using equation
1	1.39	1	1.22
2	2.53	2	2.57
3	3.72	3	3.91
4	5.08	4	5.26
5	6.84	5	6.60

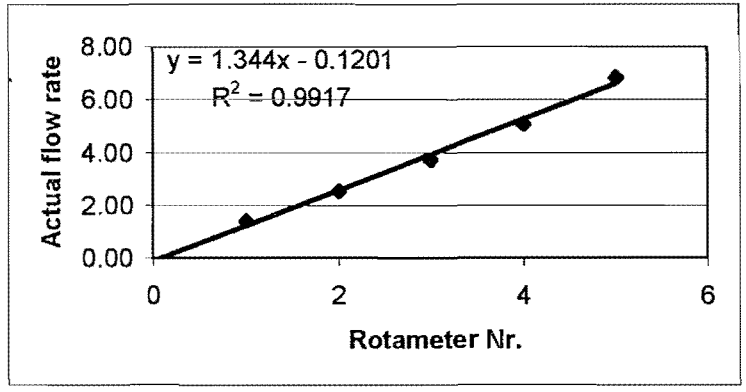

APPENDIX

Oxygen calibration

Pressure drop	Rotameter nr.	ml	time	ml	time	ml	time	ml	time	ml	time	l/min
mmHg												
87	220	15	3.45	20	4.85	15	3.66	20	4.82	15	3.48	0.25
87	200	15	3.81	20	5.08	10	2.48	15	3.81	20	5.11	0.24
86	150	15	5.05	20	6.62	15	5.04	20	6.64	20	6.61	0.18
80	100	15	7.94	15	7.74	10	5.22	15	7.91	10	5.1	0.12
76	50	10	9.48	10	9.4	15	14.19	15	14.18	10	9.2	0.06
		10	9.34	15	14.05	10	9.46	15	14.18	15	14.5	0.06

Rotameter Nr.	measured rate
220	0.25
200	0.24
150	0.18
100	0.12
50	0.06

Rotameter Nr.	rate using equation
220	0.264
200	0.24
150	0.18
100	0.12
50	0.06

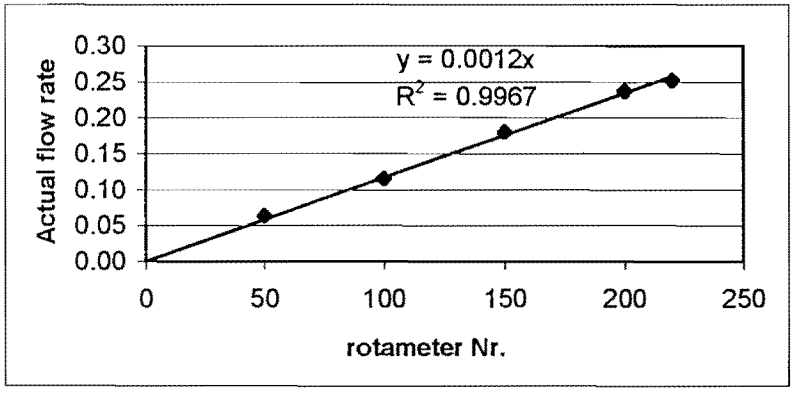

CO_2
calibration

Pressure drop	rotameter nr.	ml	time	ml	time	ml	time	ml	time	ml	time	l/min
(mmHg)	50	100	70.51	100	70.31	100	69.21	100	69.27	100	68.73	0.09
	100	100	42.53	100	42.44	100	42.56	100	42.31	100	42.1	0.14
	150	100	31.6	100	31.54	100	31.61	200	61.23	100	30.5	0.19
84	200	25	5.1	25	5.05	30	6.21	30	6.27	30	6.22	0.29
	250	100	16.59	200	33.36	100	16.81	200	33.17	200	33.26	0.36
88	300	25	3.53	25	3.58	30	4.34	25	4.32	30	3.6	0.42
	350	100	12.53	200	24.73	100	12.13	200	24.41	100	12.33	0.49
91	400	25	2.91	30	3.44	30	3.52	30	3.46	25	2.99	0.51
96	500	25	2.39	25	2.42	30	2.86	25	2.34	30	2.89	0.63
101	600	35	3.02	35	3.11	35	3	30	2.56	20	1.72	0.69

rotamete nr.	measured rate	rotameter nr.	rate using equation
50	0.09	50	0.65
100	0.14	100	1.3
150	0.19	150	1.95
200	0.29	200	2.6
250	0.36	250	3.25
300	0.42	300	3.9
350	0.49	350	4.55
400	0.51	400	5.2
500	0.63	500	6.5
600	0.70	600	7.8

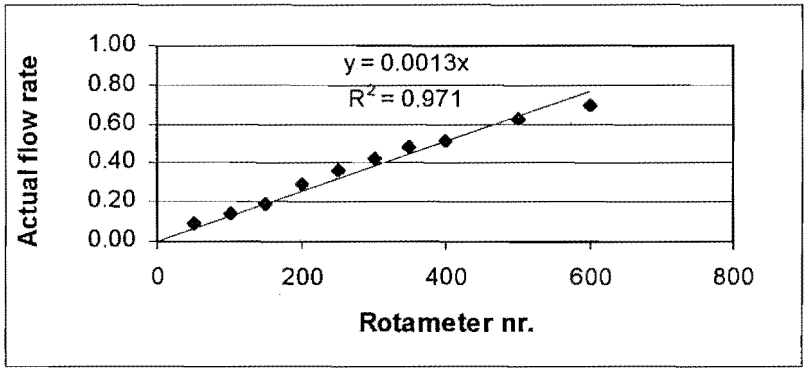

Rotameter corrections for gas density were done since changes in gas density could significantly affect the airflow measurements by rotameters. Using a rotameter at an altitude different than that, for which it was calibrated, could yield serious error. From the observed flow rate at the bubble tower (V1), the flow rate at the rotameter (V2) at 0.865 atm could be calculated using the following equation

Flow rate through rotameter (V2) = (P_{atm} / P_{rot}) x Observed flow rate (V1)

V3 – the flow rate at the rotameter at 1 atm was then calculated and as a check, V2 was then recalculated as shown below.

$$R_2 = R_1\sqrt{\frac{P_2}{P_1}}$$

Where R is the rotameter reading and P is the pressure.

N2

Patm = 87624.5 P3 = 101300 T(K) = 298

rotameter setting	Prot mmHg	Pabs Pa	V1 at bubble tower (l/min)	V2 at rotameter = V1*Patm/prot	V3 at rot at 1atm = V2/sqrt(Prot/P3)	V2 at rot = V3/sqrt(P3/P2)		n (mol/s) ProtV2/RT
1	85	98954	1.39	1.23	1.25	1.23		0.00082
2	108	102020	2.53	2.17	2.17	2.17		0.00149
3	122	103886	3.72	3.14	3.10	3.14		0.00219
4	143	106685	5.08	4.17	4.07	4.17		0.00300
5	162	109217	6.84	5.48	5.28	5.48		0.00403

O2

Patm = 87624.5 P3 = 101300 T(K) = 298

rotameter setting	Prot mmHg	Pabs Pa	V1 at bubble tower (l/min)	V2 at rotameter V1*Patm/prot	V3 at rot at 1atm V2/sqrt(Prot/P3)	V2 at rot V3/sqrt(P3/P2)		n (mol/s) ProtV2/RT
220	87	99221	0.25	0.22	0.23	0.22		0.00015
200	87	99221	0.24	0.21	0.21	0.21		0.00014
150	86	99087	0.18	0.16	0.16	0.16		0.00011
100	80	98288	0.12	0.10	0.10	0.10		0.00007
50	76	97755	0.06	0.06	0.06	0.06		0.00004

CO2

Patm = 87624.5 P3 = 101300 T(K) = 298

rotameter setting	Prot mmHg	Pabs Pa	V1 at bubble tower (l/min)	V2 at rotameter V1*Patm/prot	V3 at rot at 1atm V2/sqrt(Prot/P3)	V2 at rot V3/sqrt(P3/P2)		n (mol/s) ProtV2/RT
200	84	98821	0.19	0.17	0.17	0.17		0.000113
300	88	99354	0.36	0.32	0.32	0.32		0.000212
400	91	99754	0.49	0.43	0.43	0.43		0.000287
500	96	100420	0.51	0.45	0.45	0.45		0.000303
600	101	101087	0.63	0.54	0.55	0.54		0.000370

Patm atmospheric pressure
Pabs absolute pressure
Prot measured pressure at rotameter

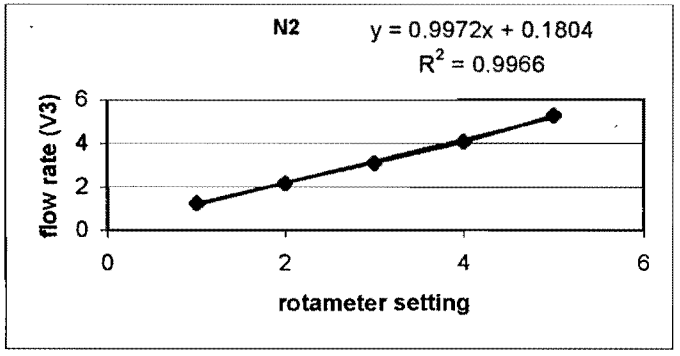

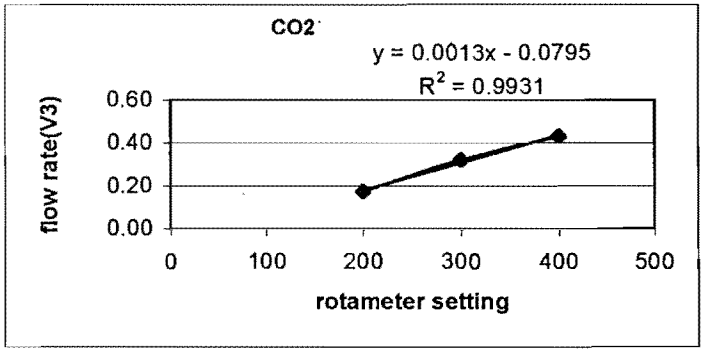

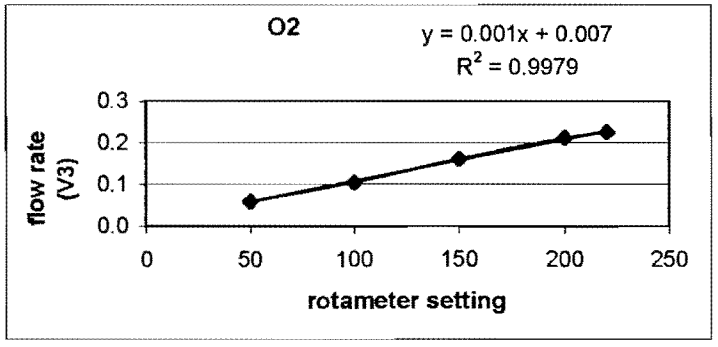

APPENDIX

Thus from the above calculations and graphs, it follows that for a given rotameter setting, the flow rate at the rotameter at 1 atm, can be calculated.

N2

Patm =	101300	pa				T(K) =	298
rotameter setting	Prot mmHg	Pabs Pa	V3 at 1atm	V2 at Pabs V3*sqrt(Prot/Patm)			n at Pabs
3.42	141	120093.8	3.59	3.91			0.00316

O2

Patm =	101300	pa				
rotameter setting	Prot mmHg	Pabs Pa	V3 at 1atm	V2 at Pabs V3*sqrt(Prot/Patm)		n at Pabs
142	141	120093.8	0.15	0.16		0.000131

CO2

Patm =	101300	pa				
rotameter setting	Prot mmHg	Pabs Pa	V3 at 1atm	V2 at Pabs V3*sqrt(Prot/Patm)		n at Pabs
372	141	120093.8	0.40	0.44		0.000355

Patm	atmospheric pressure
Pabs	absolute pressure
Prot	pressure at rotameter

APPENDIX 4

EXPERIMENTAL GAS ANALYSES AND WATER CONTENT

The calculated inlet gas compositions for:

3% excess O_2 in the exit gas is: 3.6 % O_2, 86.7% N_2, and 9.7% CO_2

4% excess O_2 in the exit gas is: 4.7 % O_2, 86.2% N_2, and 9.1% CO_2

16-05-2000

Calibration of inlet gas for 3% excess O_2 in exit gas

	%	%	%	%	%	%
O_2	3.51	3.41	3.27	3.23	3.17	3.12
N_2	88.31	87.92	88.8	88.22	88.33	88.41
CO_2	8.19	8.66	8.55	8.55	8.5	8.47

Calibration of inlet gas for 4% excess O_2 in exit gas

	%	%	%	%	%	%
O_2	4.28	4.31	4.42	4.34	4.29	4.37
N_2	88.07	87.95	87.88	87.89	87.98	87.75
CO_2	7.65	7.74	7.69	7.76	7.73	7.87

23-05-2000

Calibration of inlet gas for 3% excess O_2 in exit gas

	%	%	%	%	%	%	%	%	%
O_2	3.09	3.13	2.97	2.9	2.88	2.88	3.15	2.96	2.96
N_2	88.58	88.61	88.67	88.81	88.86	88.88	88.62	88.82	88.77
CO_2	8.34	8.26	8.36	8.28	8.26	8.24	8.23	8.22	8.27

Calibration of inlet gas for 4% excess O_2 in exit gas

	%	%	%	%	%	%
O_2	4.26	4.28	4.27	4.28	4.29	4.26
N_2	87.78	87.72	87.74	88.08	87.96	87.76
CO_2	7.96	8.01	7.98	7.65	7.75	7.98

15-09-2000

Calibration of inlet gas for 3% excess O_2 in exit gas

	%	%	%	%	%	%	%
O_2	3.48	3.53	3.47	3.54	3.49	3.53	3.61
N_2	86.96	86.4	86.75	86.93	86.74	68.84	86.64
CO_2	9.56	10.07	9.78	9.54	9.77	9.64	9.74

Calibration of inlet gas for 4% excess O_2 in exit gas

	%	%	%	%	%
O_2	4.94	4.88	4.91	4.86	4.79
N_2	86.1	85.88	85.93	86.08	86.29
CO_2	8.95	9.24	9.15	9.06	8.92

Water content of gas mixture

Some preliminary experiments were done to ensure that the correct amount of vapour entered the furnace. This was done by passing the exit gas at the bottom of the furnace through a drierite column that had been pre-weighed. After the experiment the drierite column was then weighed again. The difference between the two weights, gave the amount of water that had been absorbed by the drierite.

mass drierite (g)	376.08
drierite +water	397.57
water (g)	21.49

This value (21.49g, in this case) was then compared to the theoretically calculated mass of water that was expected to be in the gas mixture at the laboratory temperature and pressure.

Total gas flow rate (l/min)	Time (min)	Total gas volume (l)	Temperature (K)	Pressure (Pa)	Moles of gas
5	30	150	299	87624.5	5.287

The moles of gas (N_2, O_2 and CO_2) above, was calculated from the ideal gas law.

% Water in final gas mixture	Moles of water	Mass (g) of water	
16.3	1.030	18.53	

The % water in the gas mixture was calculated as shown in appendix 3. The moles of water was then calculated as follows:

[5.287 / (1- 16.3 / 100)] * (16.3 / 100) = 1.03 moles

In all of the experiments the mass of water (theoretical and measured) were quite similar, as in the above example.

APPENDIX 5

PHASE ANALYSIS COMPOSITIONS OF METAL AND SCALE

The phase analyses of some of the samples are given below:

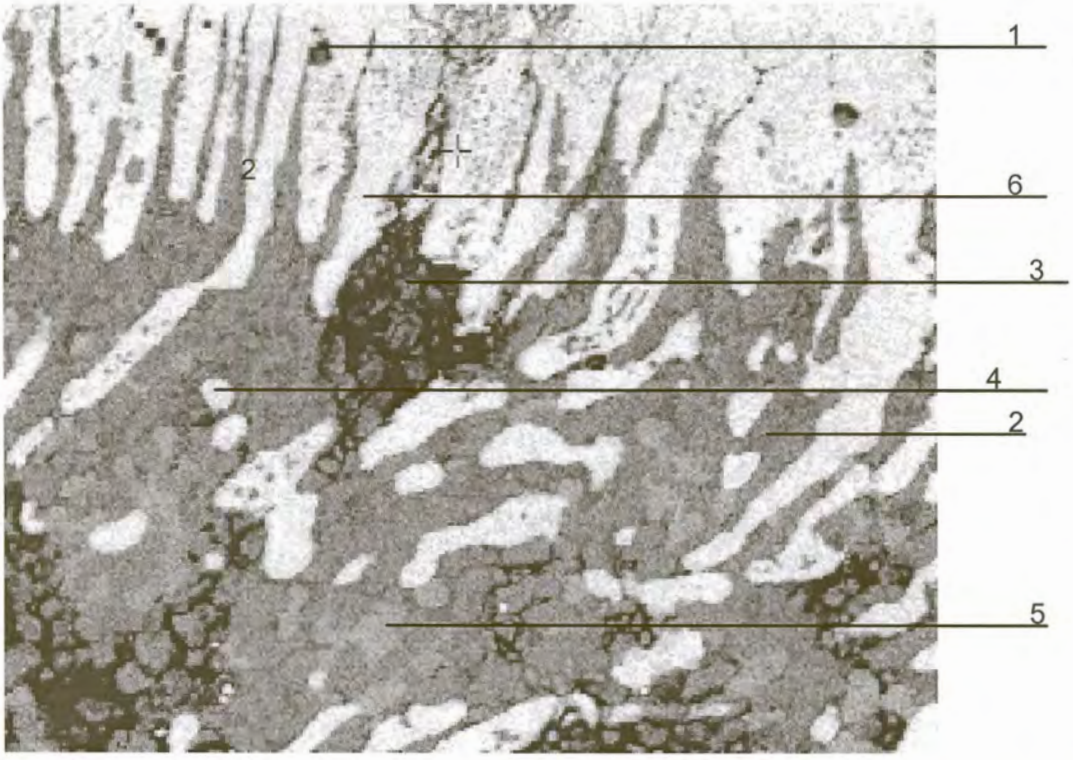

The above diagram shows the structure of scale for type 412 stainless steel reheated at 1210^0C in an atmosphere with 4% excess oxygen for 6hr. The analyses of the different phases are given below.

Point 1

Tue Oct 31 06:58:06 2000

Filter Fit Method
Chi-sqd = 2.11 Livetime = 73.0 Sec.

Element	k-ratio (calc.)	ZAF	Atom %	Element Wt %	Wt % Err. (3-Sigma)
Fe-K	0.2683	1.067	26.55	28.62	+/- 1.98
Ni-K	0.0000	1.051	0.00	0.00	+/- 0.00
Cr-K	0.5067	1.000	50.48	50.67	+/- 2.38
Mn-K	0.0062	1.041	0.61	0.65	+/- 1.30
Si-K	0.0065	1.332	1.59	0.86	+/- 0.24
Ti-K	0.2080	0.923	20.77	19.20	+/- 1.27
Total			100.00	100.00	

Point 2

Filter Fit Method
Chi-sqd = 2.60 Livetime = 84.0 Sec.

Element	k-ratio (calc.)	ZAF	Atom %	Element Wt %	Wt % Err. (3-Sigma)
Fe-K	0.1620	1.075	15.78	17.41	+/- 1.54
Ni-K	0.0050	1.049	0.45	0.52	+/- 1.04
Cr-K	0.4083	1.037	41.25	42.35	+/- 2.14
Mn-K	0.0081	1.061	0.79	0.86	+/- 1.15
Si-K	0.0066	1.292	1.53	0.85	+/- 0.21
Ti-K	0.4005	0.949	40.19	38.01	+/- 1.52
Total			100.00	100.00	

Point 3

Chi-sqd = 2.25 Livetime = 73.0 Sec.

Element	k-ratio (calc.)	ZAF	Atom %	Element Wt %	Wt % Err. (3-Sigma)
Fe-K	0.4817	1.045	48.55	50.34	+/- 2.45
Ni-K	0.0000	1.052	0.00	0.00	+/- 0.00
Cr-K	0.5048	0.940	49.13	47.44	+/- 2.24
Mn-K	0.0196	1.019	1.96	2.00	+/- 1.28
Si-K	0.0010	1.393	0.28	0.15	+/- 0.23
Ti-K	0.0008	0.892	0.08	0.07	+/- 0.36
Total			100.00	100.00	

Point 4

Filter Fit Method
Chi-sqd = 2.39 Livetime = 47.0 Sec.

Element	k-ratio (calc.)	ZAF	Atom %	Element Wt %	Wt % Err. (3-Sigma)
Fe-K	0.9667	1.001	96.67	96.77	+/- 4.03
Ni-K	0.0109	1.055	1.10	1.15	+/- 1.18
Cr-K	0.0256	0.797	2.19	2.04	+/- 0.89
Mn-K	0.0004	1.019	0.04	0.04	+/- 0.73
Si-K	0.0000	1.468	0.01	0.00	+/- 0.20
Ti-K	0.0000	0.918	0.00	0.00	+/- 0.00
Total			100.00	100.00	

Point 5

Chi-sqd = 0.98 Livetime = 77.0 Sec.

Element	k-ratio (calc.)	ZAF	Atom %	Element Wt %	Wt % Err. (3-Sigma)
Fe-K	0.4509	1.050	45.48	47.32	+/- 3.25
Ni-K	0.0000	1.052	0.00	0.00	+/- 0.00
Cr-K	0.5448	0.946	53.19	51.53	+/- 2.29
Mn-K	0.0081	1.019	0.81	0.83	+/- 1.30
Si-K	0.0014	1.388	0.37	0.20	+/- 0.22
Ti-K	0.0014	0.888	0.14	0.12	+/- 0.35
Total			100.00	100.00	

Point 6

Filter Fit Method
Chi-sqd = 2.46 Livetime = 36.0 Sec.

Element	k-ratio (calc.)	ZAF	Atom %	Element Wt %	Wt % Err. (3-Sigma)
Fe-K	0.9665	1.001	96.56	96.78	+/- 4.69
Ni-K	0.0093	1.055	0.93	0.98	+/- 1.22
Cr-K	0.0266	0.797	2.27	2.12	+/- 0.57
Mn-K	0.0000	1.019	0.00	0.00	+/- 0.00
Si-K	0.0008	1.468	0.23	0.12	+/- 0.23
Ti-K	0.0000	0.918	0.00	0.00	+/- 0.00
Total			100.00	100.00	

The next diagram below shows the structure of scale for type 304 stainless steel reheated at 1280^0C in an atmosphere with 3% excess oxygen for 6hr. The analyses of the different phases are also given below. Points 1 and 2 show the compositions of the metal at the scale-metal interface, whilst points 3, 4 and 7 actually show the composition of the chromium-depleted metal within the scale.

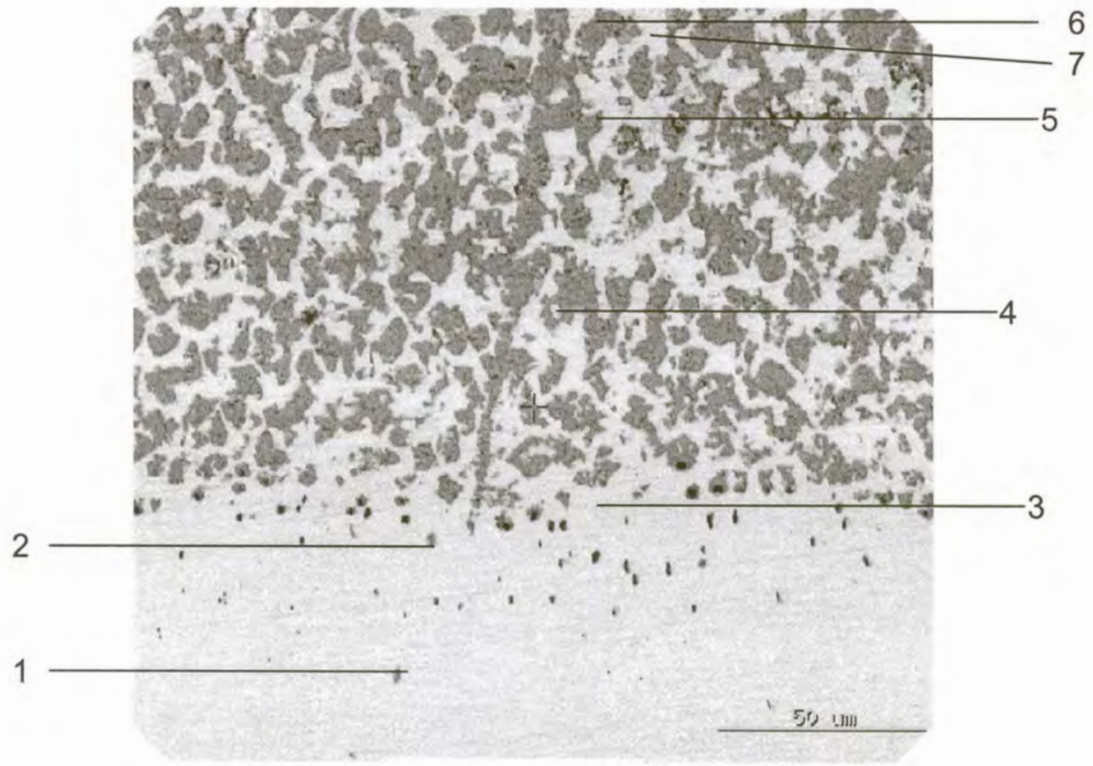

Point 1

Chi-sqd = 4.84 Livetime = 56.0 Sec.

Element	k-ratio (calc.)	ZAF	Atom %	Element Wt %	Wt % Err. (3-Sigma)
Fe-K	0.1923	1.045	19.12	20.09	+/- 2.04
Mn-K	0.2712	1.023	26.85	27.76	+/- 2.23
Si-K	0.0017	1.418	0.46	0.24	+/- 0.16
Cr-K	0.4074	0.986	41.06	40.17	+/- 1.65
Ni-K	0.0238	1.051	2.26	2.50	+/- 0.93
Ti-K	0.1027	0.900	10.25	9.24	+/- 0.71
Total			100.00	100.00	

Point 2

Chi-sqd = 2.27 Livetime = 48.0 Sec.

Element	k-ratio (calc.)	ZAF	Atom %	Element Wt %	Wt % Err. (3-Sigma)
Fe-K	0.4463	1.037	43.31	46.27	+/- 2.50
Mn-K	0.1185	1.023	11.54	12.12	+/- 2.00
Si-K	0.0309	1.464	8.41	4.52	+/- 0.23
Cr-K	0.3393	0.943	32.17	31.99	+/- 1.51
Ni-K	0.0461	1.060	4.35	4.89	+/- 2.02
Ti-K	0.0022	0.922	0.23	0.21	+/- 0.26
Total			100.00	100.00	

Point 3

Chi-sqd = 2.42 Livetime = 33.0 Sec.

Element	k-ratio (calc.)	ZAF	Atom %	Element Wt %	Wt % Err. (3-Sigma)
Fe-K	0.7481	1.010	74.80	75.54	+/- 2.89
Mn-K	0.0027	1.016	0.27	0.27	+/- 0.75
Si-K	0.0017	1.538	0.53	0.27	+/- 0.17
Cr-K	0.1753	0.875	16.32	15.35	+/- 1.12
Ni-K	0.0811	1.057	8.08	8.57	+/- 1.34
Ti-K	0.0000	0.932	0.00	0.00	+/- 0.00
Total			100.00	100.00	

Point 4

Chi-sqd = 3.76 Livetime = 39.0 Sec.

Element	k-ratio (calc.)	ZAF	Atom %	Element Wt %	Wt % Err. (3-Sigma)
Fe-K	0.8241	0.994	81.80	81.91	+/- 2.65
Mn-K	0.0009	1.014	0.10	0.09	+/- 0.56
Si-K	0.0030	1.568	0.94	0.47	+/- 0.27
Cr-K	0.0505	0.840	4.55	4.25	+/- 0.72
Ni-K	0.1258	1.055	12.61	13.28	+/- 1.41
Ti-K	0.0000	0.938	0.00	0.00	+/- 0.00
Total			100.00	100.00	

Point 5

Chi-sqd = 1.73 Livetime = 41.0 Sec.

Element	k-ratio (calc.)	ZAF	Atom %	Element Wt %	Wt % Err. (3-Sigma)
Fe-K	0.4060	1.058	40.69	42.96	+/- 1.95
Mn-K	0.0187	1.022	1.84	1.91	+/- 1.14
Si-K	0.0119	1.445	3.24	1.72	+/- 0.38
Cr-K	0.5496	0.955	53.40	52.50	+/- 1.98
Ni-K	0.0079	1.060	0.75	0.84	+/- 1.08
Ti-K	0.0008	0.896	0.08	0.07	+/- 0.30
Total			100.00	100.00	

Point 6

Chi-sqd = 1.81 Livetime = 31.0 Sec.

Element	k-ratio (calc.)	ZAF	Atom %	Element Wt %	Wt % Err. (3-Sigma)
Fe-K	0.4025	1.059	40.68	42.60	+/- 2.23
Mn-K	0.0174	1.020	1.72	1.78	+/- 1.32
Si-K	0.0049	1.446	1.33	0.70	+/- 0.23
Cr-K	0.5699	0.954	55.77	54.38	+/- 2.33
Ni-K	0.0045	1.059	0.43	0.47	+/- 1.16
Ti-K	0.0007	0.891	0.07	0.06	+/- 0.34
Total			100.00	100.00	

Point 7

Chi-sqd = 3.34 Livetime = 32.0 Sec.

Element	k-ratio (calc.)	ZAF	Atom %	Element Wt %	Wt % Err. (3-Sigma)
Fe-K	0.8138	0.988	80.83	80.42	+/- 2.98
Mn-K	0.0001	1.012	0.01	0.01	+/- 0.60
Si-K	0.0007	1.581	0.23	0.11	+/- 0.17
Cr-K	0.0317	0.838	2.87	2.66	+/- 0.43
Ni-K	0.1596	1.053	16.06	16.80	+/- 1.72
Ti-K	0.0000	0.940	0.00	0.00	+/- 0.00
Total			100.00	100.00	

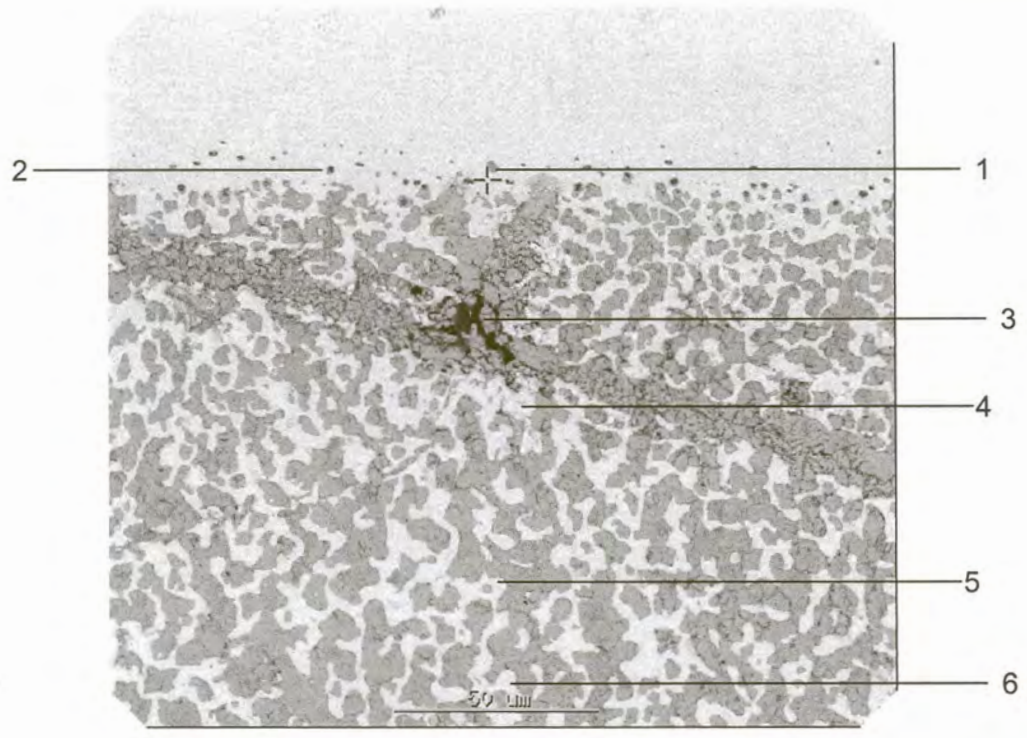

The above diagram shows the structure of scale for type 304 stainless steel reheated at 1260^0C in an atmosphere with 3% excess oxygen for 6hr. The analyses of the different phases are given below.

mon 30/10 Point 1

Element	k-ratio (calc.)	ZAF	Atom %	Element Wt %	Wt % Err. (3-Sigma)
Si-K	0.0057	1.350	1.46	0.77	+/- 0.33
Fe-K	0.0508	1.041	5.03	5.29	+/- 1.83
Cr-K	0.4982	0.987	50.25	49.19	+/- 3.31
Ni-K	0.0000	1.043	0.00	0.00	+/- 0.00
Mn-K	0.4423	1.012	43.26	44.75	+/- 4.44
Total			100.00	100.00	

Mon Oct 30 10:34:50 2000
Point 2
Filter Fit Method
Chi-sqd = 1.60 Livetime = 80.0 Sec.

Element	k-ratio (calc.)	ZAF	Atom %	Element Wt %	Wt % Err. (3-Sigma)
Si-K	0.0177	1.415	4.76	2.51	+/- 0.37
Fe-K	0.4771	1.031	46.90	49.18	+/- 2.82
Cr-K	0.3555	0.934	34.01	33.20	+/- 1.70
Ni-K	0.0467	1.052	4.46	4.91	+/- 2.24
Mn-K	0.1001	1.019	9.89	10.20	+/- 2.19
Total			100.00	100.00	

Point 3

Filter Fit Method
Chi-sqd = 3.51 Livetime = 70.0 Sec.

Element	k-ratio (calc.)	ZAF	Atom %	Element Wt %	Wt % Err. (3-Sigma)
Si-K	0.0015	1.468	0.42	0.21	+/- 0.23
Fe-K	0.8972	1.007	89.67	90.32	+/- 3.01
Cr-K	0.0944	0.829	8.34	7.83	+/- 1.16
Ni-K	0.0127	1.056	1.27	1.34	+/- 1.19
Mn-K	0.0029	1.019	0.30	0.30	+/- 0.86
Total			100.00	100.00	

Point 4

Filter Fit Method
Chi-sqd = 3.40 Livetime = 60.0 Sec.

Element	k-ratio (calc.)	ZAF	Atom %	Element Wt %	Wt % Err. (3-Sigma)
Si-K	0.0007	1.510	0.22	0.11	+/- 0.17
Fe-K	0.8075	0.987	80.14	79.73	+/- 3.13
Cr-K	0.0342	0.834	3.08	2.85	+/- 0.46
Ni-K	0.1643	1.047	16.44	17.19	+/- 2.87
Mn-K	0.0012	1.011	0.13	0.12	+/- 0.63
Total			100.00	100.00	

Point 5

Filter Fit Method
Chi-sqd = 3.21 Livetime = 59.0 Sec.

Element	k-ratio (calc.)	ZAF	Atom %	Element Wt %	Wt % Err. (3-Sigma)

Si-K	0.0005	1.511	0.15	0.08	+/- 0.18
Fe-K	0.8075	0.987	80.14	79.67	+/- 2.46
Cr-K	0.0314	0.833	2.82	2.61	+/- 0.79
Ni-K	0.1686	1.046	16.88	17.64	+/- 1.85
Mn-K	0.0000	1.010	0.00	0.00	+/- 0.00
Total			100.00	100.00	

Point 6

Chi-sqd = 2.38 Livetime = 56.0 Sec.

Element	k-ratio (calc.)	ZAF	Atom %	Element Wt %	Wt % Err. (3-Sigma)
Si-K	0.0758	1.412	19.09	10.69	+/- 0.69
Fe-K	0.7158	1.029	66.13	73.68	+/- 4.11
Cr-K	0.1233	0.888	10.55	10.95	+/- 1.48
Ni-K	0.0078	1.069	0.72	0.84	+/- 1.26
Mn-K	0.0370	1.039	3.51	3.84	+/- 1.20
Total			100.00	100.00	

APPENDIX 6

CALCULATION OF AVERAGE RESIDUAL SCALE THICKNESS

A.6.1 Introduction

The average residual scale thicknesses were calculated using tools on the scanning electron microscope.
The frame area, fraction of scale as well as the width of the scale were measured using the SEM and then the scale area was calculated according to the following:

Scale area = frame area x fraction of scale

The average residual scale was then determined as follows:

Residual scale = scale area / scale width

The results for the various samples are given below.

412								
					residual	residual		
conditions	scale fraction	frame area	scale area	scale width (um)	thickness (um)	thickness (mm)	averages (mm)	
6hr, 1280C, 3% O2	0.04629	7785100	360372.279	2790.2	129.16	0.13		
	0.04595	7785100	357725.345	2792.09	128.12	0.13		
	0.03343	7785100	260255.893	2804.41	92.80	0.09	0.12	
6hr, 1280C, 4% O2	0.03531	7785100	274891.881	2791.17	98.49	0.10		
	0.06607	7785100	514361.557	2809.5	183.08	0.18		
	0.06024	7785100	468974.424	2805.2	167.18	0.17	0.15	
1.5h, 1280C, 3% O2	0.05675	7785100	441804.425	2794.86	158.08	0.16		
	0.13295	7785100	1035029.045	2796.24	370.15	0.37		
	0.07402	7785100	576253.102	2861.93	201.35	0.20	0.24	
1.5h, 1280C, 4% O2	0.17341	7785100	1350014.191	2791.28	483.65	0.48		
	0.0808	7785100	629036.08	2797.1	224.89	0.22		
	0.12741	7785100	991899.591	2794.54	354.94	0.35	0.35	
3hr, 1280C, 3% O2	0.12205	7785100	950171.455	2788.19	340.78	0.34		
	0.08948	7785100	696610.748	2790.53	249.63	0.25	0.30	
3hr, 1280C, 4% O2	0.06995	7785100	544567.745	2786.71	195.42	0.20		
	0.07551	7785100	587852.901	2848.11	206.40	0.21		
	0.06299	7785100	490383.449	2842.34	172.53	0.17	0.19	
3hr, 1210C, 3% O2	0.06699	7785100	521523.849	2794.05	186.66	0.19		
	0.04555	7785100	354611.305	2941.51	120.55	0.12		
	0.03505	7785100	272867.755	2818.68	96.81	0.10	0.13	

APPENDIX

3hr, 1210C, 4% O2	0.05991	7785100	466405.341	2805.26	166.26	0.17		
	0.04791	7785100	372984.141	2805.67	132.94	0.13		
	0.05222	7785100	406537.922	3014.17	134.88	0.13	0.14	
conditions	scale fraction	frame area	scale area	scale width (um)	residual thickness (um)	residual thickness (mm)	averages (mm)	
6hr, 1210C, 3% O2	0.05778	7785100	449823.078	2793.29	161.04	0.16		
	0.04154	7785100	323393.054	2790.21	115.90	0.12		
	0.03543	7785100	275826.093	2815.77	97.96	0.10	0.12	
6hr, 1210C, 4% O2	0.11114	6.97E+06	774224.5794	2682.21	288.65	0.29		
	0.25889	7785100	2015484.539	2824.8	713.50	0.71		
	0.08273	7785100	644061.323	2854.65	225.62	0.23	0.41	
1.5h, 1210C, 3% O2	0.03623	7785100	282054.173	2790.47	101.08	0.10		
	0.04674	7785100	363875.574	2883.66	126.19	0.13		
	0.0333	7785100	259243.83	2865.91	90.46	0.09	0.11	
1.5h, 1210C, 4% O2	0.03531	7785100	274891.881	2781.87	98.82	0.10		
	0.03049	7785100	237367.699	2891.54	82.09	0.08		
	0.02951	1.80E+07	532056.447	4248.78	125.23	0.13	0.10	
304								
6hr, 1280C, 3% O2	0.14949	7785100	1163794.599	2792.52	416.75	0.42		
	0.10319	7785100	803344.469	2803.2	286.58	0.29		
	0.15297	7785100	1190886.747	2589.54	459.88	0.46	0.39	
6hr, 1280C, 4% O2	0.13591	7785100	1058072.941	2796.59	378.34	0.38		
	0.07599	7785100	591589.749	2838.95	208.38	0.21		
	0.0797	7785100	620472.47	2794.26	222.05	0.22	0.27	

APPENDIX

1.5h, 1280C, 3% O2	0.12798	7785100	996337.098	2743.67	363.14	0.36		
	0.08433	7785100	656517.483	2801.82	234.32	0.23		
	0.06574	7785100	511792.474	2736.21	187.04	0.19	0.26	
1.5h, 1280C, 4% O2	0.22375	7785100	1741916.125	2780.7	626.43	0.63		
	0.12483	7785100	971814.033	2792.3	348.03	0.35		
	0.09052	7785100	704707.252	2915.94	241.67	0.24	0.41	
					residual	residual		
conditions	scale fraction	frame area	scale area	scale width (um)	thickness (um)	thickness (mm)	averages (mm)	
3hr, 1280C, 4% O2	0.15609	7785100	1215176.259	2790.18	435.52	0.44		
	0.15794	7785100	1229578.694	2797.7	439.50	0.44		
	0.13439	7785100	1046239.589	2802.49	373.33	0.37	0.42	
3hr, 1280C, 3% O2	0.22525	7785100	1753593.775	2795.49	627.29	0.63		
	0.19309	7785100	1503224.959	2810.17	534.92	0.53	0.58	
3hr, 1250C, 4% O2	0.04765	7785100	370960.015	2793.41	132.80	0.13		
	0.08311	7785100	647019.661	2835.55	228.18	0.23		
	0.07546	7785100	587463.646	2888.69	203.37	0.20	0.19	
6hr, 1250C, 4% O2	0.07311	7785100	569168.661	2833.82	200.85	0.20		
	0.04901	7785100	381547.751	2790.39	136.74	0.14		
	0.08098	7785100	630437.398	2851.98	221.05	0.22	0.19	
3hr, 1250C, 3% O2	0.10119	7785100	787774.269	2780.2	283.35	0.28		
	0.12208	7785100	950405.008	2798.56	339.61	0.34		
	0.10739	7785100	836041.889	2813.84	297.12	0.30	0.31	

APPENDIX

1.5hr, 1250C, 3% O2	0.20583	7785100	1602407.133	2796.15	573.08	0.57		
	0.09931	7785100	773138.281	2794.9	276.62	0.28	0.42	
6hr, 1250C, 3% O2	0.11368	7785100	885010.168	2780.05	318.34	0.32		
	0.11485	7785100	894118.735	2832.39	315.68	0.32		
	0.07389	7785100	575241.039	2798.56	205.55	0.21	0.28	
1.5h, 1250C, 4% O2	0.30795	7785100	2397421.545	2799.92	856.25	0.86		
	0.11883	7785100	925103.433	2795.79	330.89	0.33		
	0.12106	7785100	942464.206	2798.19	336.81	0.34	0.51	

APPENDIX

APPENDIX 7

SCANNING ELECTRON MICROGRAPHS OF SOME OF REMAINING RESULTS

The figure below shows the appearance of the exterior surface of a descaled type 304 sample, showing that the appearance of the cracked residual scale reflects the underlying austenite grain structure.

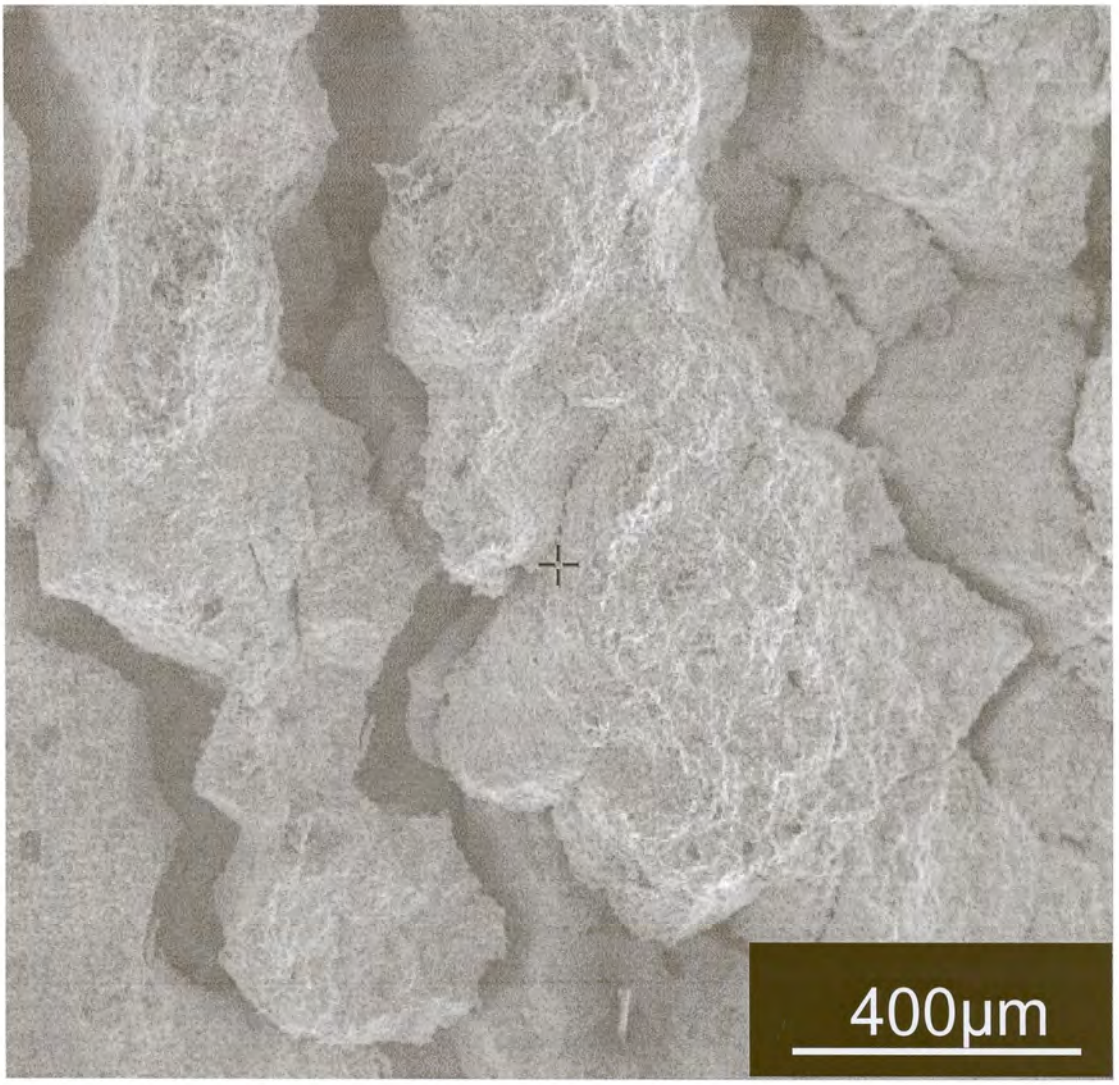

The topography visible in this image is that of the residual scale attached to a type 412 stainless steel sample.

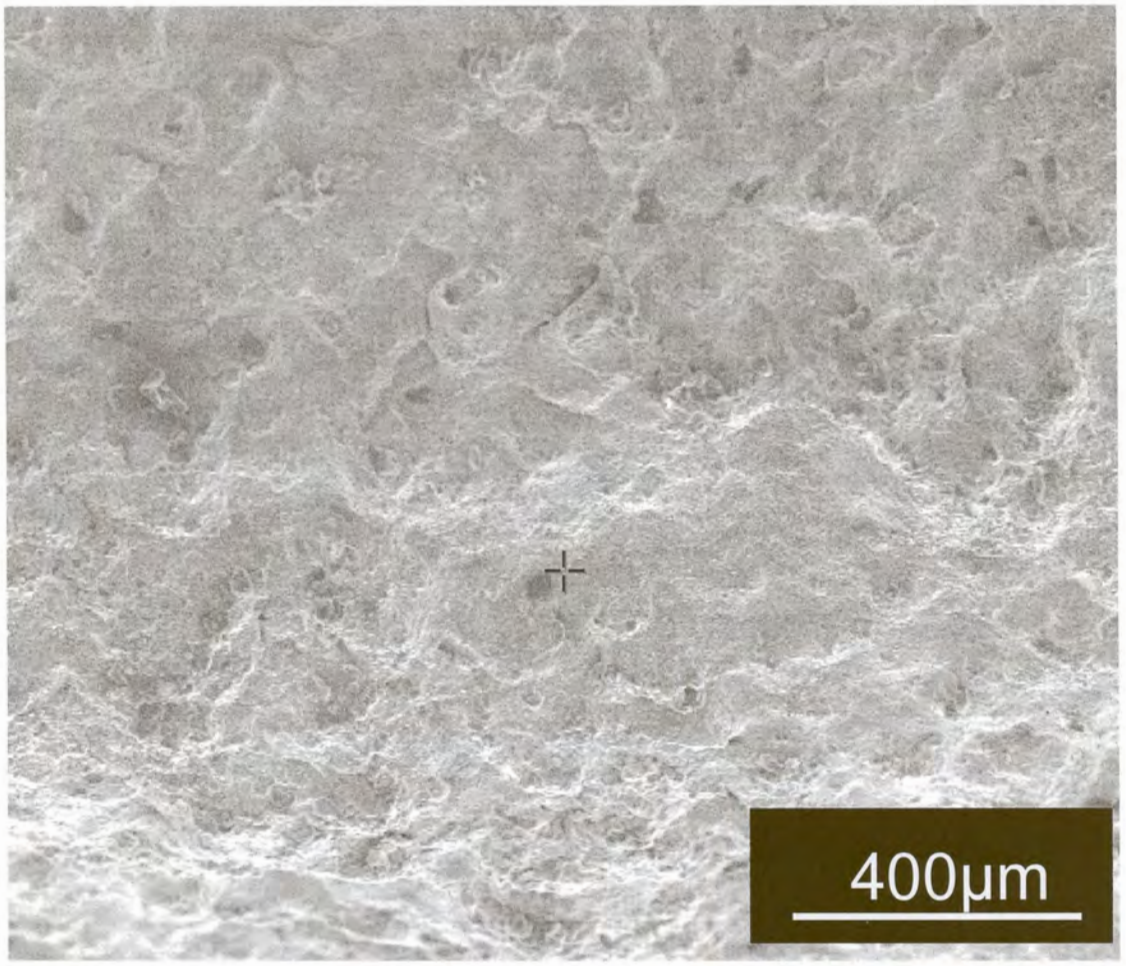

Montage of descaled surface of type 304 sample, showing that the residual scale thickness corresponds to the full thickness of the entangled region. The scale is towards the upper part of the image and the steel substrate towards the bottom. This sample was oxidized at a reheating temperature of 1250 ^{0}C, with 4% excess oxygen for 3 hours.

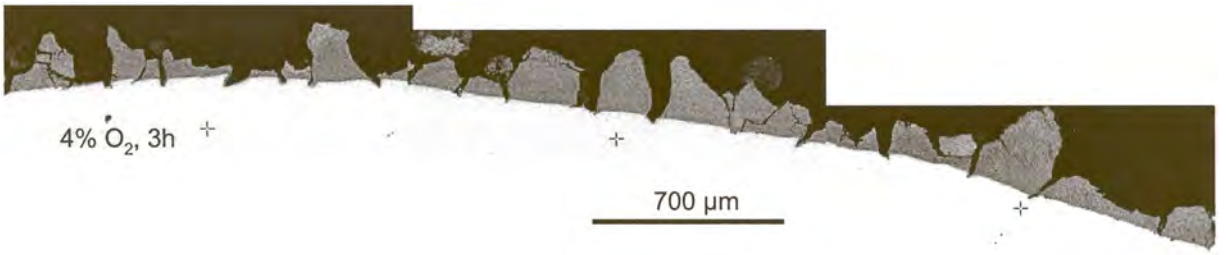

Montage of descaled surface of type 412 stainless steel sample. This sample was oxidised at a reheating temperature of 1210 ^{0}C, with 3% excess oxygen for 6 hours.

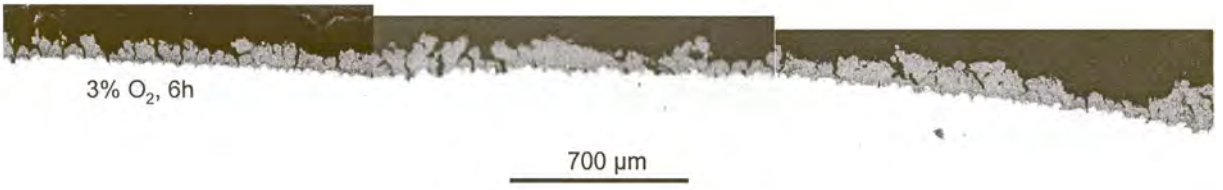

Etched cross-sections of type 304 samples reheated at 1250 ^{0}C. Samples were electrolytically etched in oxalic acid to reveal microstructure of the steel. Cracks in the residual steel can be seen to correspond to grain boundaries in the underlying microstructure.